

University of Windsor

## Scholarship at UWindor

---

Electronic Theses and Dissertations

Theses, Dissertations, and Major Papers

---

2009

### Tribological Studies of Eutectic Al-Si Alloys Used for Automotive Engine Blocks Subjected to Sliding Wear Damage

Guijun Xue  
*University of Windsor*

Follow this and additional works at: <https://scholar.uwindsor.ca/etd>

---

#### Recommended Citation

Xue, Guijun, "Tribological Studies of Eutectic Al-Si Alloys Used for Automotive Engine Blocks Subjected to Sliding Wear Damage" (2009). *Electronic Theses and Dissertations*. 149.  
<https://scholar.uwindsor.ca/etd/149>

This online database contains the full-text of PhD dissertations and Masters' theses of University of Windsor students from 1954 forward. These documents are made available for personal study and research purposes only, in accordance with the Canadian Copyright Act and the Creative Commons license—CC BY-NC-ND (Attribution, Non-Commercial, No Derivative Works). Under this license, works must always be attributed to the copyright holder (original author), cannot be used for any commercial purposes, and may not be altered. Any other use would require the permission of the copyright holder. Students may inquire about withdrawing their dissertation and/or thesis from this database. For additional inquiries, please contact the repository administrator via email ([scholarship@uwindsor.ca](mailto:scholarship@uwindsor.ca)) or by telephone at 519-253-3000ext. 3208.

**TRIBOLOGICAL STUDIES OF EUTECTIC AL-SI ALLOYS  
USED FOR AUTOMOTIVE ENGINE BLOCKS  
SUBJECTED TO SLIDING WEAR DAMAGE**

**By**

**GUIJUN XUE**

**A Thesis**

**Submitted to the Faculty of Graduate Studies  
through Mechanical, Automotive and Materials Engineering  
in Partial Fulfillment of the Requirements for  
the Degree of Master of Applied Science  
at the University of Windsor**

**Windsor, Ontario, Canada**

**2009**

**© 2009 Guijun Xue**

**Tribological Studies of Eutectic Al-Si Alloys Used for Automotive Engine Blocks  
Subjected to Sliding Wear Damage**

**By**

**Guijun Xue**

APPROVED BY:

---

**Dr. A. Fartaj**

**Mechanical Engineering, MAME**

---

**Dr. H. Hu**

**Engineering Materials, MAME**

---

**Dr. A.T. Alpas, Co- Advisor**

**Engineering Materials, MAME**

---

**Dr. A. Edrisy, Co- Advisor**

**Engineering Materials, MAME**

---

**Dr. N. Zamani, Chair of Defense**

**Mechanical, Automotive & Materials Engineering**

September 1, 2009

## **Author's Declaration of Originality**

I hereby certify that I am the sole author of this thesis and that no part of this thesis has been published or submitted for publication.

I certify that, to the best of my knowledge, my thesis does not infringe upon anyone's copyright nor violate any proprietary rights and that any ideas, techniques, quotations, or any other material from the work of other people included in my thesis, published or otherwise, are fully acknowledged in accordance with the standard referencing practices. Furthermore, to the extent that I have included copyrighted material that surpasses the bounds of fair dealing within the meaning of the Canada Copyright Act, I certify that I have obtained a written permission from the copyright owner(s) to include such material(s) in my thesis and have included copies of such copyright clearances to my appendix.

I declare that this is a true copy of my thesis, including any final revisions, as approved by my thesis committee and the Graduate Studies office, and that this thesis has not been submitted for a higher degree to any other University or Institution.

## **ABSTRACT**

The microstructures and wear performances of linerless engine cylinder blocks made of two eutectic Al-Si alloys with different Si morphologies were characterized after the engine tests. Overall, both the Al-11 wt. % Si alloy and the Al-12.6 wt. % Si alloy provided similar wear performance.

Block-on-ring wear tests were applied to the Al-11% Si alloy. The MW regime in air consisted of two sub-regimes: MW-1 and MW-2. The argon atmosphere produced a 10-fold reduction in wear rates and the formation of LMW regime at loads less than 10 N. The metallic tribolayers formed in the MW under argon atmosphere were uniform and stable, resulting lower wear rates than those in air. The mechanism of material removal under argon atmosphere was delamination. The SW occurring in argon was observed at a relatively low load, compared to an air atmosphere. Wear was also more sensitive to applied load in the argon atmosphere.

*To*

*my wife Fengmei Wang*

*my son Richard Xue*

## **ACKNOWLEDGEMENTS**

I would like to express my sincere gratitude to supervisors Dr. Ahmet Alpas and Dr. Afsaneh Edrisy for their valuable guidance and wisdom throughout my study at the University of Windsor. I would like to sincerely thank my other committee members, Dr. Hu and Dr. Fartaj, for taking time from their busy schedules to make valuable suggestions for my work.

Special thanks go to Mr. J. Robinson, Mr. P. Sequin and the members of the Technical Support Center for their technical assistance and Mrs. B. Denomey and Ms. Rosemarie Gignac for their administrative assistance. I am grateful to Dr. S. Akarca and Dr. M. Shafiei, the previous and present IRC research coordinators, for their support.

All previous and current researchers in the Tribology of Lightweight Materials at the IRC are thankfully acknowledged for their help and friendship.

The financial support from NSERC and General Motors of Canada is greatly appreciated. I also would like to acknowledge the Graduate Tuition Scholarship provided by the University of Windsor.

## TABLE OF CONTENTS

AUTHOR’S DECLARATION OF ORIGINALITY .....	iii
ABSTRACT .....	iv
ACKNOWLEDGEMENTS .....	vi
LIST OF TABLES .....	xi
LIST OF FIGURES .....	xii
LIST OF ABBREVIATIONS .....	xx
CHAPTER1 INTRODUCTION .....	1
CHAPTER 2 LITERATURE SURVEY .....	3
2.1. Dry and Lubricated Sliding Wear in Automotive Engines .....	3
2.1.1. Internal Combustion (IC) Engines .....	3
2.1.2. Engine Wear Regimes .....	4
2.1.3 Factors That Influence Engine Block Wear .....	5
2.2. Al-Si Alloys Used in Engine Blocks .....	7
2.2.1. Typical Al-Si Alloys Developed for Engine Blocks .....	7
2.2.2. Technologies for Manufacturing Aluminum Cylinder Blocks [33-34] .....	9
2.2.2.1. Sand casting .....	9
2.2.2.2. Lost Foam Process .....	9
2.2.2.3. Die Casting .....	9
2.2.2.4. Squeeze Die Casting .....	10
2.2.2.5. Other methods .....	10
2.2.3. Tribological Methods for Testing Engine Materials .....	11
2.3. Al-Si Alloy Wear .....	12
2.3.1. Effect of Normal Load on Wear .....	12
2.3.2. Effect of Sliding Speed on Wear .....	13



2.3.3.	Effect of Temperature on Wear.....	13
2.3.4.	Effect of Environment on Wear.....	14
2.3.5.	Tribolayer Formation.....	17
2.3.6.	Effect of Microstructure on the Wear.....	18
2.3.6.1.	Volume Fraction for Si Particles.....	18
2.3.6.2	Effect of Silicon Morphology on Wear.....	19
2.4.	Wear Regimes and Mechanisms of Al-Si Alloys.....	22
2.5.	Research Objectives.....	25
CHAPTER 3 EXPERIMENTAL DETAILS.....		42
3.1.	Engine Tests and Materials for Tests.....	42
3.2.	Dry Sliding Tests.....	43
3.3.	Sample Preparations for Wear Tests.....	44
3.4.	Wear Rate Measurement.....	44
3.5.	Sample Preparation for Metallographic Analysis.....	45
3.6.	Evaluation of Worn Surface and Subsurface Morphologies.....	46
3.7.	Measurement of Si Aspect Ratio and Secondary DAS.....	47
CHAPTER 4 MICROSTRUCTURES, PROPERTIES AND WEAR OF LINERLESS		
Al-Si ENGINES: SAND-CAST AND BRASS-CHILLED ALLOYS.....		50
4.1.	Al-Si Alloy Engines Tested.....	50
4.2.	Chemical Composition and Hardness of Al-Si Alloys.....	51
4.3.	Alloys Microstructures.....	51
4.3.1	Dendrite Arm Spacing (DAS) of the Two Alloys.....	52
4.3.2	Identification of Phases in the Alloys.....	52
4.3.3	Si Morphology and Size.....	53
4.3.4	Surface Morphology.....	53

4.4.	Analysis of the Normal Wear Area.....	54
4.4.1	Sand-Cast Alloy.....	54
4.4.2	Brass-chilled Alloy.....	54
4.5.	Discussion.....	55
4.6.	Summary.....	56
CHAPTER 5 DRY SLIDING WEAR BEHAVIOUR OF Al-Si ALLOYS UNDER CONTROLLED ATMOSPHERIC CONDITIONS.....		78
5.1.	Introduction.....	78
5.2.	Dry Sliding Wear Behaviour of Al-11% Si Alloy.....	79
5.2.1.	Wear Regimes and Wear Transitions in Air.....	79
5.2.2.	Wear Regimes and Wear Transitions in an Argon Atmosphere.....	80
5.2.3.	Wear Performance Comparisons of Al-11% Si Alloy and A390.....	82
5.3.	Examinations of Samples Tested in Air.....	83
5.3.1.	Observation of Worn Surfaces.....	83
5.3.2.	Cross- Sectional Observation of Worn Subsurfaces.....	84
5.3.3.	Wear Debris.....	86
5.4.	Examination of Tested Samples in Argon.....	88
5.4.1.	Worn Surfaces.....	88
5.4.2.	Subsurface Microstructures.....	89
5.5.	Discussion.....	90
5.5.1.	Wear Comparison under Air and Argon Atmospheres.....	90
5.5.2.	Wear Mechanism under Controlled Atmospheres.....	92
5.5.2.1.	In Air.....	92
5.5.2.2.	In Argon.....	93
CHAPTER 6 SUMMARY AND CONCLUSIONS.....		140

6.1. Microstructures and Wear Performances.....	140
6.2. Dry Sliding Wear Behaviour of Al-11% Si Alloy under Dry Air and Argon Atmospheres and Their Wear Mechanisms.....	140
6.3. Suggestions for Future Work.....	142
APPENDICES.....	143
REFERENCES.....	144
VITA AUCTORIS.....	148

## LIST OF TABLES

<b>Table 2.1.</b> .....	27
Chemical composition of the selected typical commercial Al-Si alloys [29]	
<b>Table 4.1.</b> .....	57
Chemical compositions (in wt% ) of the Al-Si alloys studied	
<b>Table 4.2.</b> .....	57
Hardnesses of the alloys studied	
<b>Table 4.3.</b> .....	57
Roughness of these two alloys studied (Area covered: 1393x1831 mm <sup>2</sup> )	
<b>Table 4.4.</b> .....	58
Summary of the Microstructures and Wear Performance for Two Eutectic Al-Si Alloy Engines	
<b>Table 5.1.</b> .....	95
The characteristics of wear regimes in an air atmosphere	
<b>Table 5.2.</b> .....	96
Comparisons of worn surface roughnesses formed during wear under air and argon atmosphere	

## LIST OF FIGURES

<b>Fig. 2.1.</b> .....	28
Main components of an internal combustion engine [9].	
<b>Fig. 2.2.</b> .....	28
P-V <sub>0</sub> diagram for four-stroke cycle IC engine [11].	
<b>Fig. 2.3.</b> .....	29
Pressure load distributions on major side-thrust cylinder wall per cycle- full load, 3,800 rpm (1 in. =25.4mm) [12].	
<b>Fig. 2.4.</b> .....	29
Pressure load distributions on minor side-thrust cylinder wall per cycle- full load, 3,800 rpm (1 in. =25.4mm) [12].	
<b>Fig. 2.5.</b> .....	30
The relationship between the coefficient of friction and the oil film thickness ratio [15].	
<b>Fig. 2.6.</b> .....	31
The lubrication regimes discussed above in <b>Fig.2.5</b> [15].	
<b>Fig. 2.7.</b> .....	32- 33
Aluminum-Silicon binary phase diagrams (a) and typical microstructures of (b) hypoeutectic 319 and (c) Hypereutectic A 390 alloy [1].	
<b>Fig. 2.8.</b> .....	33
Illustration of a linerless engine block made from a eutectic Al-Si alloy from GM.	
<b>Fig. 2.9.</b> .....	34
The pin-on-disk wear test machine]: a) three different arrangements for a simple pin-on-disk wear test machine; b) block-on-ring wear machine; c) reciprocating wear machine [36].	
<b>Fig. 2.10.</b> .....	34
Variations of wear rate of four Al-Si alloys with normal load [39].	
<b>Fig. 2.11.</b> .....	35
Wear rates of the as-received A390, 383 and Al-25Si alloys plotted against load on a logarithmic scale. The two sub-regimes of mild wear MW-1 and MW-2 are separated by a transition regime. The loads 20, 35, and 60N correspond to the highest load in MW-1. The transition from MW-2 to the severe wear regime occurs at 150N for all the alloys [40].	
<b>Fig. 2.12.</b> .....	35
Variation of wear of 6061 aluminum with normal load at different sliding speeds [21].	
<b>Fig. 2.13.</b> .....	36
(a) Contact surface temperature versus sliding time plots at different velocities at a constant load of 5.0 N; (b) contact surface temperature versus sliding time plots at 50N;	

(c) contact surface temperature versus sliding distance plots at different loads at a constant sliding velocity of 0.8m/s [21].

<b>Fig. 2.14.</b> .....	37
Effect of forced cooling by chilled water on the mild to severe wear transition in 6061 Al worn against SAE 52100 steel. Without cooling the contact temperature exceeds $T_c$ (395K) leading to severe wear ( $\circ$ ). Cooling the system will ensure that the contact surface temperature stays below 395K, thus only mild wear is observed ( $\bullet$ ). Load =98N, $v=0.8\text{m/s}$ [21].	
<b>Fig. 2.15.</b> .....	38
Variation of transition load with Si content [38].	
<b>Fig. 2.16.</b> .....	38
Variation of wear rates of aluminum alloys sliding against a hard steel bush at a speed of 1.96 m/sec (Loads: $\circ$ :1 kg, $\Delta$ :1.5 kg, $\square$ : 2kg, $\bullet$ : 2.5 kg) by Clarke and Sarkar [63].	
<b>Fig. 2.17.</b> .....	39
Wear regimes in a cast A356 Al ( $\circ$ ) and A356-20% SiC ( $\bullet$ ) particles (Configuration: block on ring, Speed: 0.8 m/s, Atmosphere: ambient air) by Zhang [70].	
<b>Fig. 2.18.</b> .....	40
Variation of the wear rates with the test load [40].	
<b>Fig. 2.19.</b> .....	41
Comparisons of: (a) the volumetric wear and (b) the COF curves of A390 in air and argon atmospheres at a load of 10 N [46].	
<b>Fig. 3.1.</b> .....	48
A photograph showing the general view of the block on ring tribometer (b) An enlarged view of sample holder with an Al-Si block sample, and spindle carrying a counterface ring.	
<b>Fig. 3.2.</b> .....	49
Three dimensional schematics showing the preparation of the taped sections. Metal stand cut at an angle of $5.7^\circ$ .	
<b>Fig. 3.3.</b> .....	49
Measurement method of secondary dendrite arm spacing.	
<b>Fig. 4.1.</b> .....	59
Sand-cast Al-Si engine bore surface with the indications of different wear type after dynamometer engine test.	
<b>Fig. 4.2.</b> .....	59
Brass-chilled Al-Si engine bore surface after hot scuffing test at $150^\circ\text{C}$ .	
<b>Fig. 4.3.</b> .....	60
Optical micrographs from unworn areas of two engines showing dendrites clearly. (a) Sand-cast alloy, (b) Brass-chilled alloy.	

<b>Fig. 4.4.</b> .....	61
Histograms showing the dendrite arm spacing in (a) Sand-cast alloy, (b) Brass-chilled alloy.	
<b>Fig. 4.5.</b> .....	62
Optical micrographs in unworn area of two alloys (a) Sand-cast (b) Brass chilled alloy.	
<b>Fig. 4.6.</b> .....	63
SEM secondary micrographs, (a) sand-cast Al-Si alloy,(b) brass-chilled, the phases identified using SEM/EDS and labeled as: a) $\alpha$ -Al, Matrix; b) Si Phase; c) light gray particles $\text{CuAl}_2$ phase; d) Chinese script phase $\text{Al}_{15}(\text{Fe}, \text{Mn})_3\text{Si}_2$ , e) $\text{Al}_5\text{Mg}_8\text{Cu}_2\text{Si}_6$ , gray needle-like.	
<b>Fig. 4.7.</b> .....	64
(a) A secondary SEM micrograph in sand-cast alloy showing plate-like Si morphology, (b) the EDS spectrum identifies the Si particles.	
<b>Fig. 4.8.</b> .....	65
A secondary SEM micrograph showing that Si morphology in brass-chilled alloy is more spherical, (b) the EDS spectrum identify the Si particles.	
<b>Fig. 4.9.</b> .....	66
<b>4.9</b> Histograms showing Si particle length (a) and width (b) distribution in the sand-cast Al-Si alloy.	
<b>Fig. 4.10.</b> .....	67
Histograms showing Si particle (a) length and (b) width distribution in the brass-chilled Al-Si alloy.	
<b>Fig. 4.11.</b> .....	68
Optical surface profilometer morphology of virgin surface in two engines, (a) sand-cast, (b) brass-chilled showing their $R_a$ are 74.7nm and 80,17nm respectively.	
<b>Fig. 4.12.</b> .....	69
Histograms showing the Si Height Distribution in (a) sand-cast and (b) brass-chilled alloys.	
<b>Fig. 4.13.</b> .....	70
Secondary SEM image of sand-cast engine normal wear surface (a) and unworn area (b).	
<b>Fig. 4.14.</b> .....	71
Secondary SEM micrograph and the EDS spectra showing the elemental surface compositions inside the areas marked in the secondary SEM micrograph in the sand-cast Al-Si alloy engine normal wear surface: (a) secondary SEM micrograph, (b)-(d) the elemental surface compositions inside the areas marked in the secondary SEM micrograph.	
<b>Fig. 4.15.</b> .....	72
Secondary SEM micrographs showing a layer (the rectangle area) formed on the	

contact wear surface (a) and the EDS spectra identify the components of the regions marked in the sand-cast Al-Si alloy (b).

<b>Fig. 4.16.</b> .....	73
Optical surface profilometer morphology of wear surface of sand-cast engine at two magnifications, (a) 25× and (b) 100 ×. Roughness was determined on an area of $3.0 \times 4.2 \text{ mm}^2$ .	
<b>Fig. 4.17.</b> .....	74
Secondary SEM image of normal wear surface on the sand-cast engine showing delamination happened on the wear area.	
<b>Fig. 4.18.</b> .....	74
Cross-sectional optical and SEM showing Si fracture on the contact wear surfaces of sand-cast alloy.	
<b>Fig. 4.19.</b> .....	75
Secondary SEM micrograph of the layer formed on the contact wear ( $\sim 1\mu\text{m}$ ) of the brass-chilled engine, (b) the EDS spectra identify its components (the marked area).	
<b>Fig. 4.20.</b> .....	76
Optical surface profilometer morphology of wear surface at two magnifications for the brass-chilled engine, (a) 25× and (b) 100×.	
<b>Fig. 4.21.</b> .....	77
Secondary SEM micrographs of contact wear surface in the brass-chilled engine showing delamination of the contact surface.	
<b>Fig. 4.22.</b> .....	77
Cross-sectional SEM image showing Si fracture on the contact surfaces of the brass-chilled alloy.	
<b>Fig. 5.1.</b> .....	97
Wear rates and transitions of Al-11% Si alloy with increasing the test load. The tests were conducted at a constant speed of 1 m/s and a sliding distance of $4 \times 10^3 \text{ m}$ in dry air (5% RH). MW-1 (at loads below 30 N) and MW-2 (at loads between 52 N and 160 N) are the sub-regimes of mild wear. Severe wear occurred at loads above 160 N.	
<b>Fig. 5.2.</b> .....	98
Volume loss vs. sliding distance plots of Al-11% Si alloy for mild wear at loads 10 N and 70 N in air ( $5 \pm 2\%$ ). Volume losses determined by mass loss measurements showed the steady state nature of the mild wear. The volumetric wear rate can be calculated from the slopes of the volumetric loss vs. sliding distance curves.	
<b>Fig. 5.3.</b> .....	99
Variation of the coefficient of friction (COF) with the sliding distance at three loads in air (5% RH): at 10N (a), at 70 N and 170 N (b).	
<b>Fig. 5.4.</b> .....	100
Variation of the wear rates with the test load for Al-11% Si tested in an argon atmosphere and in air (5%RH). UMW was observed at loads $< 10 \text{ N}$ , MW between 10N	



and 80N and SW above 80N.

<b>Fig. 5.5.</b> .....	101
The micrographs showing volume loss vs. sliding distance at sliding distance of 4000 m in argon at loads (a) 10N and (b) 50N.	
<b>Fig. 5.6.</b> .....	102
Variation of the coefficient of friction (COF) with the sliding distance at two loads corresponding to mild and severe wear regimes in argon (5% RH): LMW at 10 N, MW at 60N. 80N and SW at 100 N.	
<b>Fig. 5.7(a)</b> .....	103
(a) Wear regimes and transitions of Al-11% Si alloy with increasing the test load. The tests were conducted at a constant speed of 1 m/s and a sliding distance of $4 \times 10^3$ m in air (5% RH). MW-1 (at loads below 30 N) and MW-2 (at loads between 52 N and 160 N) are the sub-regimes of mild wear. Severe wear occurred at loads above 160 N.	
<b>Fig. 5.7(b)</b> .....	104
Variation of the wear rates with the test load for Al-11% Si tested in an argon atmosphere (5%RH). LMW at loads <10 N, MW between 10N and 80N and SW above 80N.	
<b>Fig. 5.8.</b> .....	105
Pseudo-3D images (a), X (b) and Y profile (c) of the middle worn surface at the load of 1N in air.	
<b>Fig. 5.9.</b> .....	106
Pseudo-3D images (a), X (b) and Y profile (c) of the middle worn surface at the load 10N in air.	
<b>Fig. 5.10.</b> .....	107
Pseudo-3D images (a), X (b) and Y profile (c) of the middle worn surface at the load 100N in air.	
<b>Fig. 5.11.</b> .....	108
Pseudo-3D images (a), X (b) and Y profile (c) of the middle worn surface at the load 170N in air.	
<b>Fig. 5.12.</b> .....	109
Variations of worn surface roughness with load in air (a) in mild wear regime (b) transition from mild wear to severe wear.	
<b>Fig. 5.13.</b> .....	110
(a) A low magnification secondary SEM micrograph of the worn surface of an Al-11% Si alloy sample in the mild wear regime at 5 N (MW-1) after 4000 m. (b) Back-scattered SEM micrograph of the same area.	
<b>Fig. 5.14.</b> .....	111
SEM micrograph of crater area in the worn surface at a load of 5N, showing equiaxed particles in the crater.	

<b>Fig. 5.15.</b> .....	112
(a) The EDS spectrum of the regions marked as A (a) and B, (b) are shown in Fig.5.13 respectively, indicating the formation of Fe rich oxidized tribolayer.	
<b>Fig. 5.16.</b> .....	113
Secondary SEM micrograph of the worn surface of Al-11% Si Alloy sample at 10N (a) and 100N (b) after 4000 m tests.	
<b>Fig. 5.17.</b> .....	114
Secondary SEM micrograph of the worn surface of 1Al-11% Si Alloy sample at 170N after 2000 m with low (a) and high (b) magnifications.	
<b>Fig. 5.18.</b> .....	115
Cross-sectional optical micrographs showing the tribolayers in mild wear in air (a) 1N, (b) 10N, (c) 40N and (d) 100N.	
<b>Fig. 5.18.</b> .....	116
<b>Continued</b> Cross-sectional optical micrographs showing the tribolayers in mild wear in air (a) 1N, (b) 10N, (c) 40N and (d) 100N.	
<b>Fig. 5.19.</b> .....	117
Worn surface microhardness variation with load for the Al- 11% Si alloy (Vickers indenter, 100gf).	
<b>Fig. 5.20.</b> .....	118
Subsurface optical micrographs of Al-11% Si alloy taken from the tapered sections cut at angle of 5.7° to the contact surfaces at loads of (a) 10 N and (b) 70 N in air (5% RH). The micrographs showed deeper and wider surface grooves, and a thicker mixed and oxidized tribolayer in MW-2 compared to MW-1.	
<b>Fig. 5.21.</b> .....	119
Subsurface microhardness (HV, 50g) profile at load of 10N (a) and 70N (b) in air after a sliding distance of 4000m. Microhardness measurements were performed on transverse tapered sections (cut at an angle of 5.7° to worn surface).	
<b>Fig. 5.22.</b> .....	120
The secondary SEM micrograph given in (a) shows worn subsurface morphology of the Al-11% Si alloy at 40 N in air (5% RH) and evidence for removal of the tribolayers by delamination, as shown by the portion of the tribolayer which was about to be removed., (b) the EDS spectrum of the regions marked indicating the formation of Fe rich oxidized tribolayer at 40N.	
<b>Fig. 5.23.</b> .....	121
The secondary SEM micrograph given in (a) shows worn subsurface morphology of the Al-11% Si alloy at 100 N in air (5% RH) and evidence for removal of the tribolayers by spallation, (b) the EDS spectrum of the regions marked indicating the formation of tribolayer at 100N.	
<b>Fig. 5.24.</b> .....	122
SEM micrograph showing two magnification views of the wear debris produced at 20	

N in air (5% RH). (a) The micrograph indicates that the debris was mainly composed of fine particles, but plate-like and ribbon shaped particles were also observed. (b) A high magnification secondary SEM micrograph of the fine particle debris.

**Fig. 5.25.** ..... 123

EDS spectrums of the debris produced at 15N from the regions marked as A, B and C in

**Fig. 5.24:** (a) ribbon shaped Fe chips (A), (b) fine particles (B) and (c) large particles (C).

**Fig. 5.26.** ..... 124

SEM (a) and EDS (b) spectrums of the debris produced at 70N from the debris particles showing that they were rich in Al content with small amounts of Fe and O.

**Fig. 5.27.** ..... 125

SEM (a) and EDS (b) spectrums of the debris produced at 170N from the debris particles showing that their chemical compositions were similar to that of unworn Al-Si samples.

**Fig. 5.28.** ..... 126

Pseudo-3D images (a) , X (b) and Y profile (c) of the middle worn surface at the load 1N in argon.

**Fig. 5.29.** ..... 127

Pseudo-3D images (a), X (b) and Y profile (c) of the middle worn surface at the load 50N in air.

**Fig. 5.30.** ..... 128

Pseudo-3D images (a) , X (b) and Y profile (c) of the middle worn surface at the load 80N in argon.

**Fig. 5.31.** ..... 129

Pseudo-3D images (a) , X (b) and Y profile (c) of the middle worn surface at the load 100N in argon.

**Fig. 5.32.** ..... 130

Variation of worn surface roughness parameters with load in argon.

**Fig. 5.33.** ..... 131

SEM micrographs of the worn surface of Al-11% Ai alloy sample tested at 1N in argon atmosphere: (a) secondary SEM, (b) back scattered SEM.

**Fig. 5.34.** ..... 132

SEM micrographs of the worn surface of Al-11% Ai alloy sample tested at 50N in argon atmosphere with two magnifications.

**Fig. 5.35.** ..... 133

SEM micrographs of the worn surface of Al-11% Ai alloy sample tested at 80N (a) and 100N (b) in argon atmosphere.

**Fig. 5.36.** ..... 134

SEM micrographs of the edge of wear track at 1N (a) and 50N (b) in argon. At 50N, layers in the form of flake were observed.

**Fig. 5.37.** ..... 135

EDS spectra of the worn surfaces at 1N and 50N after a sliding distance of 4000m tested in argon atmosphere.

**Fig. 5.38.** ..... 136

Subsurface optical micrographs of Al-11% Si alloy taken from the tapered sections cut at angle of  $5.7^\circ$  to the contact surfaces at loads of (a) 10 N, (b) 50 N and (c) in argon (5% RH).

**Fig. 5.39.** ..... 137

Subsurface microhardness (HV, 10g) profile at load of 10N, 50N and 80N in argon after a sliding distance of 4000m. Microhardness measurements were performed on transverse tapered sections (cut at an angle of  $5.7^\circ$  to worn surface)

**Fig. 5.40.** ..... 138

Back scattered SEM (a) and EDS (b) spectra of the worn subsurface at 10N after a sliding distance of 4000m tested in argon atmosphere.

**Fig. 5.41.** ..... 139

Back scattered SEM (a) and EDS (b) spectra of the worn subsurface at 50N and 50N after a sliding distance of 4000m tested in argon atmosphere.

## **LIST OF ABBREVIATIONS**

<b>MW</b>	<b>Mild wear</b>
<b>SW</b>	<b>Severe wear</b>
<b>UMW</b>	<b>Ultra-mild wear</b>
<b>LMW</b>	<b>Low Wear (new definition of previous UMW)</b>
<b>MW-1</b>	<b>The first regime of mild wear</b>
<b>MW-2</b>	<b>The second regime of mild wear</b>
<b>EDS</b>	<b>Electron diffraction spectrum</b>
<b>SEM</b>	<b>Secondary electron microscopy</b>
<b>COF</b>	<b>Coefficient of friction</b>
<b>HV</b>	<b>Vickers hardness</b>
<b>HB</b>	<b>Hardness in Brinell scale</b>
<b>RH</b>	<b>Relative Humidity</b>
<b>SD</b>	<b>Sliding direction</b>

# CHAPTER 1

## INTRODUCTION

Lightweight materials, particularly Al-Si alloys, have been developed for use in engine applications as a way to meet the automotive industry's continuous demand for better fuel efficiency and cleaner exhaust. The Al-Si alloys used in engine blocks can be divided into three categories, based on their silicon percentages: hypoeutectic (5-10 wt% Si, such as 356, 380), eutectic and hypereutectic alloys (14-20 wt% Si, such as 390 series). The binary eutectic Al-Si alloy contains 12.6 wt% Si [1].

When cylinder blocks cast of hypoeutectic alloys like AA319 or AA 356 are used, cylinder liners made of cast iron or, in some cases, metal matrix composite must be inserted. An alternative is the use of specific surface treatments (thermal spray coatings) that provide wear resistance during engine operation [2-6]. On the other hand, cast hypereutectic alloys can also be used to manufacture monolithic engine block without liners or surface treatments that still achieves a satisfactory performance [7]. Their overall manufacturing cost, however, remains high due to high casting and machining costs [8], which necessitates the development of new Al-Si alloys with the required combination of good casting, machining and wear resistance properties to use in cylinder blocks—an innovation that would simplify the manufacturing process and save costs. The eutectic Al-Si alloys can potentially provide the required combination for use in linerless automotive engine blocks, so studying their tribological performance is of great importance in the effort to optimize the properties of automotive engine block materials.

This research analyzes the microstructures and wear performance of eutectic Al-Si alloys. The wear surfaces of two eutectic Al-Si alloys that had been subjected to engine

tests were characterized to reveal whether or not a correlation exists between engine wear and microstructure. Dry sliding wear tests in air and argon were conducted on a eutectic Al-11% Si alloy using a block-on-ring (SAE 52100 type steel) configuration. The results--which were evaluated to understand the micromechanisms that control Al-Si alloy wear under different environmental conditions--are expected to lend insight into wear resistant alloy design requirements, as well as provide new information for optimizing automotive engine materials.

This thesis is comprised of six chapters. Chapter 1 briefly introduces the subject. Chapter 2 reviews existing literature on the wear behaviour of the Al-Si alloys used in automotive engine blocks, and includes a) an introduction of internal combustion engines and typical automotive engines wear; b) a description of the Al-Si alloys currently used in automotive engine blocks; c) a discussion of the existing wear mechanisms and the effects that Al-Si alloys microstructures have on them; and d) this research's objectives. Chapter 3 describes the experimental methods and materials used in this study, while Chapter 4 characterizes the properties and microstructures of the two eutectic Al-Si alloys chosen for study, and describes their wear performance after engine tests. Chapter 5 presents the results of Al-11% Si alloy wear tests in air and argon, and Chapter 6 summarizes and concludes.

## CHAPTER 2

### LITERATURE SURVEY

This chapter reviews the wear behaviour of the Al-Si alloys used in automotive engine blocks. It begins with a brief introduction of internal combustion engines and the typical wear observed in automotive engines. It then considers the properties, manufacturing processes, and test methods of the Al-Si alloys used in automotive engine blocks. The wear mechanisms and the effects that the Al-Si alloys microstructures (silicon particle size, morphology, and content) have on them are also reviewed. The chapter closes with a description of the objectives for this research.

#### 2.1. Dry and Lubricated Sliding Wear in Automotive Engines

##### 2.1.1. Internal Combustion (IC) Engines

**Fig. 2.1** illustrates the principles of power generation for internal combustion (IC) engines, which convert the chemical energy stored in a mixture of air and liquid fuel into thermal energy within an engine block, then manufacture the thermal energy into mechanical work [9]. There are two main types of IC engines: spark ignition (SI) engines and compression ignition (CI) engines [10]. The common four strokes used by IC engines include the (1) intake stroke, (2) the compression stroke, (3) the expansion or power stroke, and (4) the exhaust stroke—each of which are numbered in sequence in **Fig.2.2**, which shows the relationship between combustion cylinder pressure and cylinder volume [11]. A sideways force is applied to the cylinder bore when the piston moves up and down, and the side thrust load varies with cylinder pressure. The major thrust side bears the large side load and longer contact durations. **Fig.2.3** displays the load



distribution curves on the major thrust side for the top, second and third ring and their overall total as measured from the top ring TDC location along the cylinder wall. The total load distribution is simply the linear combination of the three. The pressure distribution curves for the minor thrust side are given in **Fig.2.4**, and compared with **Fig.2.3**, this load pressure curve shows pressure drops at the second peak and the center portion of the cylinder--resulting from the low side thrust load magnitude, which covered less wall length on the minor thrust side of the cylinder [12].

### 2.1.2 Engine Wear Regimes

Relative motion between two contacting solid bodies produces the potential for sliding wear to occur [13]. Sliding wear can be classified into two categories: dry sliding wear and lubricated wear. The transition from one lubrication regime to another to a dimensionless film thickness ratio can be defined as:

$$\lambda = \frac{h}{\left( \sigma_{surface1}^2 + \sigma_{surface2}^2 \right)^{1/2}} \quad (2.1)$$

Where  $\lambda$  is the film thickness ratio,  $h$  is the film thickness calculated using the application of classical thin film analysis with the assumption that surfaces are smooth, and  $\sigma$  is the root mean square (rms) surface roughness [14].

**Fig.2.5** plots the relationship between the coefficient of friction (COF) and the oil film thickness ratio or Sommerfeld number (=viscosity  $\times$  speed/load). Different automotive components rely upon different modes of lubrication to achieve acceptable performance, and each may experience more than one lubrication regime in a single cycle. The different lubrication regimes are illustrated in **Fig.2.6** [15].

The lubricant films in a hydrodynamic lubrication regime are normally many times thicker than the average surface roughness, and the two sliding surfaces are completely separated by the lubricant film. An elastohydrodynamic lubrication regime depends on local elastic distortion of the solids to provide coherent fluid films for preventing asperity interaction. A boundary lubrication regime features mono or multi-molecular layers of boundary lubricants that interact, with the solids dominating the contact operation. The effects of fluid film are negligible, and there is considerable asperity contact. In a mixed lubrication regime, the contact behaviour is affected by the mixture of boundary and fluid films. Some asperity contact occurs, and an interaction takes place between the mono or multi-molecular layers of boundary lubricating films while a partial fluid-film lubrication action simultaneously involves in the bulk of the space between the solids.

Dry sliding wear occurs when lubricants in the sliding interfaces are absent, such as in the case of cold scuffing in automotive engines. Automotive engine components should operate under ultra-mild wear (UMW) conditions, in which a negligible amount of material is removed. Mild wear is generally attributed to mechanical mixing and/or oxidation, and the sliding surface damage is less extensive when tribological layers cover the worn surfaces [16]. Severe wear involves massive surface damage and the removal or transfer to the counterface of large-scale materials [17]. Transitions from one wear regime to another occur quite abruptly when the contact load or speed is changed. There is no single mechanism of mild wear in dry wear.

### **2.1.3 Factors That Influence Engine Block Wear**

Studying the wear mechanisms between the piston rings and cylinder bore is vital, because the friction between the piston rings and the cylinder bore is responsible for more than 40% of engine power loss [9]. The main factors influencing engine block wear are: a) engine working parameters like speed, temperature, load, and frequency; and b) engine lubricant conditions like gas cleanliness, corrosion, surface finish, and quantity of lubricant [18]. Engine speed has an effect on the sliding wear of bore surfaces because it affects the acceleration forces applied to the rings [19]. Low temperature is a main and frequent source of excessive wear between piston and rings, while high temperature occasionally causes wear by interfering with the lubrication of cylinder surfaces. earlier service failure may result from scuffing which occurs when hot spots induce the distortion or destruction of the oil film.

Scuffing-- defined as “a roughening by plastic flow whether or not there is material loss or transfer” [20] -- is a significantly detrimental form of engine wear damages. There has not been no a consensus among the researchers about its definition. Some investigators described scuffed surfaces as those that were involved in sudden failure, while others defined them as presence of grooves, or transferred material, transferred particles, or other physical features [21]. Scuffing has been sometimes observed between the piston rings and the cylinder bore [22]. Scuffing is usually accompanied by a dramatic increase in friction and a rapid temperature rise that accelerates lubricant degradation. Scuffing prevention depends not only on the duration of the contact and the materials used, but on the surface preparation and the lubricants in the system. In addition to surface roughness, the three-dimensional topography, residual stress, and phase distribution are all involved in the scuffing process [23].

Scuffing occurs in Al alloys when the lubricant film breaks down, or the contact surface temperature reaches a critical temperature [24-25]. The contact pairing between an Al-Si alloy and steel is commonly used in vehicles. Aluminum might transfer to a steel surface even in the presence of a substantial amount of lubricant [26]. The transition from mild wear to severe wear that led to scuffing during unlubricated contact was related to surface temperature [27].

## **2.2 Al-Si Alloys Used in Engine Blocks**

### **2.2.1 Typical Al-Si Alloys Developed for Engine Blocks**

Al-Si alloys used for engine block can be divided into three categories based on their silicon percentage: hypoeutectic ( $<11.7$  wt. %), eutectic ( $11.7$  wt. % to  $12.6$  wt. %), and hypereutectic ( $> 12.6$  wt. %). **Fig.2.7** shows Aluminum-Silicon binary phase diagrams (a), and the typical microstructures of (b) hypoeutectic 319, and (c) hypereutectic A 390 alloys [1]. Silicon can reduce the thermal expansion coefficient, increase wear resistance, and improve an alloy's casting characteristics. When the hypoeutectic Al-Si alloy solidifies, the primary aluminum forms and grows in dendrites or silicon phase forms, growing in angular primary particles during the solidification of the hypereutectic alloy. At the eutectic point, the eutectic Al-Si phases begin to nucleate and proceed to grow until the end of solidification. At room temperature, hypoeutectic alloys have a microstructure that features a soft and ductile primary aluminum phase, and a hard and brittle eutectic silicon phase. Hypereutectic alloys usually contain coarse, angular primary silicon particles and a eutectic silicon phase.

Aluminum alloys with 5-20% silicon that support commercial use usually have some other coexisting elements such as copper, magnesium, manganese, zinc, iron, nickel

or phosphorus. Iron modifies the silicon phase by inducing several Al-Fe-Si phases, and is often used to prevent die sticking in die-casting up to a level of 1.5-2.0%. The network type (Chinese script) Al-Fe-Si phases, however, breaks easily, reducing the wear resistance. Manganese is mainly used to modify the Al-Fe-Si phase and improves the ductility and shrinkage characteristics of the alloy. Magnesium and copper strengthens the material by precipitating hardening, while Nickel improves the alloy's hardness at elevated temperature. Zinc improves heat treatment, but might produce shrinkage, and phosphorus refines the primary silicon phase in a hypereutectic alloy [28]. Typical compositions for commercial alloys are listed in **Table 2.1** [29].

The cylinder block is both the basic and largest framework in a car engine, because it supports all the other engine components. The materials needed to manufacture a cylinder block with high output powers must fulfill the following required functions: good castability and machinability, high heat conductivity, light weight, high strength, satisfactory wear, and scuff resistance. Using aluminum to construct automotive engine blocks offers a potential mass savings in fuel efficiency, and when cylinder blocks are cast of hypoeutectic Al-Si alloys, they require the use of cylinder liners like cast iron sleeves, metal matrix composites, or even AA390. Surface treatments such as plating and coating can also provide wear resistance during operation, but each of these block modifications increases the product's overall cost.

Hypereutectic alloys that have been cast with an appropriate surface preparation such as the etching of the engine bore faces, may achieve a satisfactory performance [30]. The performance of most hypereutectic alloys is limited by low process reliability in casting because of the large sized, irregularly shaped, and unevenly distributed silicon particles. Thus, to use the advantages offered, the hypereutectic aluminium-silicon alloys

should be produced with a controlled small, equiaxed and uniform silicon particle. This is not readily achievable using the conventional casting processes, however.

A near eutectic aluminum alloy with desirable wear resistance can potentially be used to make the linerless engine block of passage vehicles. Clark and Sarkar [31] pointed out that a near-eutectic alloy has the good load bearing capacity. GM patents exist for this kind of Al-Si alloys [32]. **Fig.2.8** shows a linerless engine block made from a eutectic Al-Si alloy.

## **2.2.2 Technologies for Manufacturing Aluminum Cylinder Blocks [33-34]**

### **2.2.2.1 Sand casting**

Sand casting with resin-bonded sand is commonly used to manufacture aluminum components. Cylinder blocks have been produced using the Cosworth process, which is a low-pressure sand casting process used to obtain sound castings. In this process, an electro-magnetic pump fills molten aluminum from the bottom of the resin-bonded mold, and then the slowly solidifying runner portion feeds melt during solidification to generate a porosity-free cylinder block [33].

### **2.2.2.2 Lost Foam Process**

In the lost foam process, a foam pattern made of polystyrene is embedded into unbonded sand and then decomposed by molten metal during pouring. The casting traces the polystyrene shape and the molten metal replaces the foam, precisely duplicating all of the pattern's features [33].

### **2.2.2.3 Die Casting**

In the die casting technique, the mold is permanent and made of die steel. There are three typical die casting processes: i) high-pressure die casting, ii) gravity die casting and iii) low-pressure die casting. In high-pressure die casting, liquid metal is injected into a steel die at high speed and high pressure (around 100 MPa). In gravity die casting, the die is kept at a high temperature so that the molten metal can fill all parts of the casting, and the production cycle time is not always short due to the preparation of the steel die and a long solidification time at high die temperatures. In low-pressure die casting, the die is connected to a pressurized crucible below through a vertical feed tube, and pressures of up to 20 MPa are used. As the chamber is pressurized, the metal level in the feed tube increases. The die temperature should be raised sufficiently until the rising melt metal fills the die with little turbulence and no gas entrapment. Low-pressure die casting is suitable only for a medium-walled casting, and is typically used for the hyper-eutectic Al-Si blocks to obtain a fine dispersion or Si crystals [33].

#### **2.2.2.4 Squeeze Die Casting**

Squeeze die casting is mainly used for aluminum blocks that have a bore wall with a composite microstructure. The technique can cast with the minimum turbulence and gas entrapment by using very large gates and high hydraulic pressure that slowly injects the molten metal into the cavity and pressurizes just before solidification to decrease shrinkage. It can produce porosity-free and heat-treatable components with thick walls, capable of surviving the critical functional testing that is essential for structural automotive parts [33].

#### **2.2.2.5 Other methods**

To produce aluminium alloys that have a high silicon content ( $\geq 20\%$ ) with a fine ( $< 20\text{ }\mu\text{m}$ ) and uniform distribution of the silicon particles, powder-metallurgical (PM) processes or spray forming processes are alternatives to casting processes [34]. Even though PM processes provide considerable microstructural homogeneity of the powder particles, their consolidation by hot extrusion, or hot isostatic pressing involves several intermediate steps. Hot extruded PM products have finely dispersed silicon particles with a size  $< 15\text{ }\mu\text{m}$ , and intermetallics with a size  $< 20\text{ }\mu\text{m}$  [34]. In the spray-forming process, the melt is atomized by a high-pressure gas jet to generate a spray of micron-sized droplets that are subsequently deposited on a stationary or movable substrate to consolidate into a near net-shaped perform. In the spray compacting process, aluminium melt is atomized by high-pressure gas to form a spray of fine metal droplets. The spray-compacted billets are then extruded into tubes, and machined to achieve the final dimensions of the cylinder liner inserts. The engine block is then high-pressure die-cast around the liners inserts.

### **2.2.3 Tribological Methods for Testing Engine Materials**

Three different types of tribological tests can be used in the development of new Al-Si alloys for use in engines: laboratory tests, component tests, and field tests [35]. Laboratory tests are used for the preliminary selection of engine materials and lubricants, and to investigate of the wear mechanisms and the influence of operating conditions like surface pressure, velocity, and working environment. Compared to other tribological tests, laboratory testing is low cost, has short running periods, and the ability to investigate wear mechanisms under controlled conditions. Several different types of tribological testing devices are used in the laboratory tests including pin-on-disk (**Fig.2.9a**), block-on-



ring (**Fig.2.9b**), and reciprocating wear machine (**Fig.2.9c**) [36]. The engine laboratory tests are used to study the tribological behaviour of both the solid body, and the counter-body. Apart from bench-type tribological tests, there are other techniques, like on-line monitoring that include machinery condition monitoring and ferrography/radionuclide techniques [37].

Component tests link laboratory tests and field tests. Component tests running under laboratory conditions are subjected to some simplifications, such as, a controlled environment and/or operating variables. Two common component tests are scuff and dynamometer tests [37]. Field tests operate under very similar conditions to those in practice over long period, but they are expensive and time-consuming, and it can be difficult to control the operating conditions or change test parameters.

## **2.3 Al-Si Alloy Wear**

### **2.3.1 Effect of Normal Load on Wear**

Shivanath et al's early studies in 1970's [38] investigated the wear behaviour of binary sand and chill casting Al-Si that contained up to 20%Si while dry sliding against steel, using pin-on-disk configuration--concluding that these alloys exhibited both mild (oxidative) and severe (metallic) wear. The transition was dependent on the load. Eyre [39] analyzed the wear of Al-Si alloys containing silicon, copper, iron, and nickel while sliding against steels and a gray-cast iron, which revealed that the transition between oxidative and metallic wear occurred when the normal load was increased, as shown in **Fig.2 10**. Metallic wear rates are an order of magnitude higher than oxidative wear rates. Elmadagli and Alpas [40] conducted wear tests on three commercial grade Al-Si alloys using a block-on-ring tester under a controlled atmosphere of 5% relative humidity at a

constant speed of 1m/s. The results were plotted on a logarithmic scale (**Fig.2.11**). The MW regime consisted of two sub-regimes: (MW-1) at low loads, and MW-2 at higher load.

### **2.3.2 Effect of Sliding Speed on Wear**

The sliding speed is another variable that influences the wear rate. In MW, the wear rate first decreased with increasing speed, then reached a minimum at a certain speed, at which point, the wear rate started to increase again [41]. The competition of frictional heat softening and strain hardening determined the down-and-up trend. The up-trend could be suppressed by forced-cooling the surface [43].

Zhang and Alpas [21] investigated the wear performance of a wrought aluminum alloy (6061) under dry sliding conditions using a ring-on-block configuration within a load range of 1-450N and a sliding speed of 0.1-5.0 m/s. Transitions between mild and severe wear were observed (**Fig2.12**), while an increasing sliding speed prompted the transition from mild to severe wear to occur at a lower load.

### **2.3.3 Effect of Temperature on Wear**

In a sliding wear system, most of the friction work done is converted into heat. The increase in temperature may modify the mechanical and metallurgical properties of the sliding surfaces. Generally, strength decreases and ductility increases as the test temperature increases. This general behaviour varies with the structural changes that result from such as precipitation, strain aging, and recrystallization [44].

Zhang and Alpas [21] measured the temperature of the contact surface and calculated the bulk surface temperature using an equation proposed by Ashby [45]. which

indicated that when the bulk surface temperature ( $T_b$ ) exceeded the critical temperature the severe wear occurred. They proposed three different forms of transition between mild and severe wear, load-induced, sliding speed-induced, and sliding distance-induced transitions. The transition between mild and severe wear was also observed in A356 aluminum [46].

Zhang and Alpas [21] also explored the effect of surface temperature on wear mechanisms. Their experimental results in **Fig.2.13** revealed an increase in the bulk surface temperature of 6061Al that correlated to the sliding time and distance under different applied loads. In the mild wear regime, at a combination of low loads and speeds, an initial temperature increase was followed by a decrease to a steady value for the rest of the experiment. At the combination of high test velocities and loads, the surface temperature continuously increased at a high rate up to the point of seizure, which suggested that the attainment of a critical transition temperature triggered the occurrence of the wear transition. They also found that the transition to severe wear could be eliminated by suppressing the temperature of the wear pair to one lower than the transition temperature (**Fig.2.14**) [21].

#### **2.3.4 Effect of Environment on Wear**

Saravanan et al. [47] investigated a 356 grade Al–Si alloy wear mechanisms in commercial purity argon tested against a D2 type tool steel. A mechanically-mixed layer covered the contact surfaces of the Al–Si alloys, and was found to be more stable and homogeneous compared to the layer formed under an oxygen atmosphere. It was also reported that the wear rates in the argon atmosphere tests were reduced by one order of magnitude reduction. Elmadagli and Alpas [46] measured the wear rates and COF of an

Al-18.5 wt. % Si alloy (A390) in dry air and argon environments at different test loads, using a block-on-ring (SAE 52100-type steel) configuration (shown in **Fig.2.15**), which revealed that the wear rates of the A390/52100 steel pair tested in argon were always lower than those measured in dry air with 5% RH. The difference was especially significant at low loads, with a 10-fold reduction in the magnitude of the wear rates occurring at 10 N. Similarly, the tests performed in argon resulted in lower steady-state COF values of  $0.29 \pm 0.02$  compared to the  $0.57 \pm 0.08$  measured in air. The tribolayers formed in argon were compacted, and covered the contact surfaces continuously. On the other hand, the surfaces of the samples tested in air were covered by iron-rich oxidized tribolayers that were easy to spall. Fretting wear tests conducted by Goto et al. [48] on an Al-4% Zn-2% Mg alloy revealed that when this alloy was tested against itself, the steady-state COF values reached as high as 1.2 in dry air, while a lower COF of 0.6 was obtained from the tests done in a dry argon atmosphere. The average wear volume increased along with the relative humidity (RH) in the test chamber.

Yen and Ishihara [49] investigated the effects of humidity on the friction and wear of Al-Si eutectic alloys and Al-Si alloy-based composites. Experiments were conducted in an RH range of 1-95%, using a cast iron counterface. The wear rate of the eutectic Al-Si alloy did not vary significantly with the humidity content up to 70 % RH, but the wear rate decreased by two orders of magnitude in a humidity range of 70 –95% RH.

Brainard and Buckley [50] constructed a tribometer for the dynamic observation of aluminum friction and wear, in addition to other metals, inside a scanning electron microscope (SEM) during experiments conducted at a pressure of  $10^{-6}$  to  $10^{-7}$  Torr. The results showed that aluminum sliding on aluminum produced a high COF of 0.82 as a result of adhesion between the two surfaces. In contrast, X-ray maps of aluminum sliding

against a steel pin demonstrated that iron transferred to the aluminum surfaces, and that the transferred iron fragments became embedded in the aluminum matrix. Small, discrete transferred aluminum pieces were randomly distributed on the steel pin. Glaser [51] studied the wear behaviour of pure aluminum in vacuum at  $10^{-5}$  Torr with a similar wear apparatus, using a ball (SAE 52100 steel)-on-flat configuration. The results indicated that the adhesion of aluminum to steel occurred during the first pass, with considerable damage to the aluminum contact surface manifesting through the formation of periodic surface features, due to a stick-and-slip process. Loose debris was formed by either the lateral or vertical extrusion of the material outside the boundaries of the contact surface.

Gravier et al. [52] performed dry sliding wear experiments on Al–1.5% Mn–1% Mg against an H13 type steel in an environmental tribochamber under vacuum and air environments, with different humidity levels. It was noted that the COF in dry air and vacuum ( $3 \times 10^{-7}$  Torr) was the same (0.6), but an increase to 0.8 occurred at high humidity levels. It was also reported that an increase the wear and friction of aluminum followed an increase in humidity, which was attributed to the ploughing of the surfaces by hard oxide wear debris. Yen [53] observed that the wear rate of an Al–12% Si–1.2% Ni alloy tested against a cast iron counterface actually decreased by two orders of magnitude when the relative humidity level in the atmosphere rose above 70% RH--contributing to the formation of an iron oxide-rich film. Yen and Ishihara [54] tested an Al–12% Si–1.2% Ni alloy with 55 vol % graphite addition, and observed that a relatively high COF of 0.5 in air with 1% RH was reduced to 0.2 in ambient air with 35% RH. This behaviour reflected the effect of atmosphere on the COF of carbon, which displayed high friction in dry nitrogen, and a lower friction in wet nitrogen. Goto and Uchijo [55] also noted the same type of dependence between wear behaviour and the humidity.

### **2.3.5 Tribolayer Formation**

Section 2.3.4 illustrates how testing in air produced very different from testing in inert environments. In air, the surfaces were normally contaminated with a layer of absorbed gases, hydrocarbons and moisture [56]. Below this layer, there exists a reaction zone that consisted of metals, typical elements from the two mating materials, their metal oxidants or sulfide and/or intermetallic, with a thickness of the order of 10 nm thick [57]. The thickness of this layer depends on the load, speed, and temperature. The tribolayer prevents metal to metal contact during sliding and one of the factors affecting the properties of this tribolayer is the atmospheric humidity present during sliding wear. In a tribo-system, the tribolayer can only be produced after at least one performance of a sliding motion. After an initial sliding, the tribolayers first appear at the contacting asperities, and continue to grow and expand to include whole real contact areas until the occurrence of seizure [58].

Elmadagli and Alpas [46] observed that the process for A390 tested in an argon atmosphere was initiated with the formation of iron-rich transfer films on the surfaces of the exposed Si particles. The composition of the layers changed during sliding, with aluminum-rich tribolayers forming during the steady-state wear at long sliding distances. These layers were compacted and provided continuous coverage of contact surfaces. In contrast, the surfaces of the samples tested in air were covered by iron-rich tribolayers that were oxidized and easy to spall. The depth of the damaged zone in the material underneath the tribolayers was smaller in the samples tested in argon than in those tested in air, because the air environment generated higher subsurface plastic strains during sliding wear.

Previous studies have revealed that a very large shear strain commonly developed at the interfaces of ductile materials [59]. The resulting mixing of the materials from the two sides produced a mechanical mixed layer (MML). Observation of the MML in a variety of materials revealed a refinement in the microstructure near the interface, along with hardness and strain gradients normal to the interface. Many methods, including SEM and TEM observation of cross-sections from worn surfaces and micro-hardness measurements of the subsurface have commonly been used to investigate the MML.

### **2.3.6 Effect of Microstructure on the Wear**

#### **2.3.6.1 Volume Fraction for Si Particles**

There have been many attempts to study the effect that silicon content has on the wear behaviour of the Al-Si alloys, with a variety of conclusions—particularly regarding to the effect of silicon content on the dry sliding wear of Al-Si alloys as obtained in past studies. Shivanath et al [38] studied the wear of Al-Si binary alloys containing 4, 8, 11, 16, and 20% silicon under dry sliding condition, and concluded that the mild wear rate (oxidative wear rate) was independent of the silicon content, silicon particle size and applied load as well. Only the transition from mild wear to severe wear increased when the silicon content increased, as shown in **Fig. 2.15**. Antoniou et al [60] also found that increasing in the silicon content from 8.6 to 14.2% extended the load range, in which fine equiaxed particles were produced.

Clarke and Sarkar [61] investigated the wear behaviour of as-cast binary Al-Si alloy pins with up to 21wt% Si, using a pin-on-bush type machine where the bush material was hardened steel. The results revealed that the wear resistance in these alloys increased up to a near eutectic composition (13 wt% Si), and their seizure resistance also

increased along with the silicon content (seen in **Fig. 2.16**). Jasim and Dwarakadasa [62] observed that a minimum in the wear rate at the eutectic composition during the dry sliding wear of binary Al-Si alloy (3-22 wt% Si) pins with a 6 mm diameter, tested against steel disks with hardness of 30 and 50 Rockwell-C, in a pressure range of 6-195 kPa and a speed range of 58-580 cm/s in an uncontrolled air atmosphere.

Mohammed et al [63] investigated the wear of Al-Si alloys containing 3 –22%Si when sliding against steel under unlubricated sliding conditions, in bearing pressure and sliding speed ranges of 6-195 kPa and 58-580cm/s, respectively. The results indicated that the wear rate for aluminum alloys was reduced by the addition of silicon until it reached a minimum value right around the eutectic composition. Further addition of silicon increased the wear rate, and revealed the fact that the effects of silicon were more pronounced at intermediate pressures than at high pressures.

Reddy et al [64] investigated the wear and seizure of binary Al-Si alloys containing up to 23% Si under dry sliding conditions, using a pin-on-disk configuration, and concluded that the wear characteristics of Al-Si alloys containing 7, 13 and 17% Si exhibited distinct different mild wear, severe wear and seizure regimes. An alloy containing 23% Si exhibited only mild and severe wear regimes and did not show seizure.

#### **2.3.6.2 Effect of Silicon Morphology on Wear**

Cleg and Das [65] used sodium and sulphur to modify the eutectic silicon and refine the primary silicon of a hypereutectic Al-Si alloy composed of Al-17%Si-4.81%Cu-0.59%Mg (wt%), respectively. They then studied the influence that the eutectic silicon modification and the primary silicon refinement had on wear under dry sliding conditions, with a pin-on-ring type (10 mm pin diameter) wear test. The results at loads of



2.5 and 4.5 kg and a constant speed of 1m/s showed that structural modification and refinement did not have a significant effect on the wear rate of the alloy. Shivanath et al [38] studied the effects of varied silicon particle size on wear by using different processing routes, such as sand casting, chill casting, and modification—all of which indicated that different Si particle sizes did not have an effect on wear. They concluded that the mild wear rates of Al-Si alloys were independent of Si-particle size.

Barber et al [66] used chromium-plated steel rings as the counterface material in a reciprocating wear machine to explore the effect of Si particle size and chemical etching on the lubricated wear rates and scuffing resistance of Al-Si alloy 390. The silicon particle size in as-cast samples was approximately 40  $\mu\text{m}$ . A high-energy source was used to remelt the aluminum alloy surfaces and modify the near surface silicon particle size. In this way, samples with a remelted surface layer about 2.4 mm thick and an average Si particle size of 5  $\mu\text{m}$  were produced. The remelted specimens displayed the highest scuff resistance possibly due to the smaller silicon particle size or the presence of the Si ‘clumps’ in the remelted specimens. An electrochemical process was used to etch the alloy surfaces, but etching did not alter the lubricated wear rates of the as-cast samples. The remelted and etched specimens exhibited the highest wear and the worst scuffing resistance, both of which were attributed to the lack of near surface silicon that might have been removed by the etching process in the remelted and etched specimens. While, this study clearly showed that remelting improved the scuffing resistance, the effect of silicon particle size was still not conclusive.

Srivastava et al [67] investigated the microstructure and wear properties of a hypereutectic Al-Si alloy (Al-20.27%Si-1.46%Cu-0.55%Mg-1.22%Ni-0.75%Fe-0.33Ti-

0.6%Mn) by casting the alloy in two different ways: a spray casting process and a conventional casting process. The primary Si size in the spray alloy was in the range of 2-5  $\mu\text{m}$  compared to the primary Si size of 70-130  $\mu\text{m}$  in the as-cast alloy. They used a pin-on-disk type wear testing machine to perform the experiments at load and speed ranges 6-8 kg and 0.3-1.5 m/s, respectively. Their results indicated that the wear rates of the spray-formed alloy were comparable to those of the as-cast alloy, with only slight differences.

Zhang and Alpas [68] studied the dry sliding wear behaviour of a cast Al-7%Si alloy (356) reinforced with 10-20% SiC particles, using a block-on-ring type tribometer, which revealed that under the conditions in which applied stress was lower than the fracture strength of the particles, the SiC particles served as load bearing elements. Their abrasive action on the counterface led to the detachment of iron layers, which were then oxidized and transferred to the contact surfaces. This process led to a tenfold increase in the wear resistance of the composites, with respect to the unreinforced alloy, and a new regime--ultra-mild wear (UMW)--was attained. The particles' size and volume fractions determined the transition load from this low wear rate regime to the mild wear (**Fig. 2.17**). Riahi and Alpas [69] investigated the scuffing resistances of two 12% Si eutectic Al-Si alloys, measuring it with electrical resistance applied during sliding tests and revealed that the resistance between the steel pin and the Al-Si samples decreased when scuffing occurred. While both alloys contained the same second-phase particles with similar volume percentages, they displayed different morphologies. Their results showed that the alloy containing a larger number of second-phase particles with smaller aspect ratios exhibited better scuffing resistance.

Silicon particles play an important role in an Al-Si alloy the wear resistance. The general mechanism responsible for an increase in the wear resistance of an Al-Si alloy is that silicon can increase the overall hardness of the alloy, making it more resistant to wear. This does not always mean, however, that the higher the fraction of silicon in the alloy, the greater the alloy's wear resistance. Due to its high brittleness, impact load can break silicon and thus may increase the overall wear of the alloy, so the optimal fraction and morphology of silicon in an Al-Si alloy is a vital key to improving its wear performance.

## **2.4 Wear Regimes and Mechanisms of Al-Si Alloys**

The UMW has been observed with one or two orders of magnitude lower than mild wear under light loads and at small speeds [57], as well as in inert atmosphere [46]. Al-Si alloys intended for use in automotive engine components are expected to operate under ultra-mild wear (UMW) conditions, where a negligible amount of material is removed [71]. Basically, the UMW occurs at lower loads and sliding speeds, when the wear rate is lower. The contact surface is covered by compacted layers. Riahi and Alpas [52] studied the sliding wear resistance of an A30 type grey cast-iron against an AISI 52100 type steel within a load range of 0.3–50.0 N and a sliding speed range of 0.2–3.0 m/s, using a block-on-ring wear machine. In the UMW regime, the wear rates were  $8 \times 10^{-7}$  and  $9 \times 10^{-7}$  mm<sup>3</sup>/m at 0.3 N for 0.2 and 0.5 m/s, respectively. The contact surfaces were covered by compacted iron oxide layers. S. Wilson and Alpas[44] also used a block-on-ring (SAE 52100) configuration to perform experiments with an A356 Al alloy and an A356 Al--20%SiC composite in dry sliding conditions, within a load range of 0.2–400 N and a sliding velocity range of 0.2–5.0 m/s. From their observations, wear transition in the composite shifted from mild to ultra-mild occurred at low loads and

velocities, with two sub-regimes existed for both materials within the mild regime. The UMW wear rates for the composite were at least two orders of magnitude lower than for unreinforced A356 Al.

Riahi and Alpas [46] systematically studied the role played by the tribolayers that formed on the contact surfaces of A356 Al–10% SiC–4% Gr and A356 Al–5% Al<sub>2</sub>O<sub>3</sub>–3% Gr during the sliding wear. The wear rates for the A356 Al–10% SiC–4% Gr composite in the ultra-mild regime ranged between  $1 \times 10^{-7}$  and  $7 \times 10^{-6}$  mm<sup>3</sup>/m. The effect that test speed had on the UMW rates was small in the speed range studied, and the transition between the ultra-mild and mild wear was relatively insensitive to the test speed. Elmadagli and Alpas [40] investigated the effects of environmental conditions--including an air atmosphere with high humidity (95% RH) and an inert argon gas atmosphere--on the wear rates and mechanisms of a A390 alloy. The alloy attained UMW rates at light applied loads that coincided with the MW in the dry air atmosphere (5% RH) in both humid air and argon atmospheres. UMW rates were approximately one order of magnitude lower than MW rates, and the wear mechanisms were controlled by the compositions and properties of the tribolayers formed on the worn surfaces. **Fig.2. 18** [40] shows the wear rate vs. load curve of A390 tested in an argon atmosphere, and those generated in air with 5% RH and 95% RH. A comparison of volumetric wear and COF for the A390 samples tested in argon and air (5% RH) atmospheres at a light load of 10 N is illustrated in **Fig.2.19 a–b** [40]. The average COF value and the average value fluctuations were lower during the test in argon, correlating with lower wear rates observed in the same test.

M. Chen, T. Perry, and A. T. Alpas studied UMW in five chemically etched Al-Si alloy surfaces from 11 to 25 wt.% Si, using a pin-on-disc tribometer at low loads (0.5-2.0

N) under boundary lubricated conditions. They found that Al-11% Si with small silicon particles exhibited optimal long-term wear performance [71].

The MW regime is characterized by relatively low wear rates ( $10^{-4}$  to  $10^{-3}$  mm<sup>3</sup>/m), and the formation of a dark, colored compacted layer on the worn surfaces. The distinction between mild and severe wear, however, is not always on the basis of differences in wear rates. The worn surface morphologies and the debris vary as well. Shivanath et al [38] studied the dry sliding wear of binary Al-Si alloys with up to 20 wt% Si, and contributed the formation of the compacted layer on the worn surface to the oxidation of aluminum. Antoniou and Borland [61] believed that the oxidation of aluminum did not play a significant role in MW and suggested that an iron-rich layer composed of an ultra-fine mixture of Al, Si, and Fe was what formed on the Al-Si surfaces. Zhang and Alpas [21] revealed that the debris generated during the mild wear of 6061 Al was partially amorphous, as identified by their XRD analyses.

Severe wear has been observed under higher loads with a sharp increase in wear rates. The worn surfaces are characterized by plastic deformation and fracture, local transfer of material, and the formation of flake-like metallic wear debris. Jasim and Dwarakadasa [63] discussed these two wear mechanisms--mild wear and severe wear--and a combination of them at intermediate load levels during the dry sliding wear of Al-Si alloys in ambient air environments. Wilson and Alpas [70] studied the effects that experimental conditions had on wear mechanisms when an A356 alloy slid against SAE 52100 steel. They constructed a wear map for this alloy and classified their results in terms of two main wear mechanisms, namely mild wear and severe wear. They observed that two sub-regimes existed within mild wear: i) a mixing/oxidation sub-regime at low speeds, where the worn surfaces were covered by tribolayers; and ii) a sub-regime where

delamination at higher speeds led to the removal of material next to the contact surfaces. This mechanism was modeled by Zhang and Alpas [21], who considered the competition between the subsurface plastic strain that enhances void growth, and the hydrostatic pressure that suppresses it. Researchers [60-62] observed the following mild wear mechanisms:

- (i) The formation and compaction of oxides that later detach as debris;
- (ii) The delamination of layers due to a process of transfer and back transfer, and the subsequent detachment of debris from these layers;
- (iii) The delamination of debris from a plastically deformed surface containing finely dispersed silicon particles;
- (iv) The formation of a compacted layer on the surface, consisting not of oxides but of an ultrafine mixture of aluminum, silicon and iron. The debris essentially consisted of laminates produced by fracturing compacted material or fine particles of the mixture.

## **2.5 Research Objectives**

The objectives of this research are to improve the current understanding of requirements for commercial wear resistant Al-Si alloy design and provide new information for optimizing automotive engine materials by studying the wear performance of the eutectic Al-Si alloys used in linerless automotive engines. Two eutectic Al-Si alloys engine bores were characterized and compared after engine tests, and dry sliding wear tests were conducted in air and argon on a selected 11% eutectic Al-Si alloy to clarify the effects of test environment on sliding wear when analyzing the micromechanisms that control Al-Si alloy wear under different conditions. The results helped explain these micromechanisms, especially at higher loads (first in inert

atmosphere as my understanding), and were compared with those for A390, as found by M. Elmadagli [46].

**Table 2.1** Chemical composition of the selected typical commercial Al-Si alloys [29]

<b>Alloy</b>	<b>%Si</b>	<b>%Cu</b>	<b>%Fe</b>	<b>%Mg</b>	<b>%Mn</b>	<b>%Ni</b>	<b>%Ti</b>	<b>%Zn</b>
<b>319</b>	5.5-6.5	3-4	1	0.1	0.5	0.35	0.25	1
<b>A356</b>	6.5-7.5	0.2	0.2	0.25-0.45	0.1	-	0.2	0.1
<b>A380</b>	7.5-9.5	3-4	1.3	0.1	0.5	0.5	-	3
<b>A390</b>	16-18	4-5	0.5	0.45-0.65	0.1	-	0.1	0.2



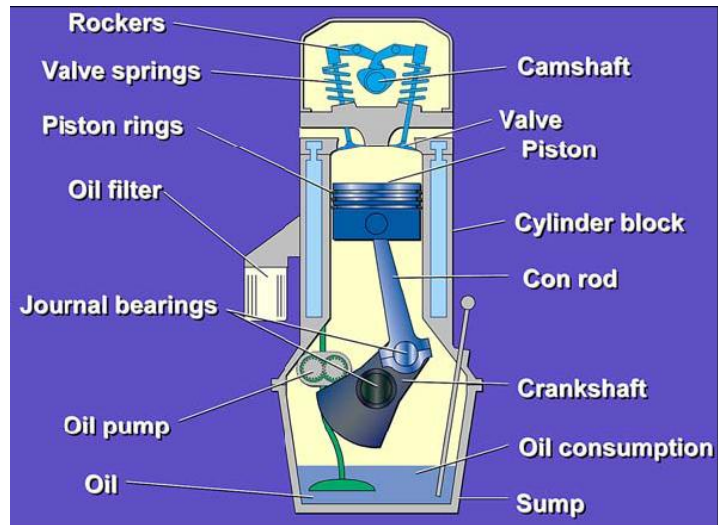


**Fig.2.1** Main components of an internal combustion engine [9].

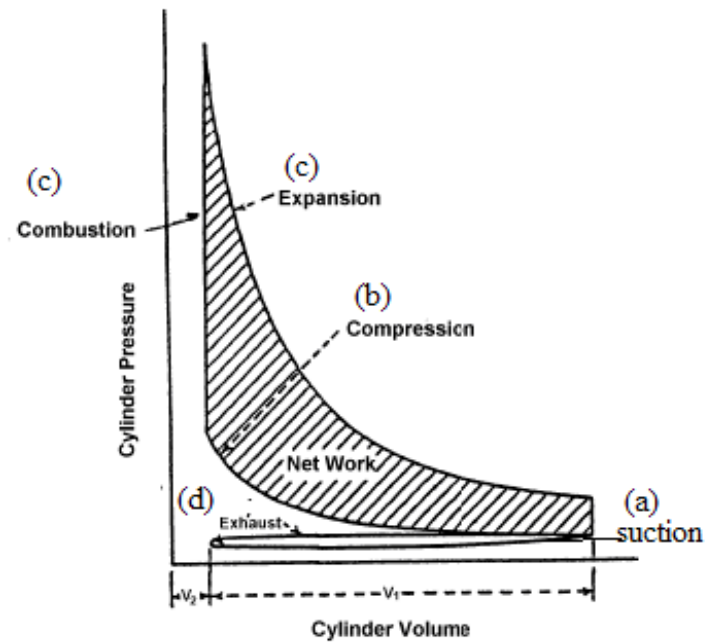


**Fig.2.2** P- $V_0$  diagram for four-stroke cycle IC engine [11].

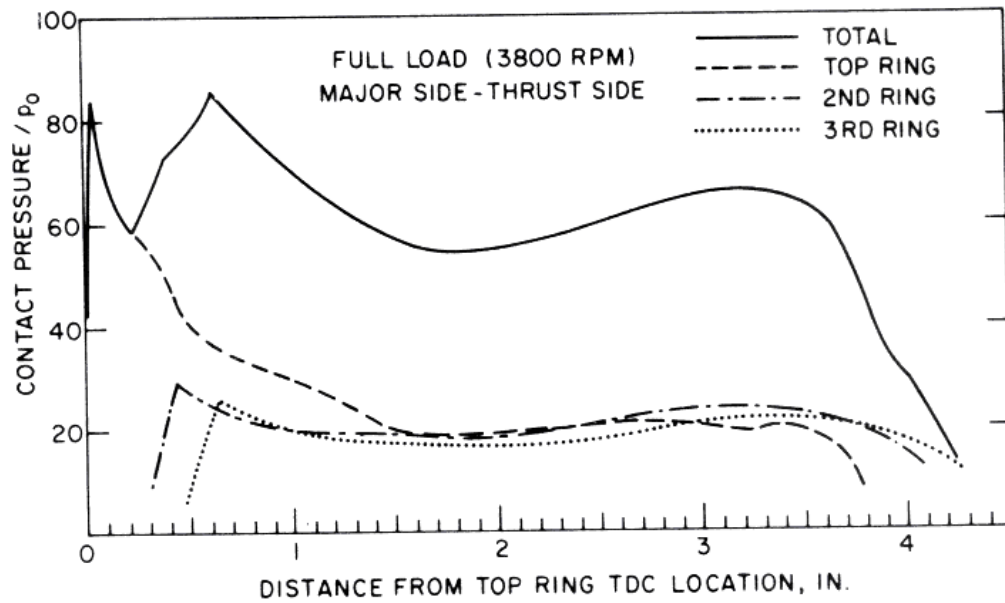


**Fig.2.3** Pressure load distributions on major side-thrust cylinder wall per cycle- full load, 3,800 rpm (1 in. =25.4mm)[12].

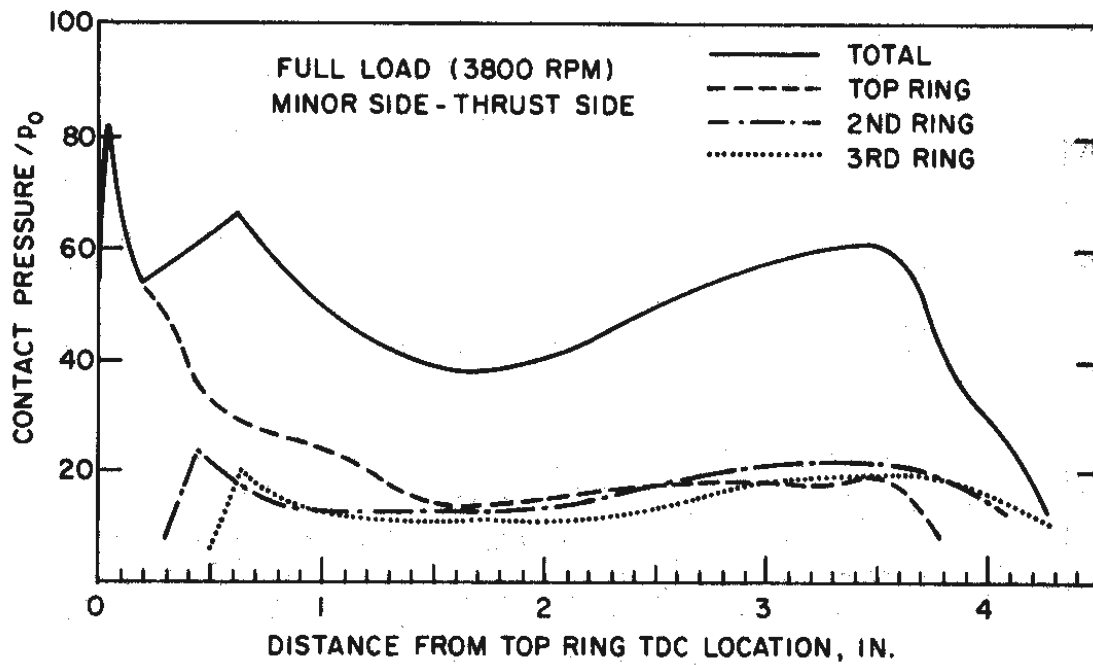


**Fig.2.4** Pressure load distributions on minor side-thrust cylinder wall per cycle- full load, 3,800 rpm (1 in. =25.4mm)[12].

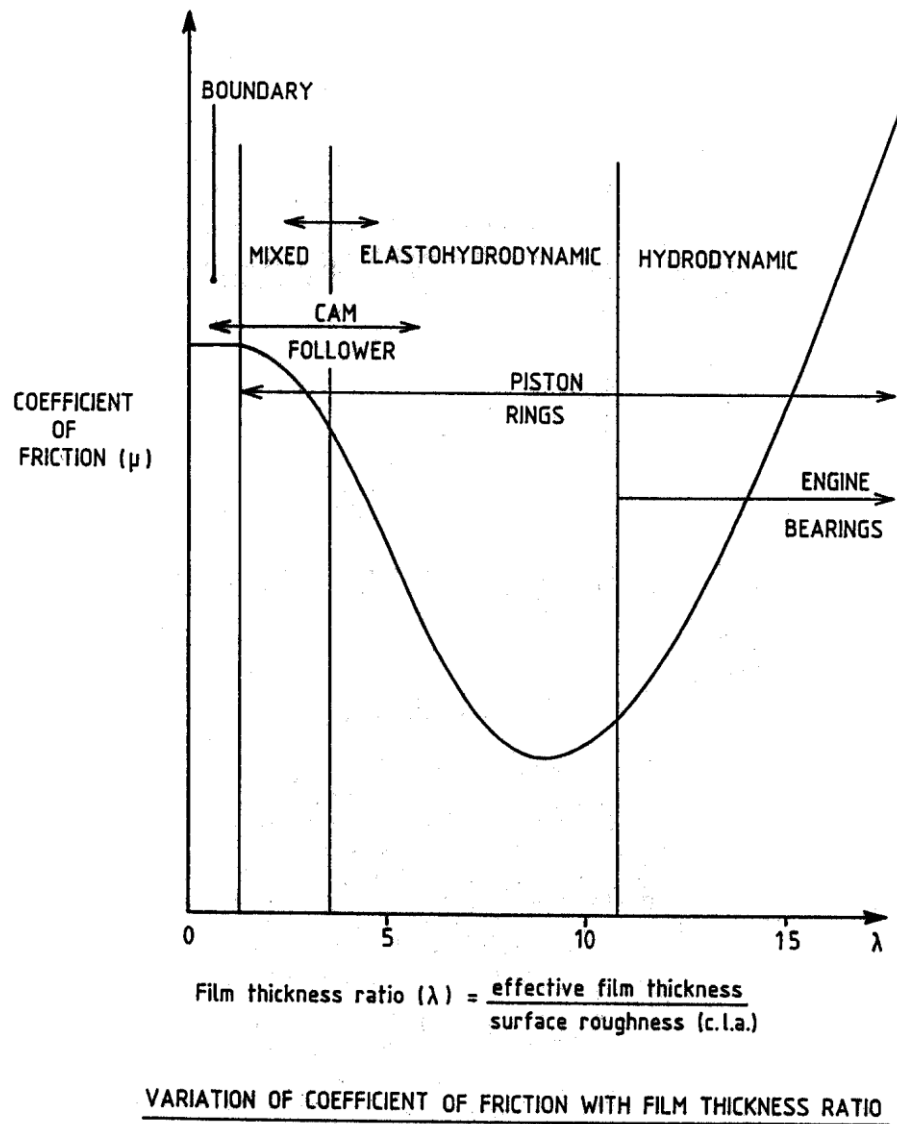
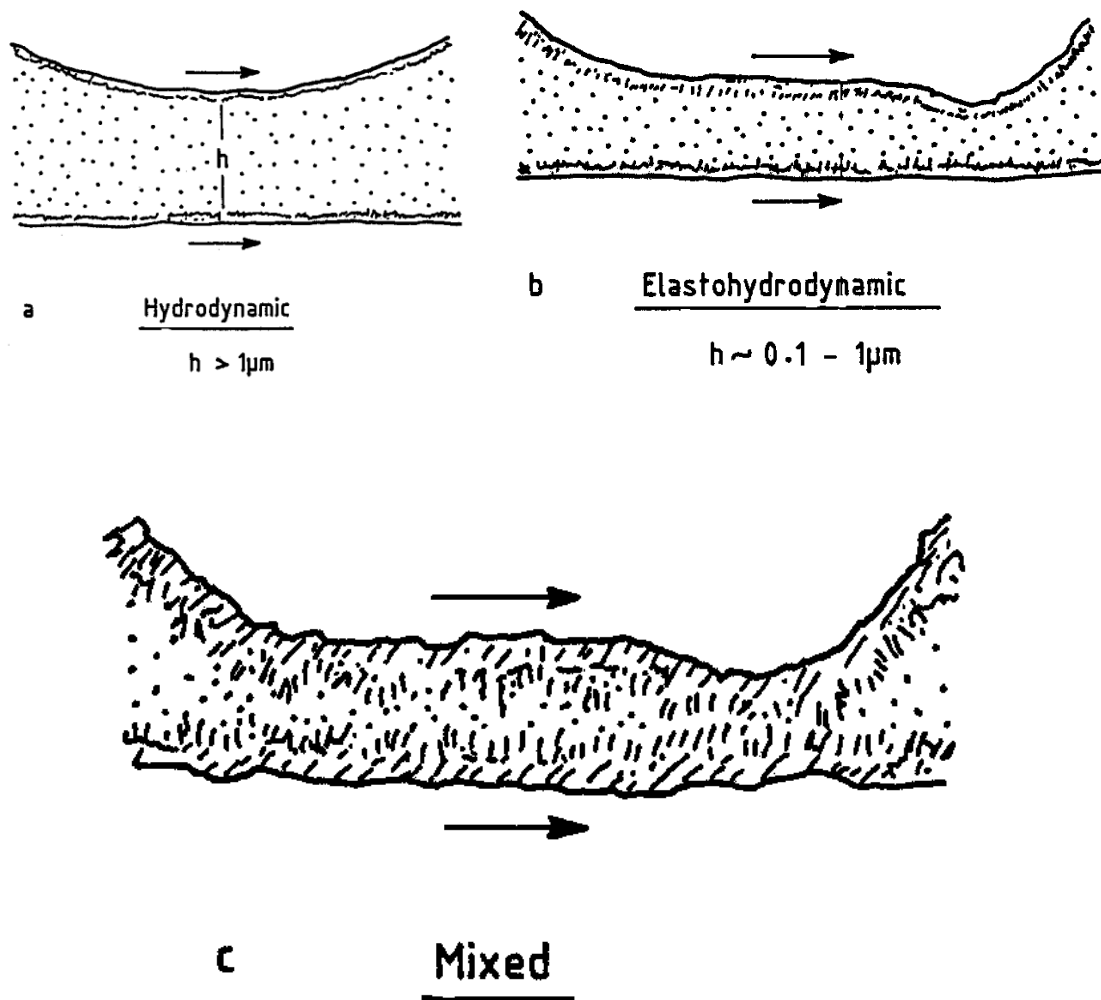
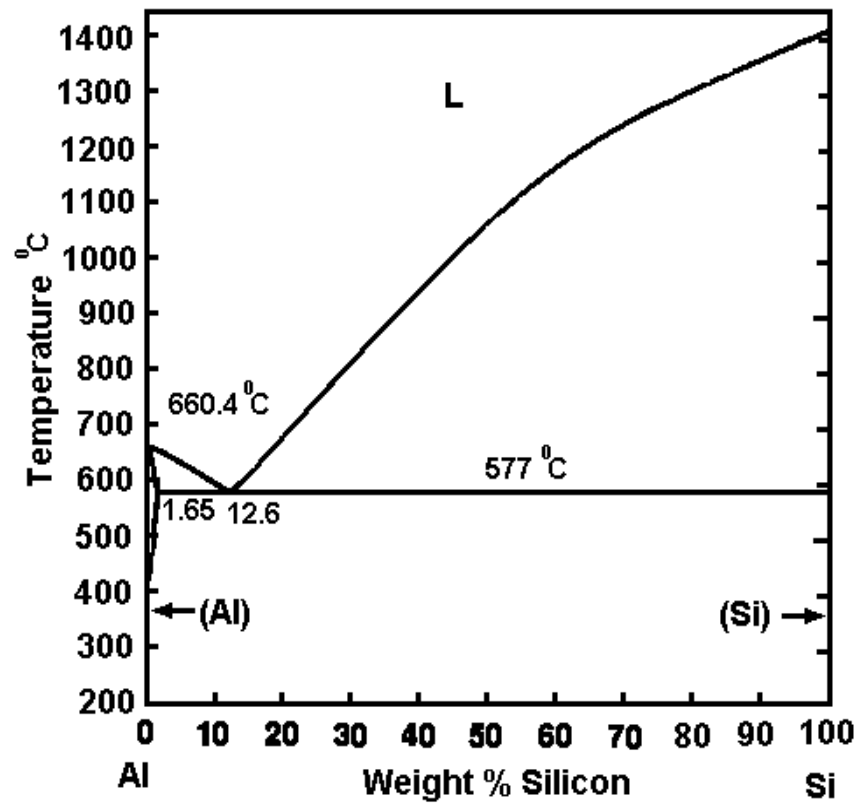


**Fig.2.5** The relationship between the coefficient of friction and the oil film thickness ratio [15].



30 Å boundary lubricant molecule (3nm)  
 10 - 50 Å oxide layer (1 - 5nm)

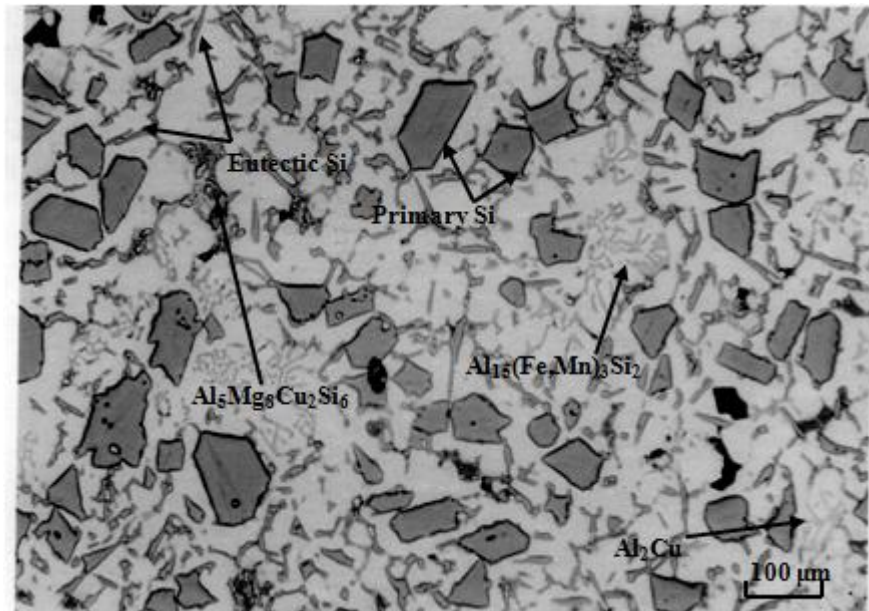
Fig.2.6 The lubrication regimes discussed above in Fig.2.5 [15].



(a)



(b)



(c)

**Fig.2.7** Aluminum-Silicon binary phase diagrams (a) and typical microstructures of (b) hypoeutectic 319 and (c) Hypereutectic A 390 alloy [1].

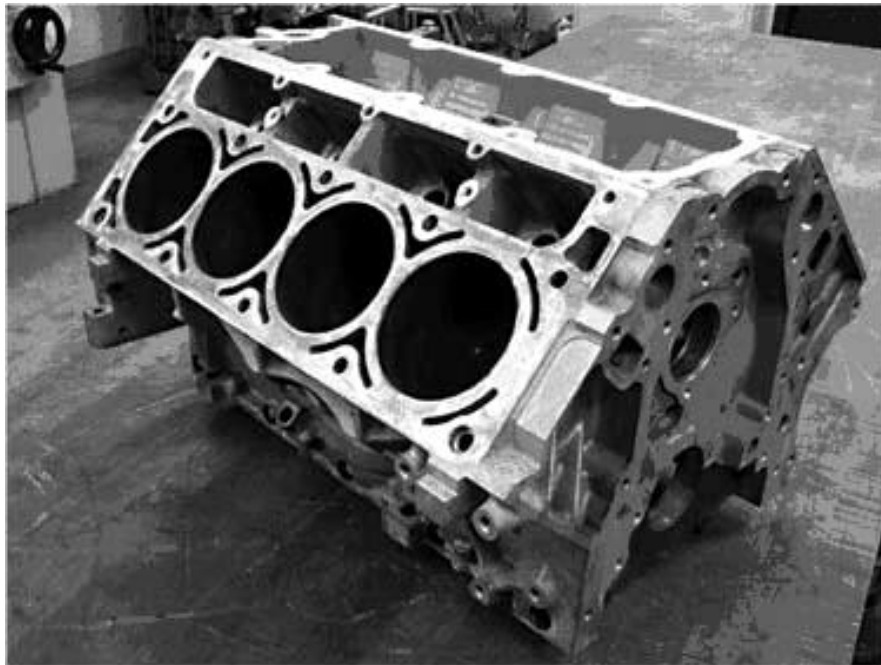


**Fig.2.8** Illustration of a linerless engine block made from a eutectic Al-Si alloy from GM

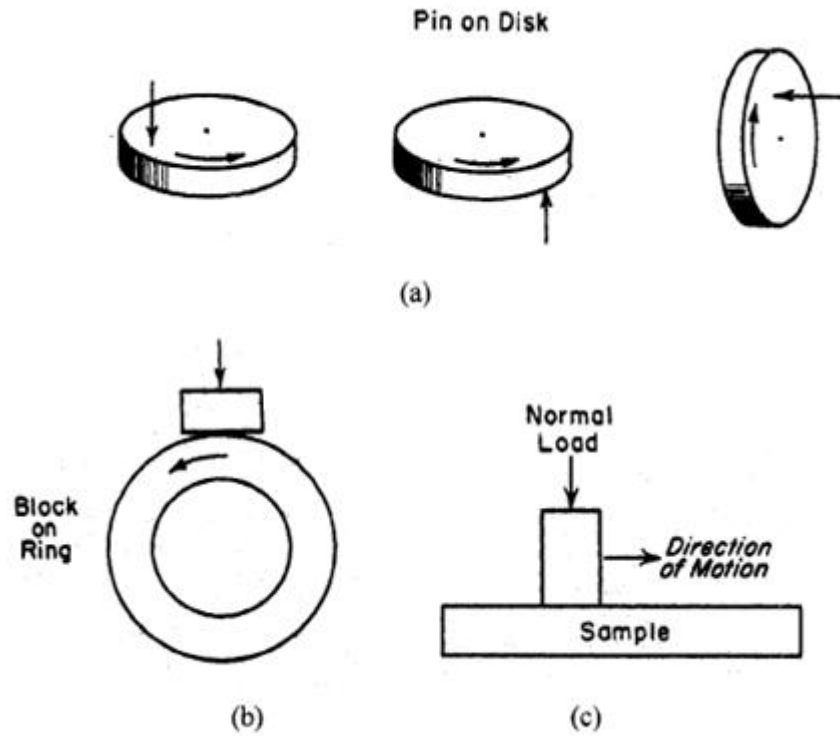


**Fig. 2.9** The pin-on-disk wear test machine]: a) three different arrangements for a simple pin-on-disk wear test machine; b) block-on-ring wear machine; c) reciprocating wear machine [36].

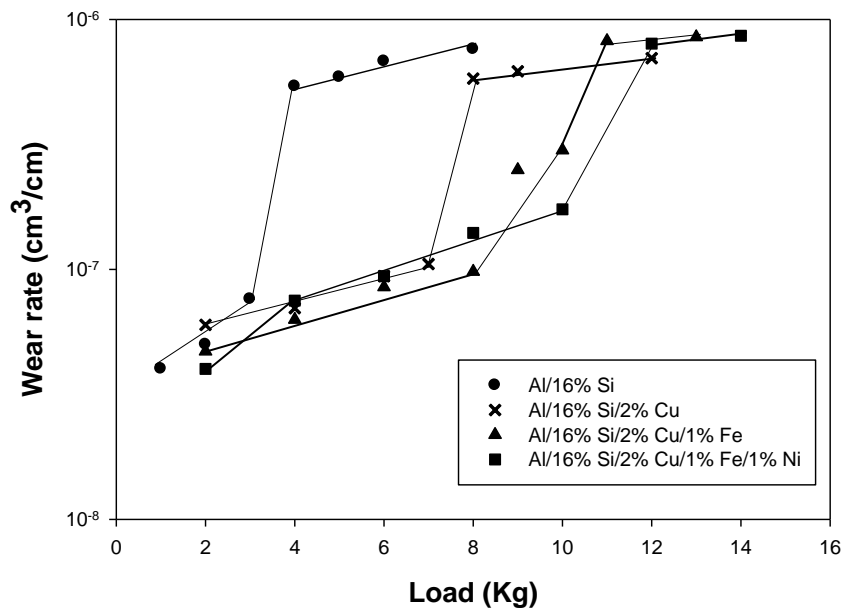


**Fig. 2.10** Variations of wear rate of four Al-Si alloys with normal load [39].

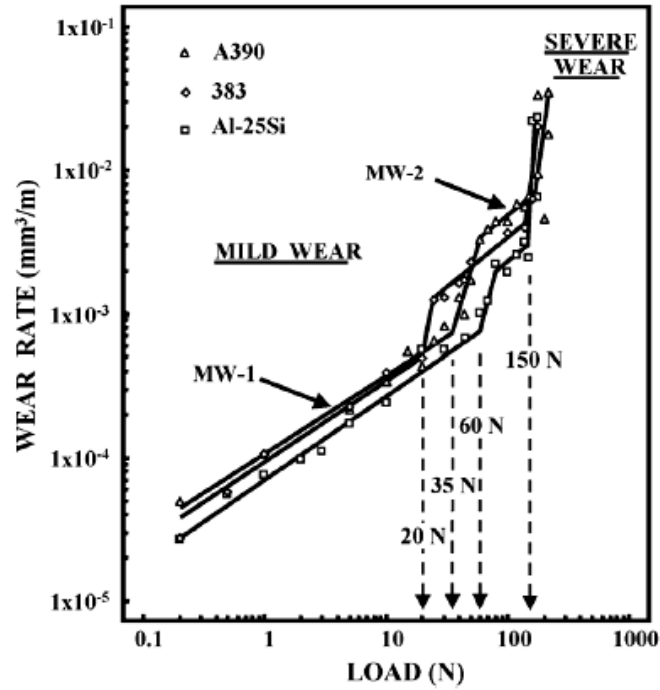


**Fig. 2.11** Wear rates of the as-received A390, 383 and Al-25Si alloys plotted against load on a logarithmic scale. The two sub-regimes of mild wear MW-1 and MW-2 are separated by a transition regime. The loads 20, 35, and 60N correspond to the highest load in MW-1. The transition from MW-2 to the severe wear regime occurs at 150N for all the alloys [40].

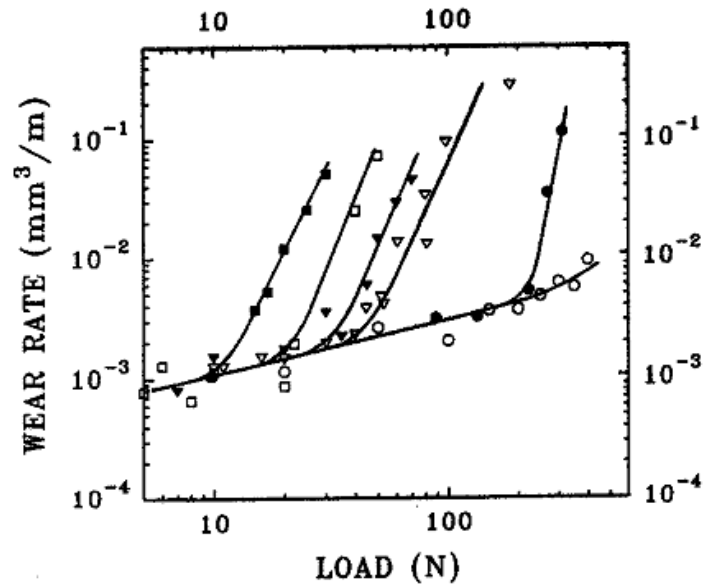
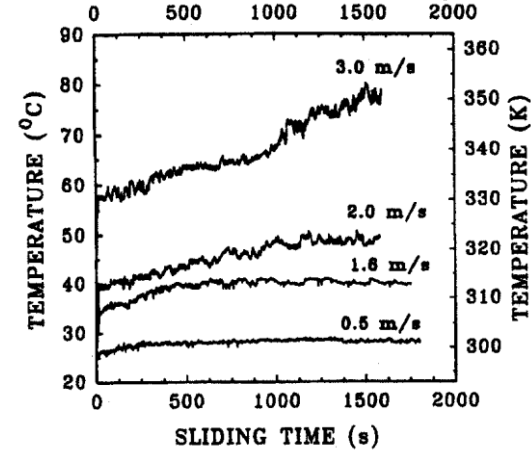
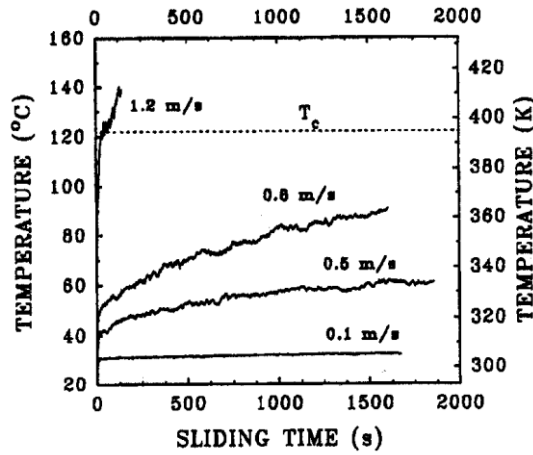


**Fig. 2.12** Variation of wear of 6061 aluminum with normal load at different sliding speeds [21].

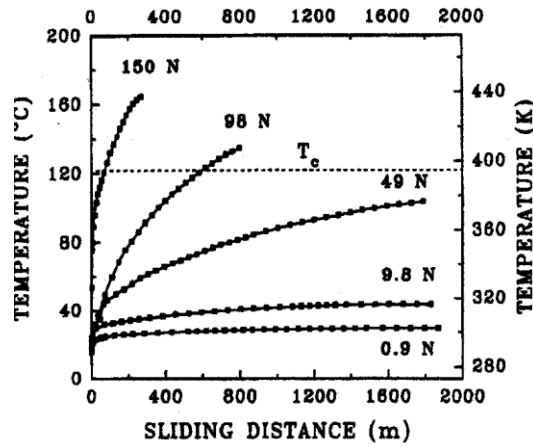




(a)



(b)



(c)

**Fig. 2.13** (a) Contact surface temperature versus sliding time plots at different velocities at a constant load of 5.0 N; (b) contact surface temperature versus sliding time plots at 50N; (c) contact surface temperature versus sliding distance plots at different loads at a constant sliding velocity of 0.8m/s [21].

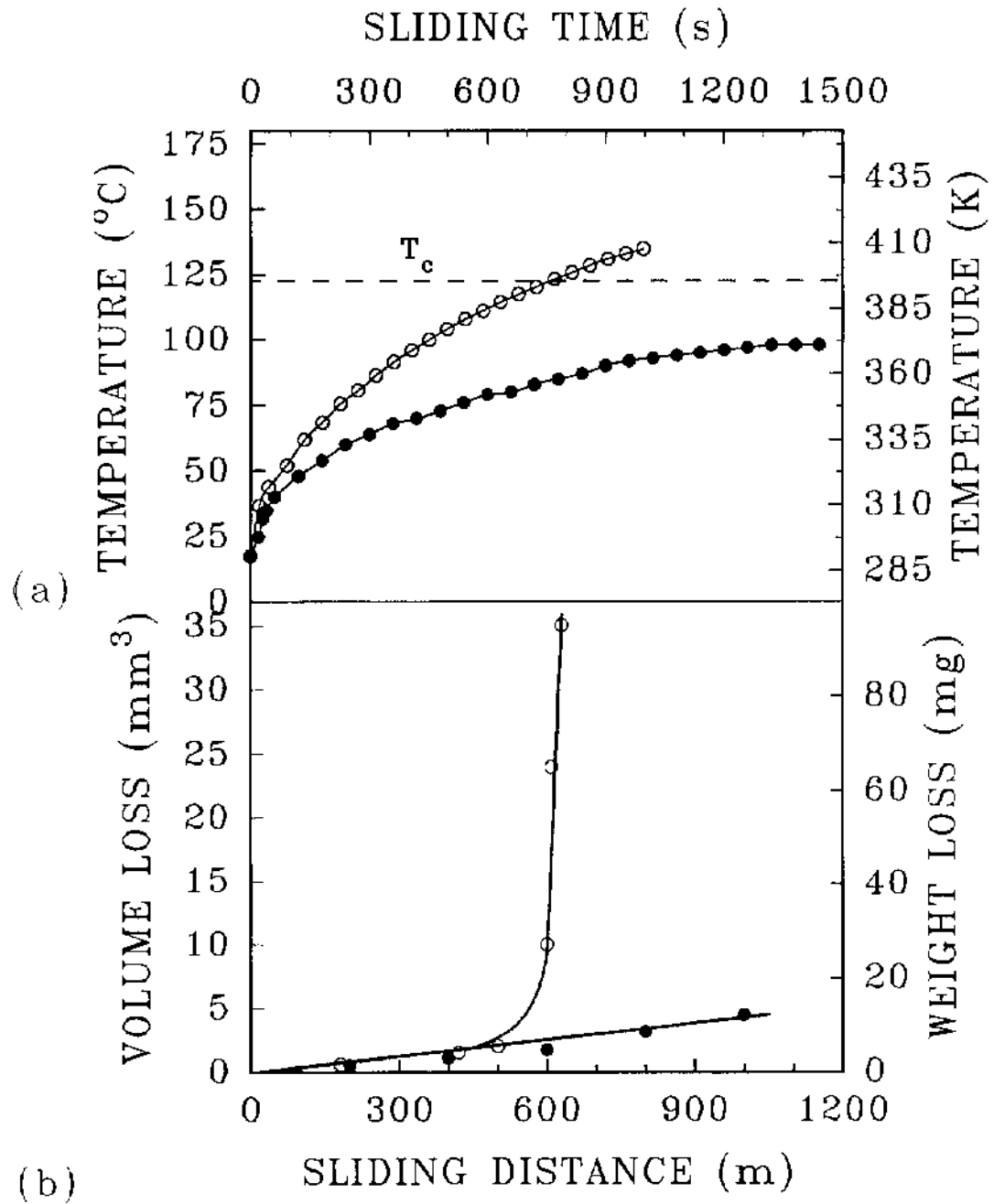


**Fig.2.14 (a-b).** Effect of forced cooling by chilled water on the mild to severe wear transition in 6061 Al worn against SAE 52100 steel. Without cooling the contact temperature exceeds  $T_c$  (395k) leading to severe wear (○). Cooling the system will ensure that the contact surface temperature stays below 395k, thus only mild wear is observed (●). Load =98N,  $v=0.8\text{m/s}$  [21].

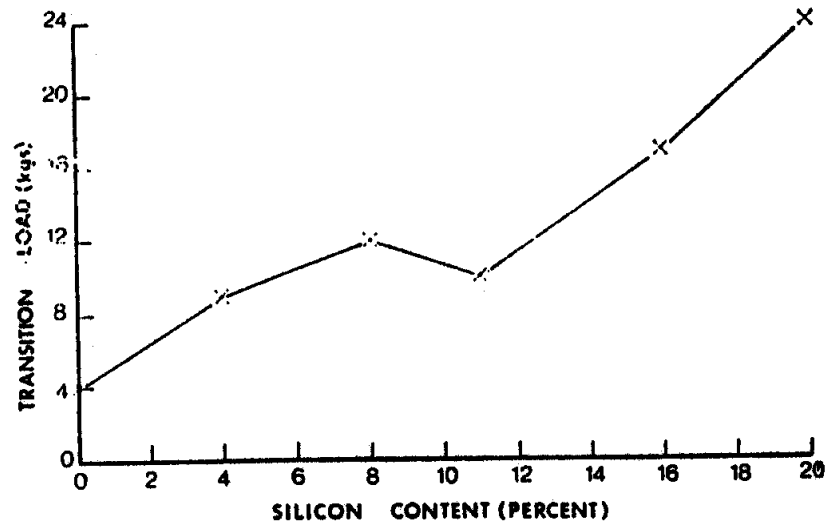


Fig. 2.15 Variation of transition load with Si content [38].

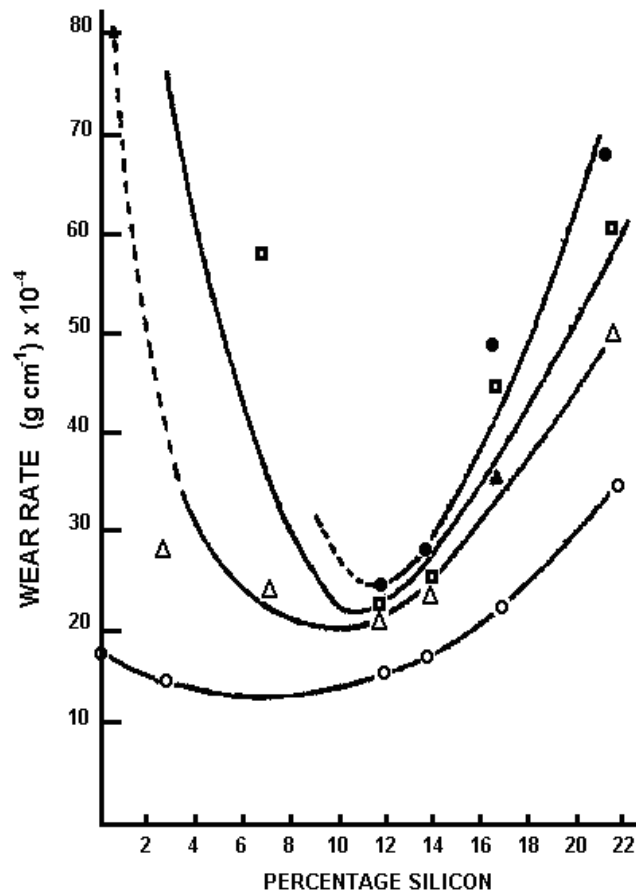
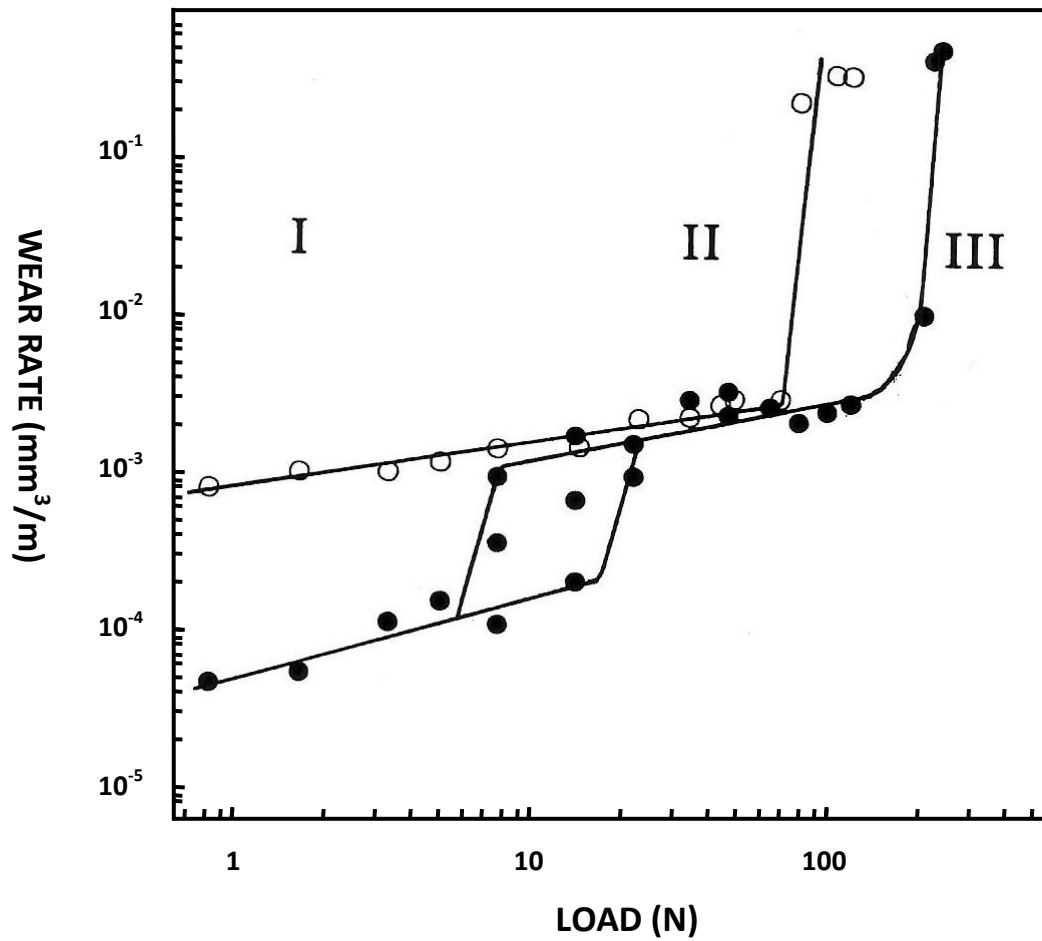
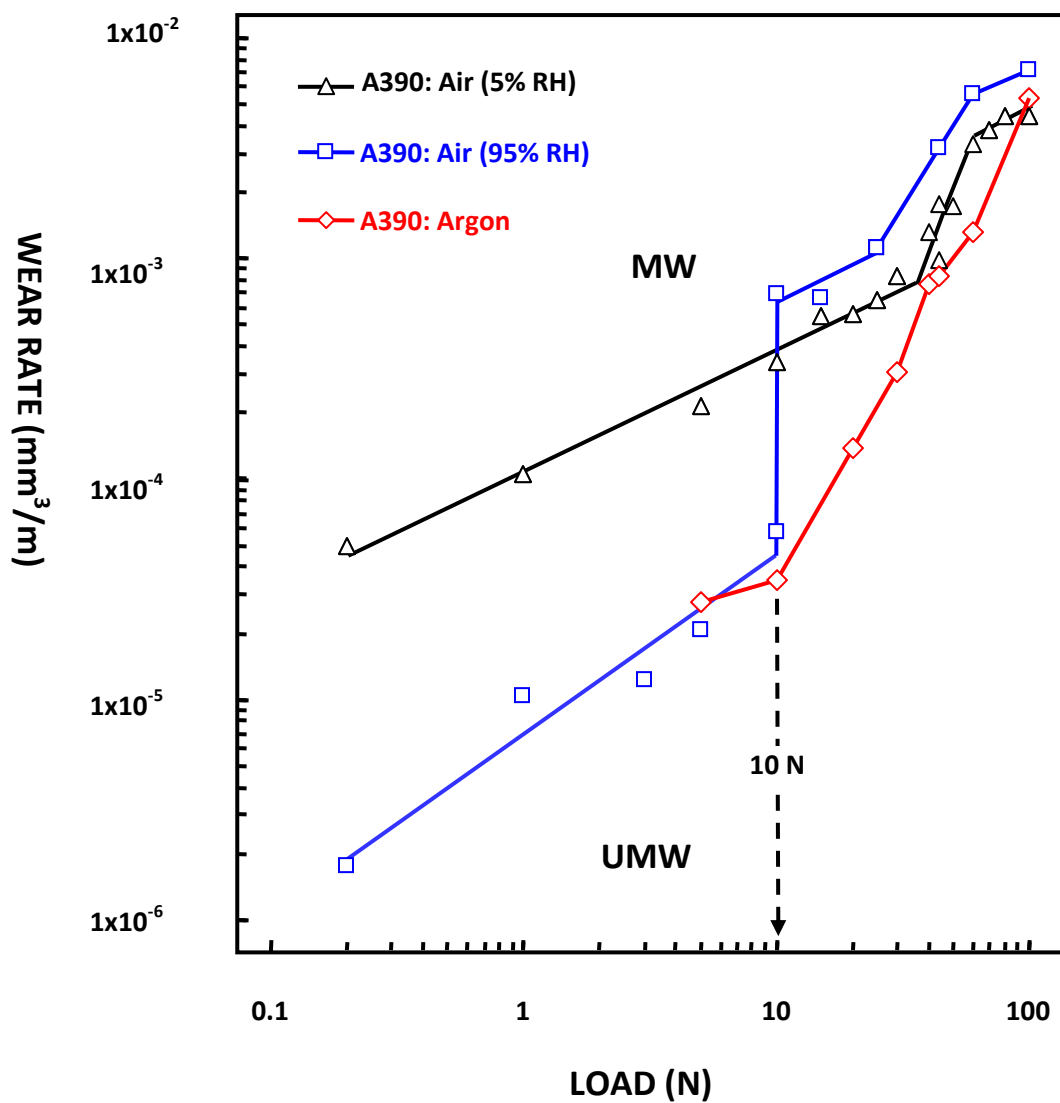


Fig. 2.16 Variation of wear rates of aluminum alloys sliding against a hard steel bush at a speed of 1.96 m/sec (Loads: ○:1 kg, △:1.5 kg, □: 2kg, ●: 2.5 kg) by Clarke and Sarkar [63].



**Fig. 2.17** Wear regimes in a cast A356 Al (○) and A356-20% SiC (●) particles (Configuration: block on ring, Speed: 0.8 m/s, Atmosphere: ambient air) by Zhang [70].



**Fig. 2.18** Variation of the wear rates with the test load [40].

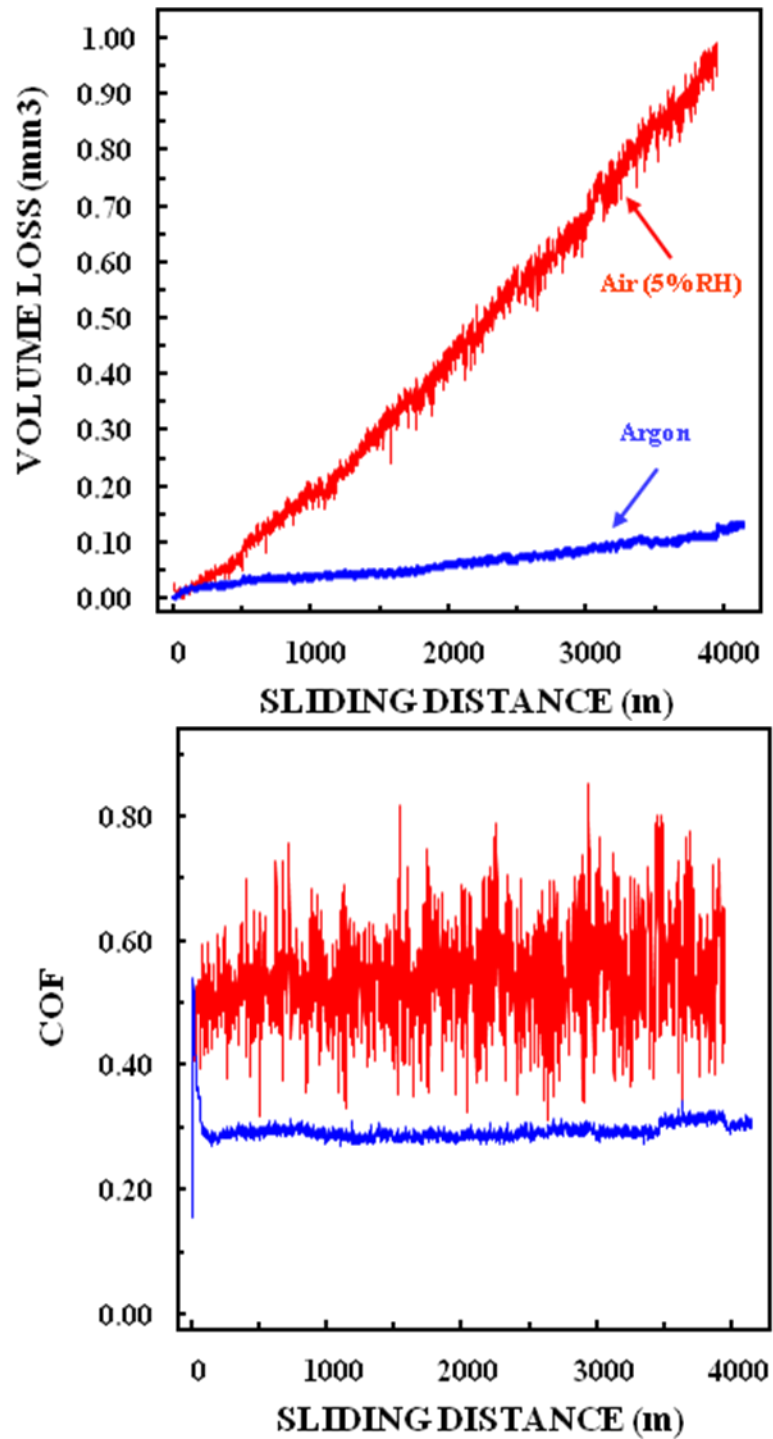


**Fig. 2.19** Comparisons of: (a) the volumetric wear and (b) the COF curves of A390 in air and argon atmospheres at a load of 10 N [46].

## **CHAPTER 3**

### **EXPERIMENTAL DETAILS**

This chapter describes the materials tested and the research methods used. First, the engine tests and materials for tests are described. Then, the experimental methods used for these tests, as well as for the metallographic investigations included the scanning electron microscopy (SEM) with energy dispersive spectroscopy (EDS), optical microscopy (OM), and optical surface profilometry (Wyko)—all of which are described in this chapter.

#### **3.1 Engine Tests and Materials for Tests**

Tribological analyses of the two linerless engine bores made from eutectic Al-Si alloys were conducted after the engine tests. One of the engines tested was made of a sand-cast Al-Si alloy. The engine bores were chemically etched before the engine was subjected to the dynamometer test. A dynamometer is a device used to measure the horsepower output of an engine while simulating actual driving conditions [72]. It can measure the parameters that characterize steady-state, full-throttle operation such as torque, power, fuel consumption, and exhaust smoke opacity at different speeds. In this case, the dynamometer tests were performed on a 5.7-liter V8 GM engine at the GM Powertrain Center in Michigan. The other GM engine inspected was made of Al-Si HF-V6 engine with brass-chilled bores. This engine was subjected to hot scuffing test at 150 °C. The wear patterns on the cylinder bores after the engine tests became the subject of further tribological failure analysis. Then, one eutectic Al-Si alloy (11% Si) was chosen to conduct the wear tests under controlled loading and environmental conditions.

### 3.2 Dry Sliding Tests

Dry sliding wear tests were accomplished using a block-on-ring type tribometer (**Fig.3.1**). Tests were performed at different loads in a range of 0.2-180N while a constant sliding velocity of 1.0 m/s was maintained. The tribometer consisted of a horizontal rotating shaft that turned the counterface ring and a vertical loading arm. The counterface steel ring samples were mounted to the spindle at the end of the horizontal rotating shaft, which was rotated by a variable speed, high torque (1 HP) D.C. electric motor. The Al-Si samples were mounted using a sample holder attached underneath the vertical loading arm. During the wear tests, the sample was loaded against the rotating counterface ring. Dead weights were placed in a pan located on the upper end of the vertical loading arm. A torque sensor (Model 4103-01A, maximum torque capacity 11 Nm, sensitivity  $\pm 0.05$  N) mounted on the shaft measured the friction force during the wear tests. The friction force was continuously measured and recorded by a multifunctional data acquisition system (IOtech Inc., Personal DAQ 56) connected to a personal computer.

All the wear tests were performed under controlled atmospheres. The tribometer was enclosed in a plexiglass chamber (90 x 50 x 40 cm) equipped with a humidifier (Electro-Tech Systems, model 562) and a dehumidifier (Electro-Tech Systems, model 561). The humidifier and dehumidifier were controlled by an electronic humidity controller made by Electro-Tech Systems (model 525). A 10 cm diameter circular fan was also set up to circulate the atmosphere inside the chamber.

The experiments were performed at constant humidity levels of  $5\pm 2\%$  RH, both in air and argon atmosphere. The experiments in an argon (99.999% purity) atmosphere were performed to study the wear mechanism in a non-oxidizing environment. To control



the argon atmosphere around the samples and minimize gas usage, a smaller plexiglass chamber (20 cm x 20 cm x 10 cm) was placed around the sample and counterface assembly. Before each test, the chamber was flushed with compressed argon gas and then a continuous flow of argon gas was directly blown to the block sample at an exit pressure of 2 Psi during the testing.

### **3.3 Sample Preparations for Wear Tests**

Al-Si samples were machined from the as-received materials in the form of rectangular blocks with 10 mm x 10 mm x 5 mm dimensions. They were finished with 600-grit SiC abrasive paper prior to the wear tests. The average roughness ( $R_a$ ) of the sample surface was  $0.21 \pm 0.05 \mu\text{m}$ , and then the samples were cleaned ultrasonically by immersing them in acetone before and after each wear test.

The counterface ring was made of SAE (AISI) 52100-type bearing steel, with the following alloy composition (wt %): 0.98 to 1.1 % C, 0.25 to 0.45 % Mn, 0.15 to 0.30 % Si, and 1.30 to 1.60 % Cr. It had an outer diameter of 38 mm and width of 12 mm respectively. The counterface hardness was measured as a 61 on the Rockwell-C scale. Like Al-Si alloy samples, the counterface ring surface was finished with 600-grit SiC abrasive grinding paper and cleaned ultrasonically by immersion in acetone before each test. The sample's narrow face (5mm×10mm) was put in contact with the counterface ring surface.

### **3.4 Wear Rate Measurement**

Dry sliding wear tests were conducted within a load range of 0.2 to 180 N at a constant speed of 1 m/s, with a constant sliding distance of  $4 \times 10^3$  m. If excessive wear

and surface damage (severe wear conditions) occurred, the tests were stopped before  $4 \times 10^3$  m. An analytical balance with an accuracy of 0.1 mg was used to measure the mass of the samples before and after each test. At each test load, the wear in mass loss (M) was then converted to volume loss (V) using the density ( $\rho$ ) of the material. The density of the alloy was measured using a liquid immersion technique based on the Archimedes principle. Finally, the volumetric wear rate (W) was calculated from the slopes of the volumetric loss (V) vs. sliding distance (S) curves. The following equations show the methods of calculating the volume loss and the wear rate:

$$V = \frac{M}{\rho} \quad (3.1)$$

$$W = \frac{V}{S} \quad (3.2)$$

### 3.5 Sample Preparation for Metallographic Analysis

Samples that were parallel and normal to sliding directions were cut from the representative regions of the cylinder bore. To avoid cold working and altering the microstructure, they were cut with a low speed saw (Buehler ISOMET) and cooled by a liquid coolant (Varsol dilute solution) during cutting. The sample preparation procedures included sectioning, mounting, grinding, polishing, and etching. After being mounted with a fast curing epoxy resin mixed with a hardener, the samples were wet grinded with abrasive rotating disks and sand papers with grit sizes from 240 to 4000, then polished with diamond paste until a mirror-like surface finish was obtained. The samples were then etched by an acetic glycol etchant for 10 to 50 seconds after they were cleaned with water and dried with acetone. [73].

### 3.6 Evaluation of Worn Surface and Subsurface Morphologies

Microstructural examinations and microhardness measurements of the worn surfaces and the cross-sectional subsurface were used to determine the wear micromechanisms. The elemental compositions and morphologies of the worn surfaces and the cross sections located below the worn surfaces were characterized by scanning electron microscopy (5800 LV SEM) equipped with an energy dispersive spectroscope (EDS). An optical microscope (OM) was also used (Axiovert). A non-contact optical profilometer (WYKO, NT 1100 System) was utilized to characterize the worn surfaces' topography. This is a non-contact, three-dimensional profilometer, used to detect the surface roughness. Ra, (roughness average) is the average vertical deviation from a line drawn centrally through the profile, and serves as a good general indication of smoothness. Rz is the peak-to-peak height obtained by averaging the five highest peaks and the five deepest valleys in the measured profile.

Microhardness testing was conducted using a Vickers diamond indenter with a constant load of 10g. A microhardness tester, Buehler Micromet II® (Model 1600-9000) - with a square-base diamond pyramid indenter (136 ° tip angle)--was used to measure the hardness of the aluminum matrix. The indentation load applied was 10 g. A Brinell hardness tester was used to measure the bulk hardness of the alloys with a 10 mm diameter steel ball and at a load of 500 kg. The values reported were the averages of at least 10 measurements.

For precise microhardness measurements of the subsurface sections, samples sectioned at an angle of about 5.7° to the sliding direction were used (**Fig. 3.2**). The tapered sections provided a 10 times magnification of the subsurface zones, compared to

the normal cross-sections found below the worn surfaces. The tapered sections were prepared with metal stands cut at a 5.7° angle. The Al-Si samples were placed on top of the metal stands, and then mounted. The polishing of the mounted sample was performed from the top.

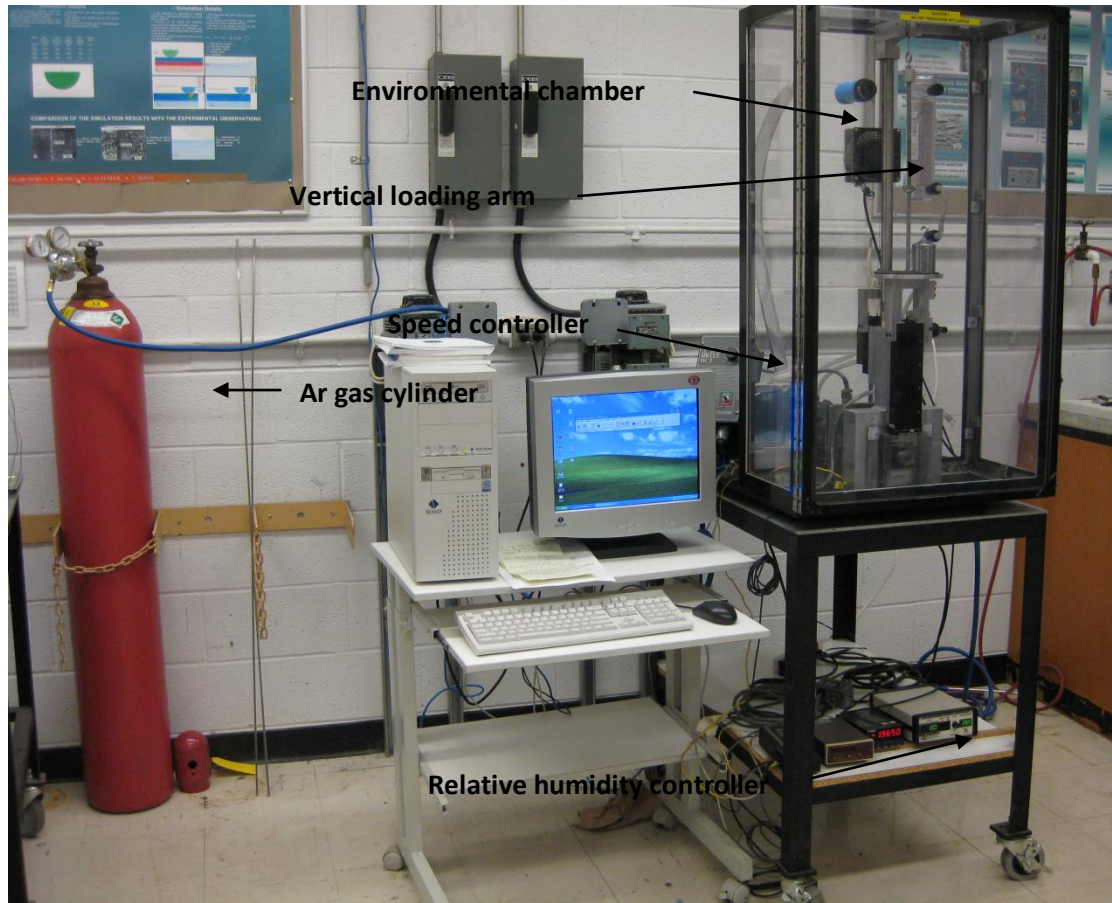
### 3.7 Measurement of Si Aspect Ratio and Secondary DAS

The size distributions for the Si particles were determined by quantitative metallography using a digital image analyzer. The particle length was determined by measuring the maximum length of each particle and the particle width was determined by measuring the widest distance across each particle in a direction perpendicular to the direction of the maximum length. The aspect ratio was defined as the average particle length divided by average particle width. About 250 silicon particles were used in these measurements, and the results were summarized in the form of a histogram showing the distribution of silicon particle length and width size.

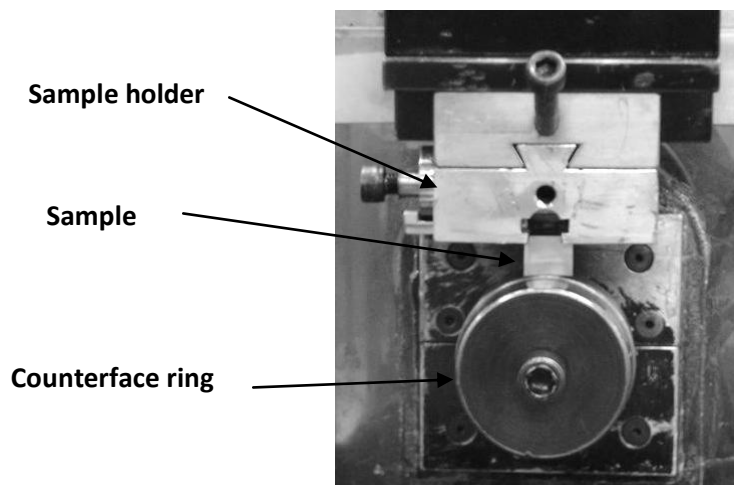
The samples of secondary dendrite arm spacing (DAS) were sectioned from the unworn areas of each engine block. The DAS of the alloys were measured using the following equation:

$$DAS_n = \frac{L}{n_n} \quad (3.3)$$

Where  $L$  is the length of the measured line, and  $n_n$  is the number of arms intersected by a measured line (**Fig. 4.4**). 40 - 60 dendrite lines were measured for both sand-cast and brass-chilled alloys. The histograms in **Fig. 4.5** show the DAS distributions in each alloy. The DAS of the sand-cast alloy was  $55.6 \pm 15.9 \mu\text{m}$ , while the brass-chilled alloy had a DAS of  $22.8 \pm 3.9 \mu\text{m}$ .



(a)



(b)

**Fig. 3.1** (a) A photograph showing the general view of the block on ring tribometer (b) An enlarged view of sample holder with an Al-Si block sample, and spindle carrying a counterface ring.

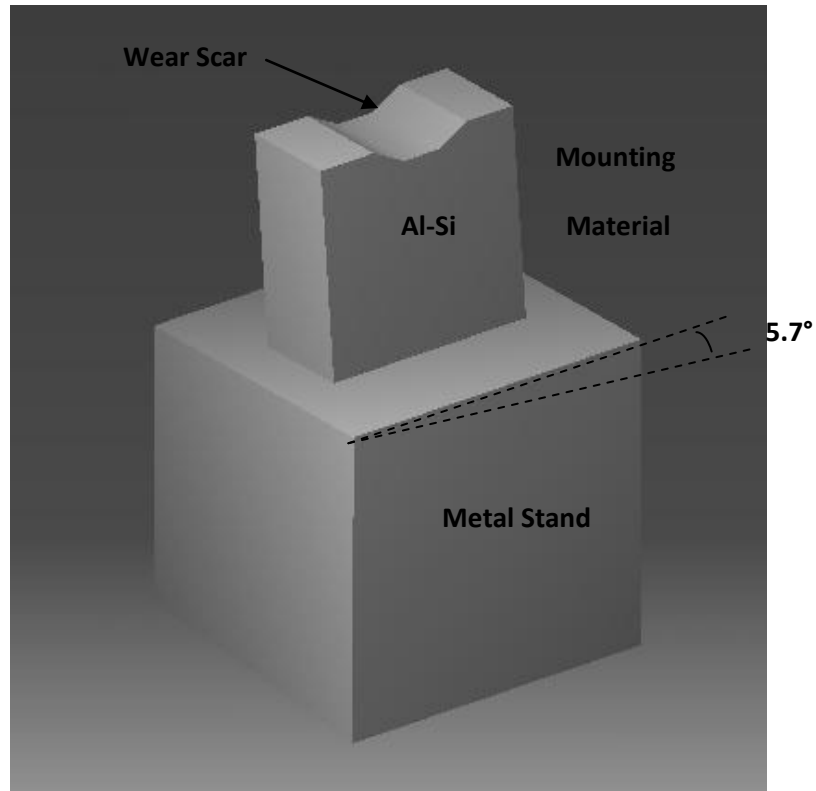


**Fig. 3.2** Three dimensional schematics showing the preparation of the taped sections. Metal stand cut at an angle of 5.7°.

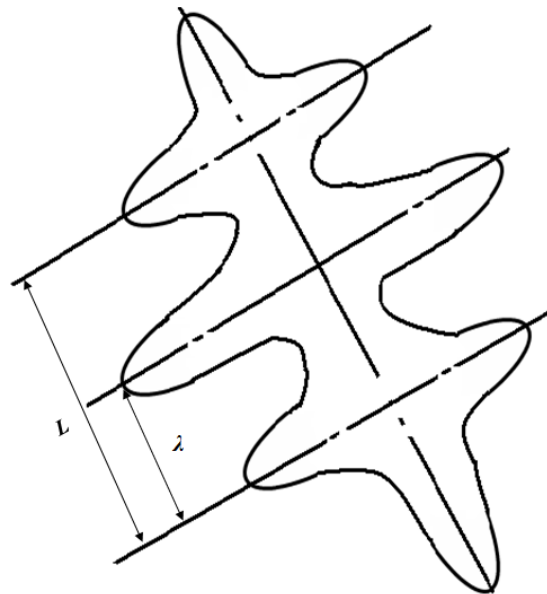


**Fig.3.3.** Measurement method of secondary dendrite arm spacing:  $\lambda(DAS) = \frac{L}{n}$ .

## **CHAPTER 4**

### **MICROSTRUCTURES, PROPERTIES AND WEAR OF LINERLESS**

#### **Al-Si ENGINES: SAND-CAST AND BRASS-CHILLED ALLOYS**

To understand the details of the microstructural processes involved in engine wear and scuffing, it is important to characterize the surface and subsurface damage in the actual Al-Si alloy engines currently in development. A tribological analysis of the failure mechanisms and wear mechanisms of Al-Si alloy bores was conducted to investigate the sliding damage processes in linerless cylinder bores made of eutectic aluminum silicon alloys. The purpose of these investigations was to understand how wear occurred to aluminum cylinder bores with different microstructures on a microscopic scale. The metallographic analyses were conducted using light optical microscopy (OM), optical surface profilometry (OSP), and scanning electron microscopy (SEM) with energy dispersive spectroscopy (EDS).

#### **4.1 Al-Si Alloy Engines Tested**

One of the linerless engines (a 5.7-liter V8 engine) tested was made of a sand-cast, near-eutectic aluminum alloy. The engine bores were chemically etched before the engine was subjected to the dynamometer engine tests, which were performed at the GM Powertrain Center. The engine endured an aggressive, 33-Hour test broken into three 11-hour segments, with the first at 1,000 rpm, the second at full power, and the third at half power. The bores were inspected after each 11-hour segment, and it was the cylinder bores that became the subject of tribological failure analysis in this work (Shown in **Fig. 4.1**).

The other linerless GM engine inspected was an Al-Si HF-V6 engine. The bores of this engine were brass-chilled during casting. The HF-V6 engine was subjected to hot scuffing tests at 150 ° C, but the engine was sound and did not show any indication of scuffing (seen in **Fig. 4.2**). Two distinct areas- an unworn region and a normal wear area (worn area) –were identified.

## **4.2 Chemical Composition and Hardness of Al-Si Alloys**

Chemical compositions for the Al-Si alloys were determined and recorded in **Table 4.1**. Both alloys are classified as near-eutectic Al-Si alloy, and the wt% of other elements beyond Cu (Mg, Fe, Mn, and Sr) were not much different. The sand-cast Al-Si alloy contained more Cu (2.3%) than the brass-chilled Al-Si alloy (0.87%). It also contained 1.0% Ni. The Ti percentage was two times higher in the brass-chilled alloy than in the sand-cast alloy. Two samples were sectioned from the unworn areas of each engine block, namely sand-cast and brass-chilled Al-Si HF-V6 engines. Their hardnesses were measured, and the values shown in **Table 4.2** are the averages of at least 10 measurements. The bulk hardness of the sand-cast engine Al-Si alloy was  $153 \pm 0.72$  HB. The brass-chilled engine Al-Si alloy had a hardness of  $162 \pm 1.06$  HB. The microhardness of the sand-cast's matrix alloy was measured as  $74.5 \pm 7.94$  HV<sub>10</sub> (Vickers hardness at 10 g load), while the matrix hardness of the brass-chilled alloy was  $77.9 \pm 11.07$  HV<sub>10</sub>.

## **4.3 Alloys Microstructures**

Metallographic analyses were conducted using an optical microscope (Olympus BH2), and a SEM (JEOL5400) with EDS. Samples chosen for metallographic examination were extracted from the representative regions of the cylinder bore. The



samples were carefully sectioned using a belt saw and coolant to prevent altering the microstructure. They were then, mounted, ground, and polished using the steps mentioned in Chapter 3. Finally, the samples were etched in a solution of 84 ml H<sub>2</sub>O, 15 ml HNO<sub>3</sub>, 0.5 ml HF and 3g CrO<sub>3</sub>.

#### **4.3.1 Dendrite Arm Spacing (DAS) of the Two Alloys**

Two samples were sectioned from the unworn areas of each engine block, and their optical microstructures were observed and compared. **Fig. 4.3 (a) and (b)** show that the two alloys have different dendrite arm spacing (DAS). 40 - 60 dendrite lines were measured for both sand-cast and brass-chilled alloys. The histograms in **Fig. 4.4** show the DAS distributions in each alloy. The DAS of the sand-cast alloy was  $55.6 \pm 15.9 \mu\text{m}$ , while the brass-chilled alloy had a DAS of  $22.8 \pm 3.9 \mu\text{m}$ .

#### **4.3.2 Identification of Phases in the Alloys**

Optical micrographs of the polished, unworn areas in **Figs. 4.5 (a) and (b)** show the alloy's silicon phase morphologies. SEM and EDS were used to identify the phases in the alloys. **Figs. 4.6 (a) and (b)** presented the SEM images of the microstructures. EDS analyses were performed on each of those phases to identify the main compositions. The alloys were composed of two main phases: the  $\alpha$ -Al matrix, and the Si particles. The phase with Chinese script morphology was Al<sub>15</sub>(Fe, Mn)<sub>3</sub>Si<sub>2</sub>, while the grey, needle-like phase was Al<sub>5</sub>Mg<sub>8</sub>Cu<sub>2</sub>Si<sub>6</sub>. Unlike sand-cast alloy, however, no light grey particles of CuAl<sub>2</sub> were found in the brass-chilled alloy because of low Cu content.

### **4.3.3 Si Morphology and Size**

To reveal the three-dimensional shape of Si, the samples were immersed into a solution of 10 ml HCl and 90 ml distilled H<sub>2</sub>O for 24 hours, followed by 1 hour in a solution of 2.5 ml HCl, 2 ml HNO<sub>3</sub>, 0.75 ml HF and 40 ml distilled H<sub>2</sub>O to dissolve the Al matrix and reveal the Si. The SEM micrographs in **Figs. 4.7 (a) and (b)** clearly display the sand-cast Al-Si alloy's large, plate-like silicon particles and the brass-chilled alloy's smaller, more spherical Si particles (**Figs. 4.8 a-b**).

The length and width of Si particles were measured using an image processing analysis. The histograms in **Figs. 4.9 and 4.10** show Si particle size distributions in each alloy. The average Si particle length and width in the sand-cast Al-Si alloy were  $40.4 \pm 20.6 \mu\text{m}$  and  $4.8 \pm 2.5 \mu\text{m}$ , resulting in an aspect ratio (average length to average width) of 8.4. The Si particle's average length in the brass-chilled alloy was  $5.2 \pm 3.4 \mu\text{m}$ , and the Si width was  $5.1 \pm 3.5 \mu\text{m}$ --producing an aspect ratio of 1.1, which meant that the aspect ratio of the sand-cast alloy was more than 8 times higher than that of the brass-chilled alloy.

### **4.3.4 Surface Morphology**

An optical surface profilometer (WYKO NT 1100 System) was used to characterize surface morphology. The vertical-scanning interferometry (VSI) mode was used to measure the surface roughness.

**Fig.4.11** shows the surface profiles of the alloys taken from the unworn surfaces. 200 Si particles in the sand-cast alloy, and 218 Si particles in the brass-chilled alloy projected above the aluminum matrix were used to measure Si particle height. The Si particle height was determined from the height difference of Si protruding above the

matrix. The average Si height in the sand-cast alloy was  $0.46 \pm 0.13 \mu\text{m}$ , and  $0.54 \pm 0.19 \mu\text{m}$  in the brass-chilled alloy. The histograms in **Figs. 4.12 (a) and (b)** show Si height distributions across an area of  $1.39 \times 1.83 \text{ mm}^2$ .

## **4.4 Analysis of the Normal Wear Area**

### **4.4.1 Sand-Cast Alloy**

The secondary SEM micrograph presented in **Fig.4.13 (a)** shows that the normal wear area has a much duller appearance than the normal wear area, as illustrated in **Fig.4.13 (b)**. Back-scattered SEM and EDS micrographs of the sand-cast engine's normal wear surface given in **Fig. 4.14** show that besides elements contained in the Al-Si alloy, other elements existed on the surface--including C, O, Zn, P, S, and Ca. It can be inferred that these elements originated from the engine oil.

The cross-sectional view shows that a layer about  $1 \mu\text{m}$  in thickness (**Fig. 4.15**) formed on the normal wear surfaces. This is the oil residue layer mixed with Al and Si. **Figs. 4.16 (a) and (b)** illustrate the 3-D surface profile of the sand-cast engine's normal wear area at low and high magnifications. Its average roughness was  $895\text{nm}$ , and there were particles delaminated from the worn surface (**Fig.4.17**) corresponding to depressions of  $1\mu\text{m}$  depth (Fig.4.17). The Cross-sectional optical and SEM micrographs in **Fig. 4.18** show Si fractures on the normal wear surfaces.

### **4.4.2 Brass-chilled Alloy**

**Figs. 4.19 (a) and (b)** reveal that there was also a layer of about  $1\mu\text{m}$  thick that was formed on the brass-chilled engine's normal wear surface. According to **Fig. 4.19 (c)**, the layer contained the elements O, Zn, Ca, and C-identifying it as a mixture of engine oil, aluminium, and silicon. The surface morphology of the brass-chilled engine is illustrated

in **Fig. 4.20**. Its average roughness  $R_a$  is 197.9 nm (average of an area of  $3.1 \times 4.2 \text{ mm}^2$ ) and lower than that of the sand-cast engine (895nm). A secondary SEM image of the brass-chilled engine shown in **Fig.4.21** reveals that delamination occurred at the worn surface. The roughness of these two alloys in unworn and normal wear areas appears in **Table 4.2**. There were fractured Si particles on the normal wear surfaces (**Fig. 4.22**) of the brass-chilled alloy.

## 4.5 Discussion

**Fig. 4.15 and 19** revealed the formation of a  $1 \text{ }\mu\text{m}$  layer--a mixture of engine oil and Al, Si-- on the surface of the normal wear areas of both engine cylinder bores. The normal wear area observed on the brass-chilled Al-Si engine surface was much smoother than that on the sand-cast engine. Also, fewer particles were removed from the normal wear surface of the brass-chilled engine compared to the sand-cast engine (**Figs 4.16 and 20**)—suggesting that the brass-chilled Al-Si alloy engine had better wear performance than the sand-cast alloy engine.

Copper can improve Al-Si alloys' strength by promoting precipitation hardening, and the sand-cast Al-Si alloy contained a larger amount of Cu (2.3 wt%) than the brass-chilled Al-Si alloy (0.87 wt%). The DAS of the brass chilled alloy was more than 2 times smaller than that of the sand-cast alloy, and the brass-chilled Al-Si alloy had a finer microstructure and smaller DAS due to faster cooling (**Figs. 4.3 and 4.4**). A decrease in the grain size and DAS can improve the alloy strength, so even though these two alloys had different chemical compositions and microstructures, they attained similar bulk hardness (shown in **Tables 4.1 and 4.2**).

A previous study [15] indicates that the wear rate decreases along with a decrease in the Al's grain size and DAS of Al. The Si particle morphology and size also have significant influence on wear performance. Si particles displayed a mostly plate-like morphology in the sand cast alloy (**Fig. 4.7**), and were spherical in the brass-chilled alloy (**Fig. 4.8**). As previously indicated, the aspect ratio of the length to the width of Si particles in the sand-cast alloy is about 8 times larger than that of the brass-chilled alloy (**Figs. 4.9** and **10**). Decreasing the silicon particle size and aspect ratio can reduce the wear coefficient and increase the transition loads [12], which suggests that the presence of spheroidized Si particles with low aspect ratios in the brass-chilled Al-Si should improve wear resistance.

## 4.6 Summary

The microstructures and wear performance of these two engine bore surfaces are summarized in **Table 4.4**. We found that the average roughness of the mechanically prepared surface (brass chilled alloy) was higher than the one that was chemically etched (sand-cast alloy) and the Si height average for the brass-chilled unworn surface was lower than the one for the sand-cast engine (**Fig.4.12**). The normal wear surfaces in both engines were covered by a 1  $\mu\text{m}$  thick layer of a mixture of engine oil and Al, Si. The brass-chilled Al-Si alloy engine, which had a finer microstructure and more spheroidized Si particles with a lower aspect ratio than the sand-cast Al-Si alloy, displayed better wear performance than the sand-cast engine. The brass-chilled Al-Si alloy engine bore also had a much smoother normal wear area, on which less fracture occurred.

**Table 4.1** Chemical compositions (in wt%) of the Al-Si alloys studied

Alloys	Si	Cu	Mg	Fe	Mn	Sr	Ti	Ni	Al
Sand-cast	11.0	2.3	0.3	0.5	0.6	0.022	0.05	-	The Balance
Brass-chilled	12.6	0.87	0.27	0.37	0.79	0.02	0.11	1.0	the Balance

**Table 4.2** Hardnesses of the alloys studied

Alloy	Hardness (HB)	Matrix Microhardness (HV)
Sand-cast	153±0.72	74.5±7.94
Brass-chilled	162±1.06	77.9±11.07

**Table 4.3** Roughness of these two alloys studied (Area covered: 1393x1831 mm<sup>2</sup>)

Alloy	Ra (Unworn Area)	Rt (Unworn Area)	Ra (Normal wear area)
Sand-cast	74.7nm	1.58µm	895nm
Brass-chilled	80.17nm	1.26µm	197.9nm

**Table 4.4** Summary of the Microstructures and Wear Performance for Two Eutectic Al-Si Alloy Engines

Alloy	Microstructure					Unworn surface		Normal Wear		
	DAS ( $\mu\text{m}$ )	Si shape	Si size ( $\mu\text{m}$ )		Aspect ratio	Ra (average)	Si height distribution ( $\mu\text{m}$ )	Ra (average)	Si fractures	Delamination
			Length	Width						
<b>Sand-cast</b>	55.59	Large plate-like	40.39	4.78	8.44	74.7 nm	0.54	895 nm	Yes	Yes
<b>Brass-chilled</b>	22.8	Small spherical	5.24	5.08	1.05	80.17 nm	0.46	197.8 nm	Yes	Yes

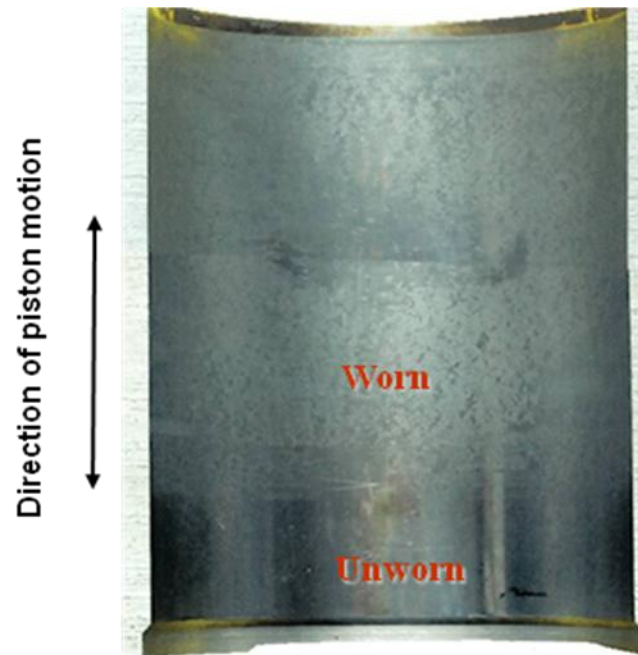


**Fig. 4.1** Sand-cast Al-Si engine bore surface with the indications of different wear type after dynamometer engine test.

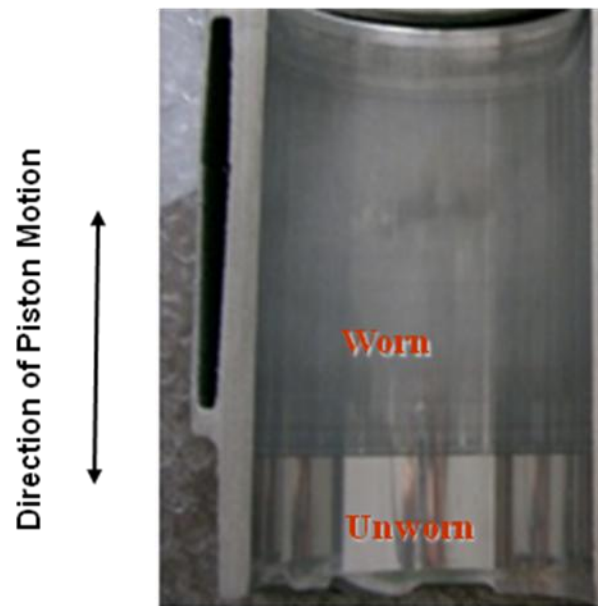
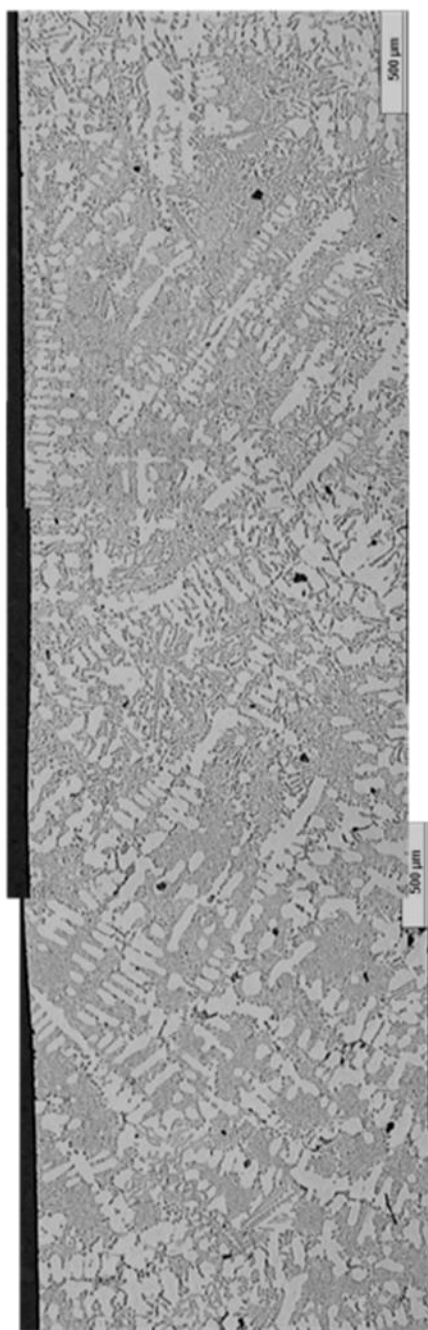
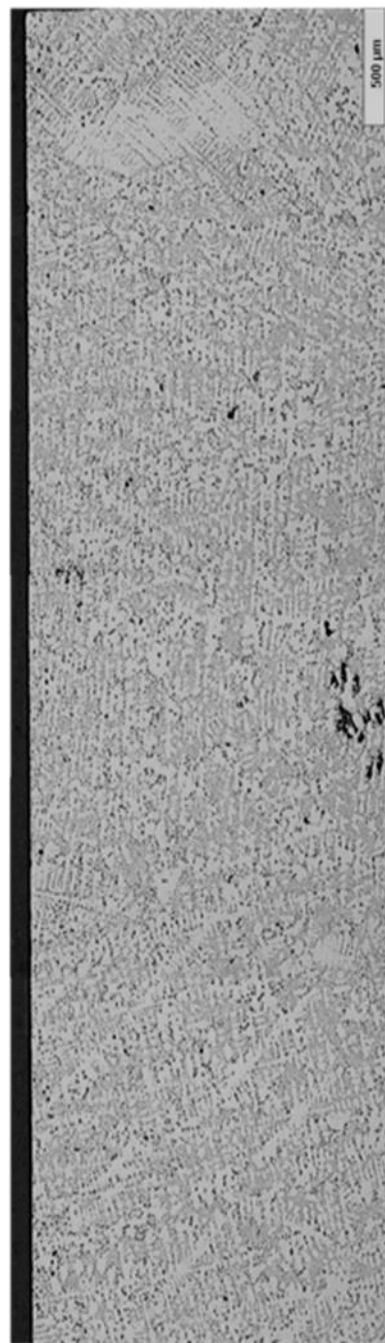


**Fig. 4.2.** Brass-chilled Al-Si engine bore surface after hot scuffing test at 150 °C.



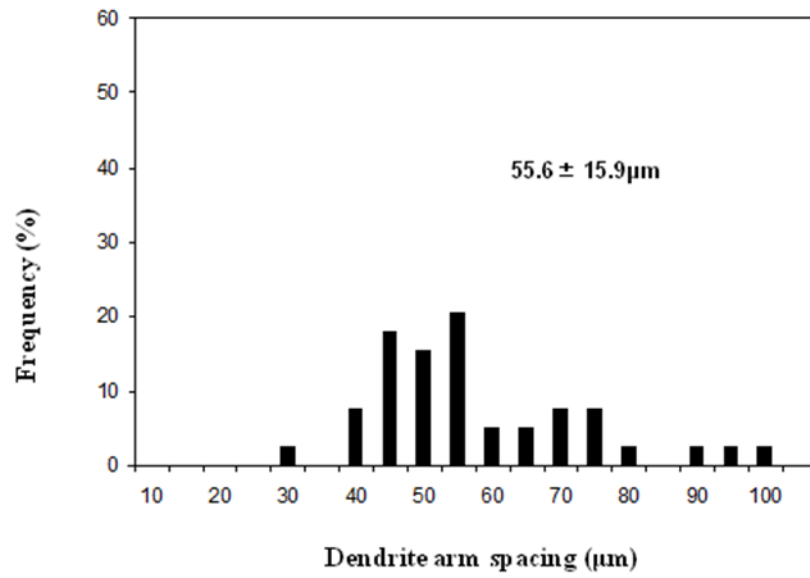


(a)

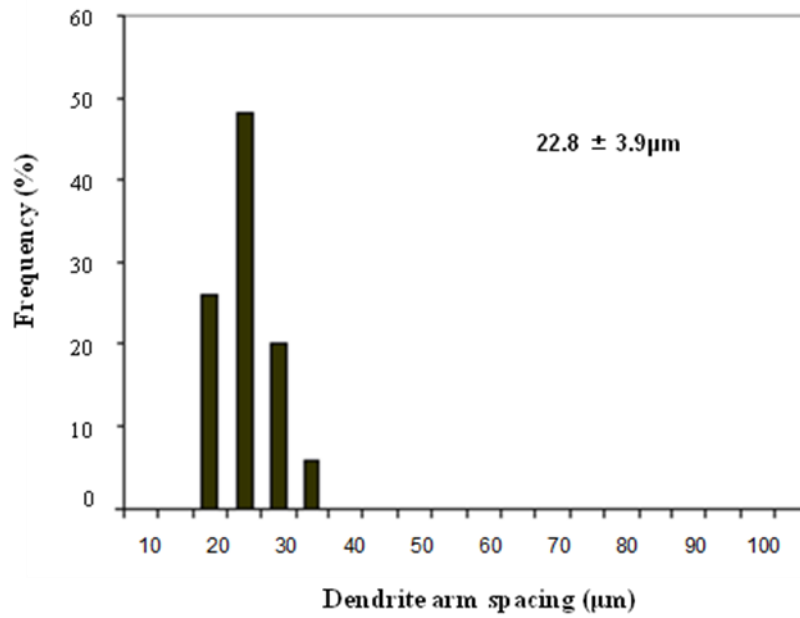


(b)

**Fig. 4.3.** Optical micrographs from unworn areas of two engines showing dendrites clearly. (a) Sand-cast alloy, (b) Brass-chilled alloy.

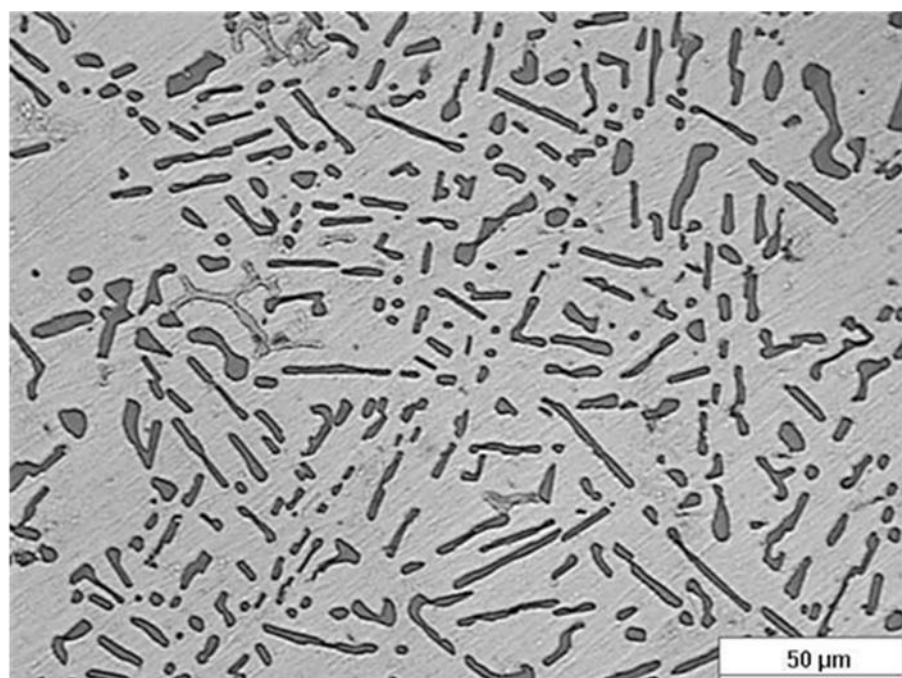


(a)

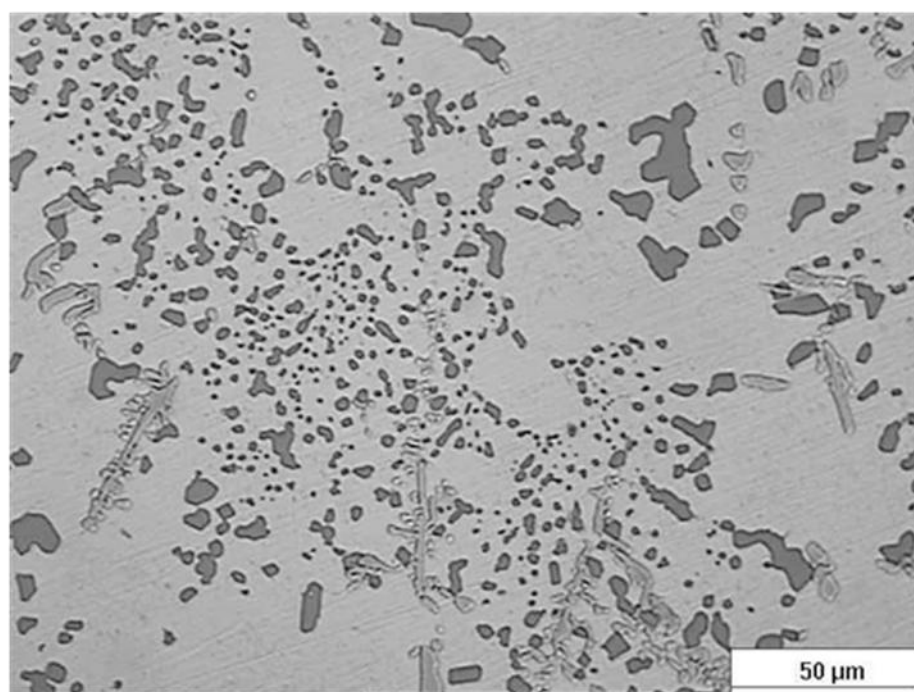


(b)

Fig.4.4. Histograms showing the dendrite arm spacing in (a) Sand-cast alloy, (b) Brass-chilled alloy.

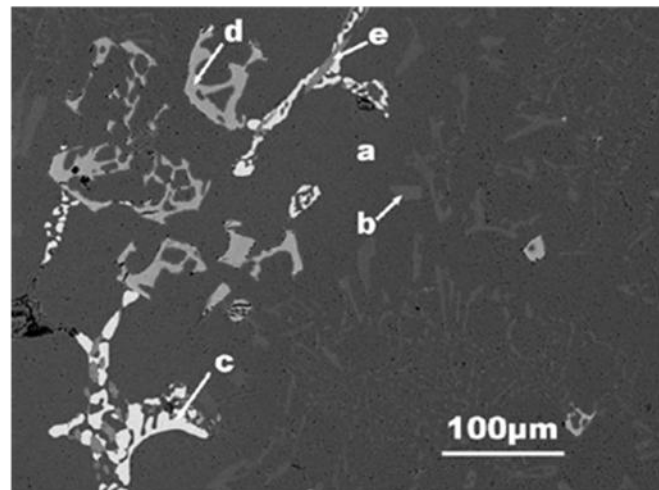


(a)

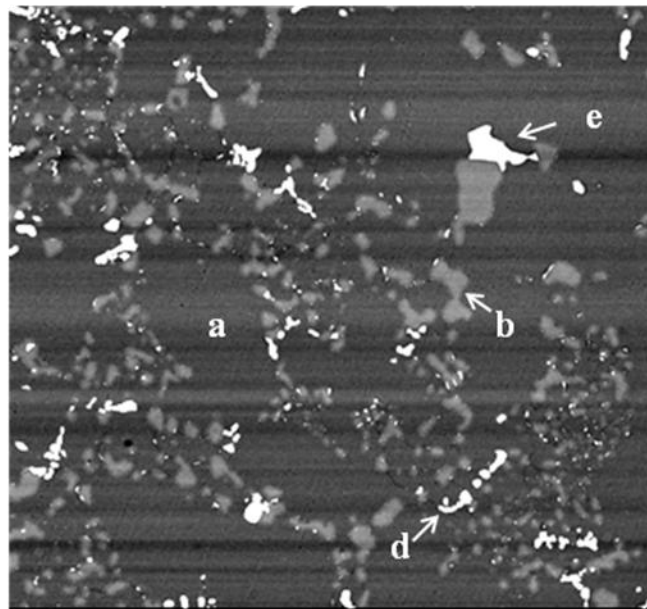


(b)

**Fig.4.5** Optical micrographs in unworn area of two alloys (a) Sand-cast (b) Brass chilled alloy

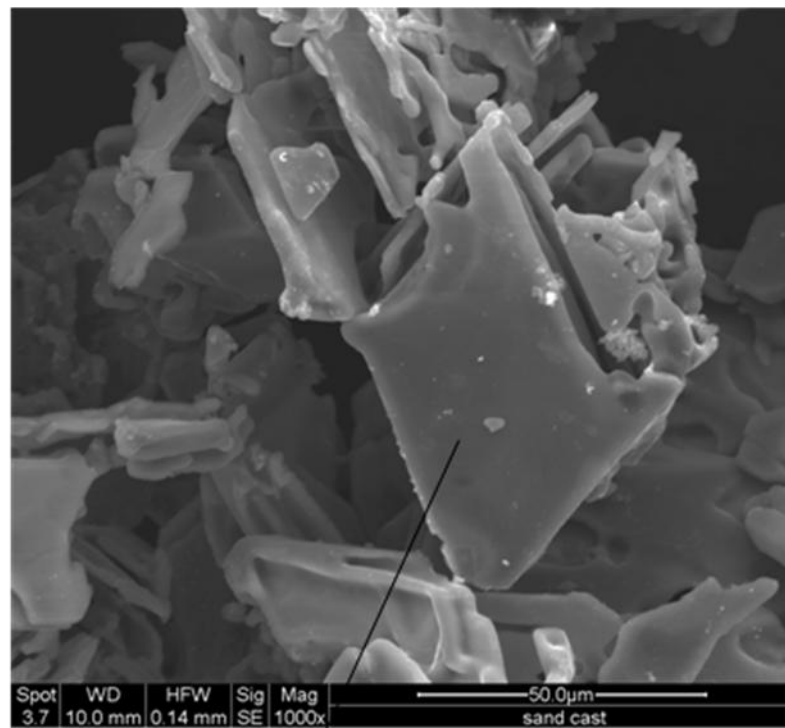


(a)

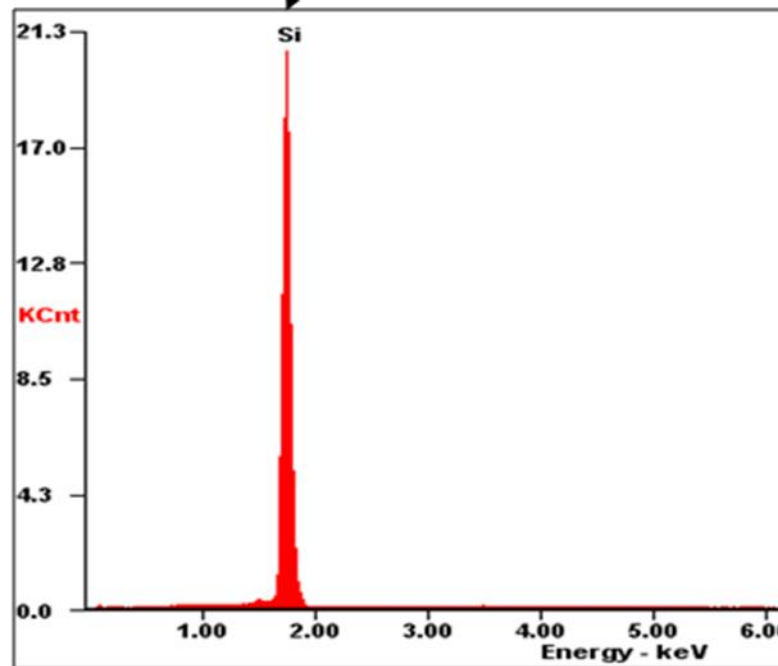


(b)

**Fig. 4.6** SEM secondary micrographs, (a) sand-cast Al-Si alloy, (b) brass-chilled, the phases identified using SEM/EDS and labeled as: a)  $\alpha$ -Al, Matrix; b) Si Phase; c) light gray particles  $\text{CuAl}_2$  phase; d) Chinese script phase  $\text{Al}_{15}(\text{Fe}, \text{Mn})_3\text{Si}_2$ , e)  $\text{Al}_5\text{Mg}_8\text{Cu}_2\text{Si}_6$ , gray needle-like.

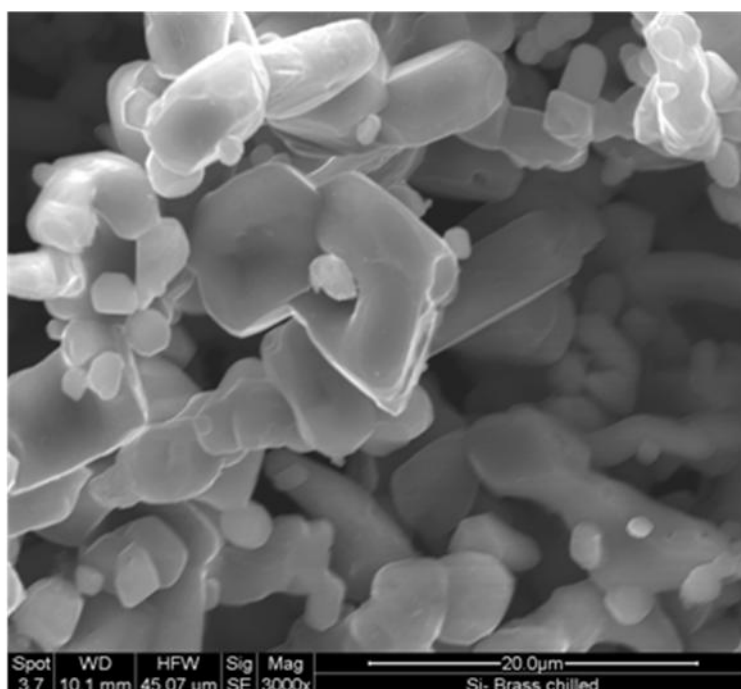


(a)

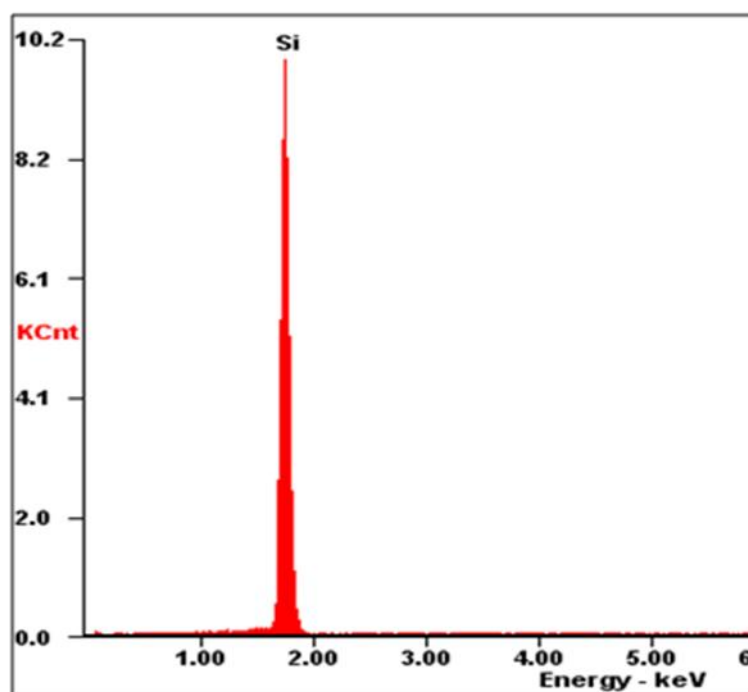


(b)

**Fig. 4.7** (a) A secondary SEM micrograph in sand-cast alloy showing plate-like Si morphology, (b) the EDS spectrum identify the Si particles.

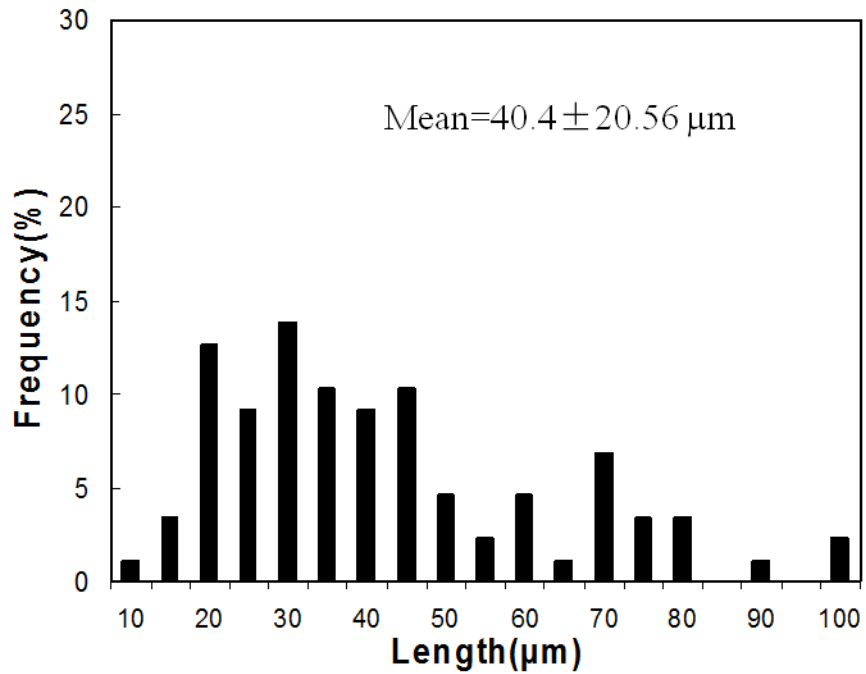


(a)

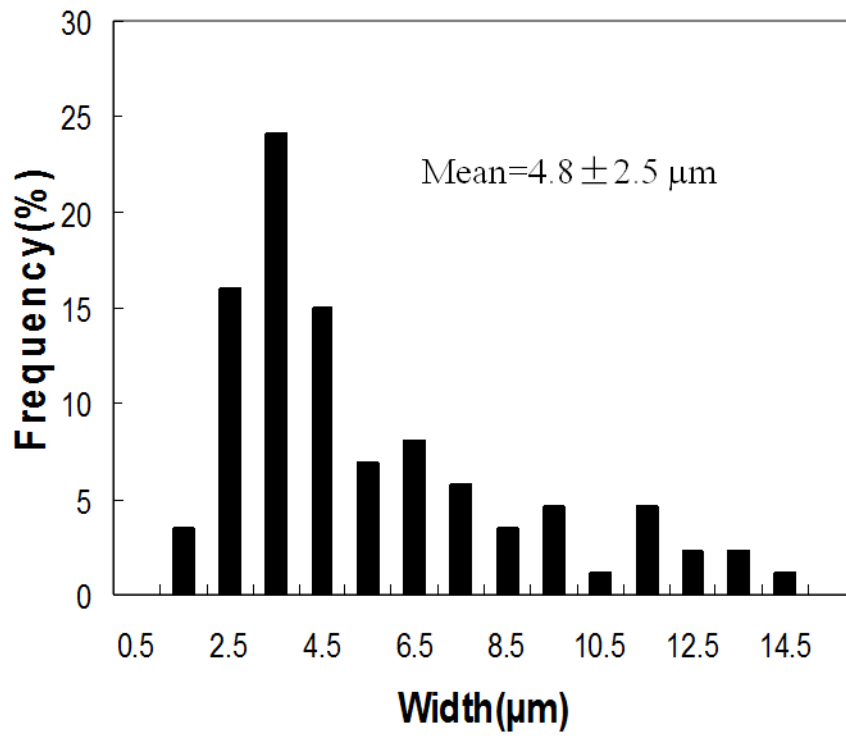


(b)

**Fig. 4.8.** (a) A secondary SEM micrograph showing that Si morphology in brass-chilled alloy is more spherical, (b) the EDS spectrum identify the Si particles.



(a)



(b)

**Fig. 4.9** Histograms showing Si particle length (a) and width (b) distribution in the sand-cast Al-Si alloy.

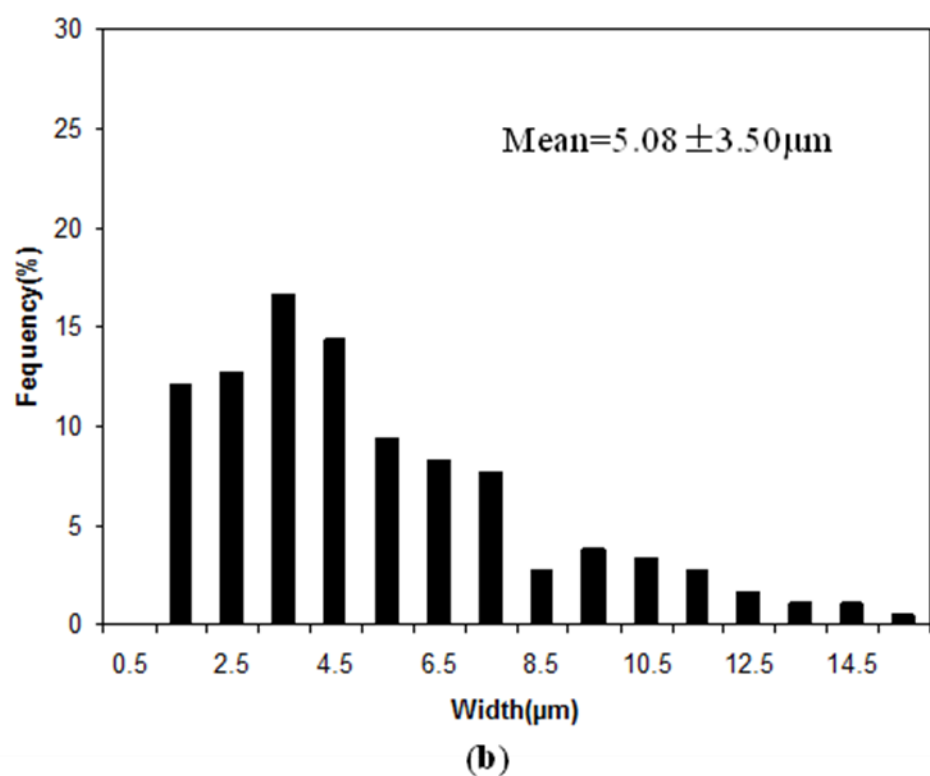
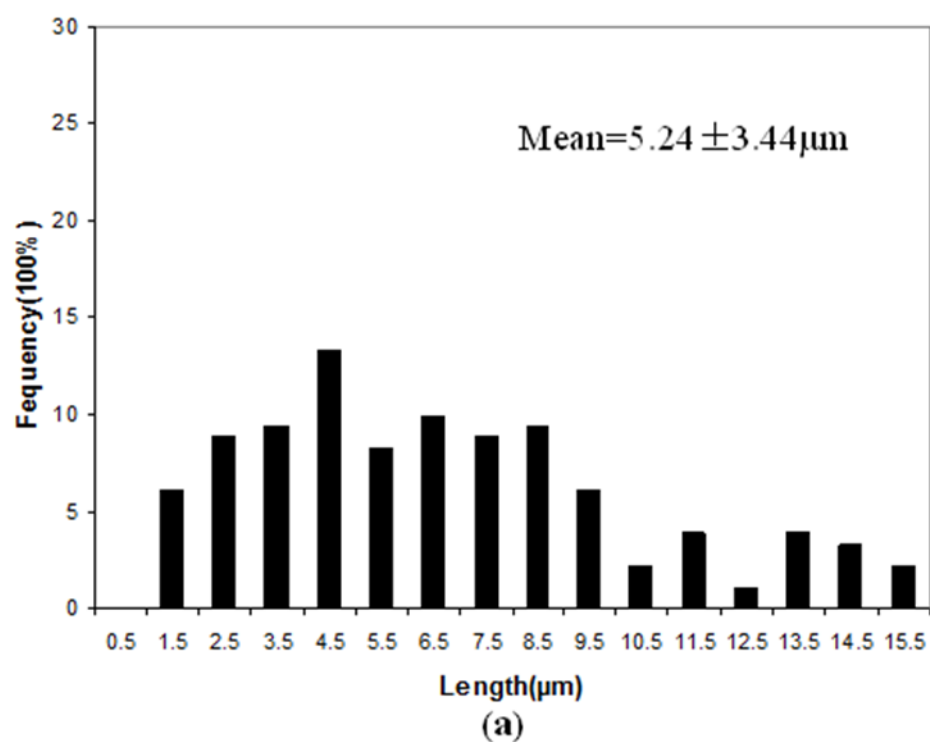
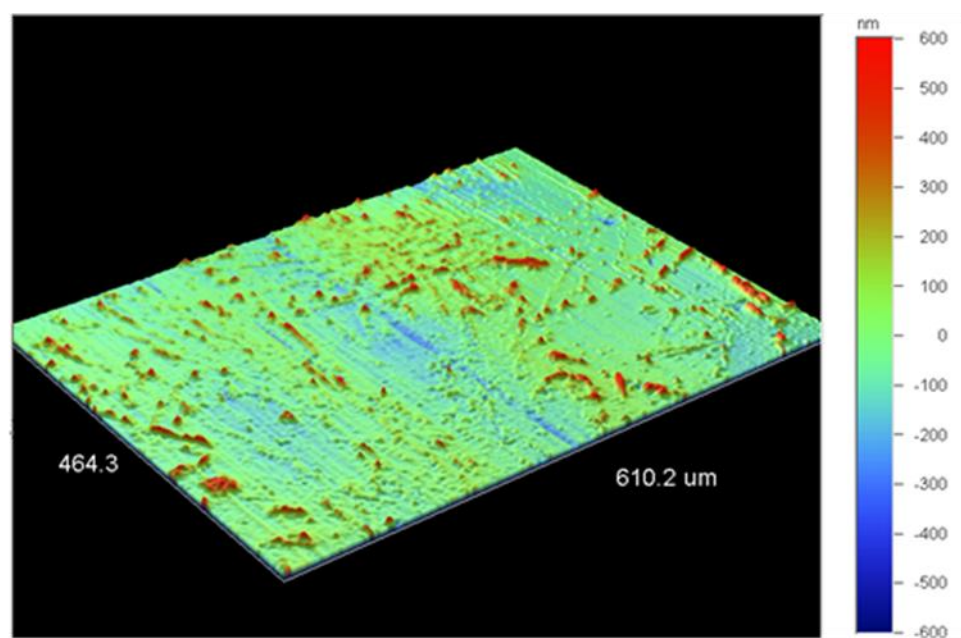
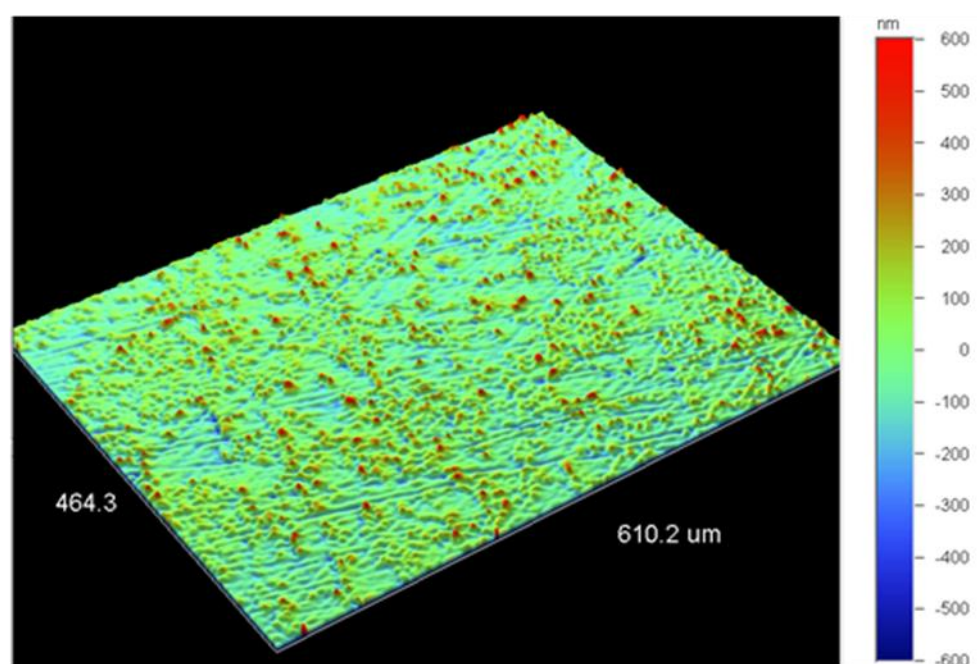


**Fig. 4.10.** Histograms showing Si particle (a) length and (b) width distribution in the brass-chilled Al-Si alloy.



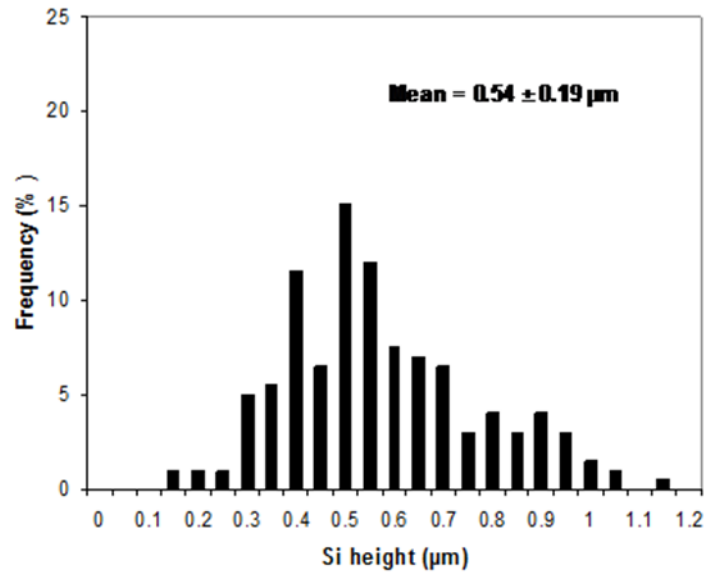


(a)

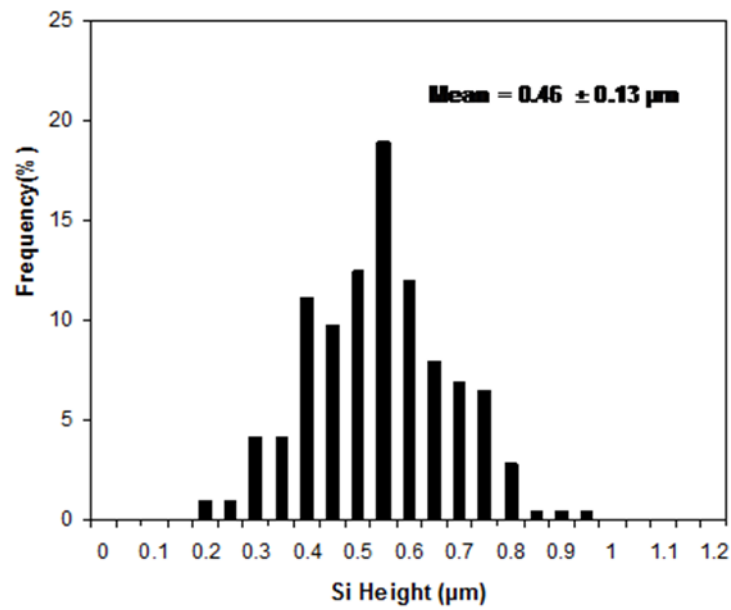


(b)

**Fig. 4.11.** Optical surface profilometer morphology of virgin surface in two engines, (a) sand-cast, (b) brass-chilled showing their  $R_a$  are 74.7nm and 80,17nm respectively.

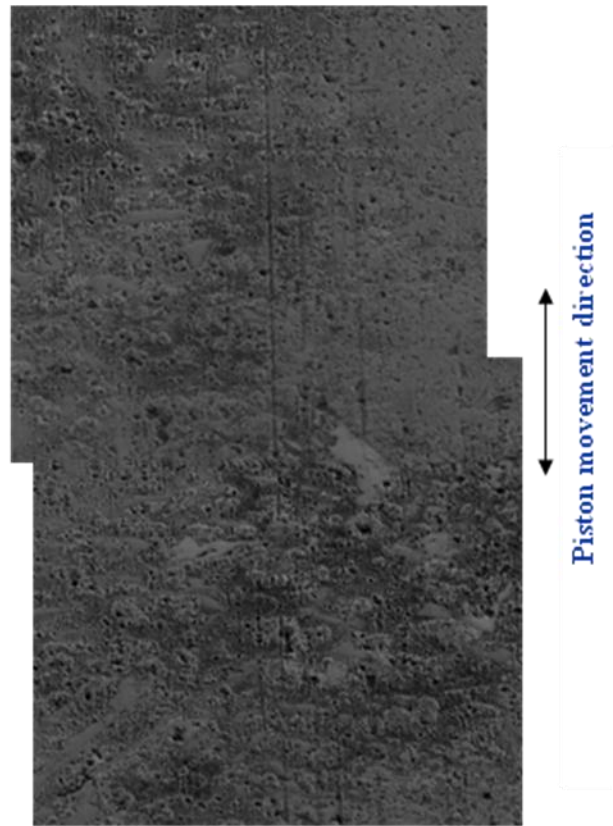


(a)

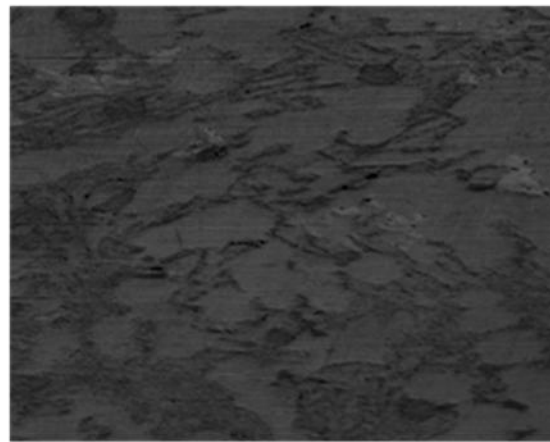


(b)

Fig.4.12 Histograms showing the Si Height Distribution in (a) sand-cast and (b) brass-chilled alloys.



**(a)**



**(b)**

**Fig.4.13** Secondary SEM image of sand-cast engine normal wear surface (a) and virgin (unworn) area (b).

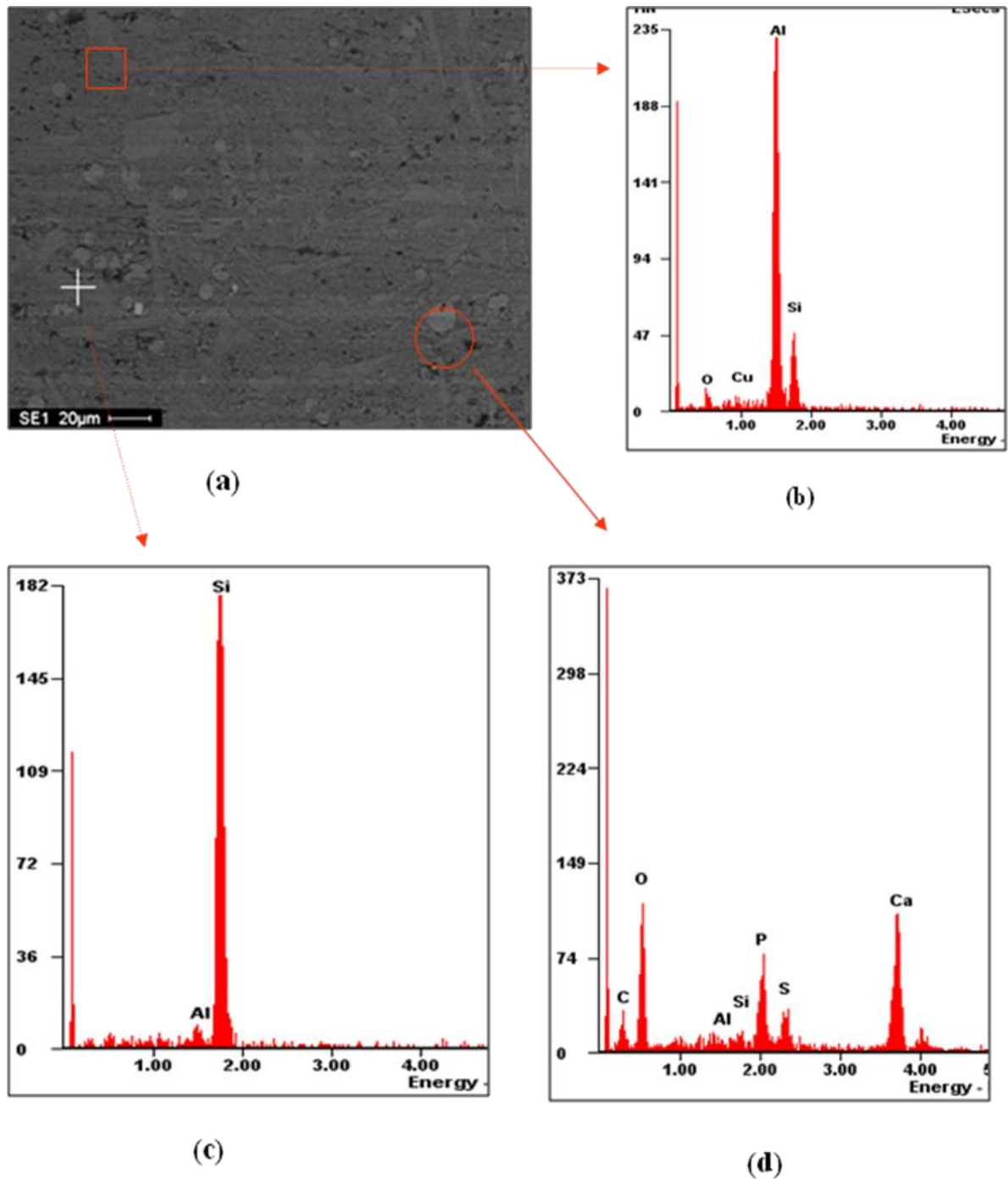


**Fig. 4.14** Secondary SEM micrograph and the EDS spectra showing the elemental surface compositions inside the areas marked in the secondary SEM micrograph in the sand-cast Al-Si alloy engine normal wear surface: (a) secondary SEM micrograph, (b)-(d) the elemental surface compositions inside the areas marked in the secondary SEM micrograph.

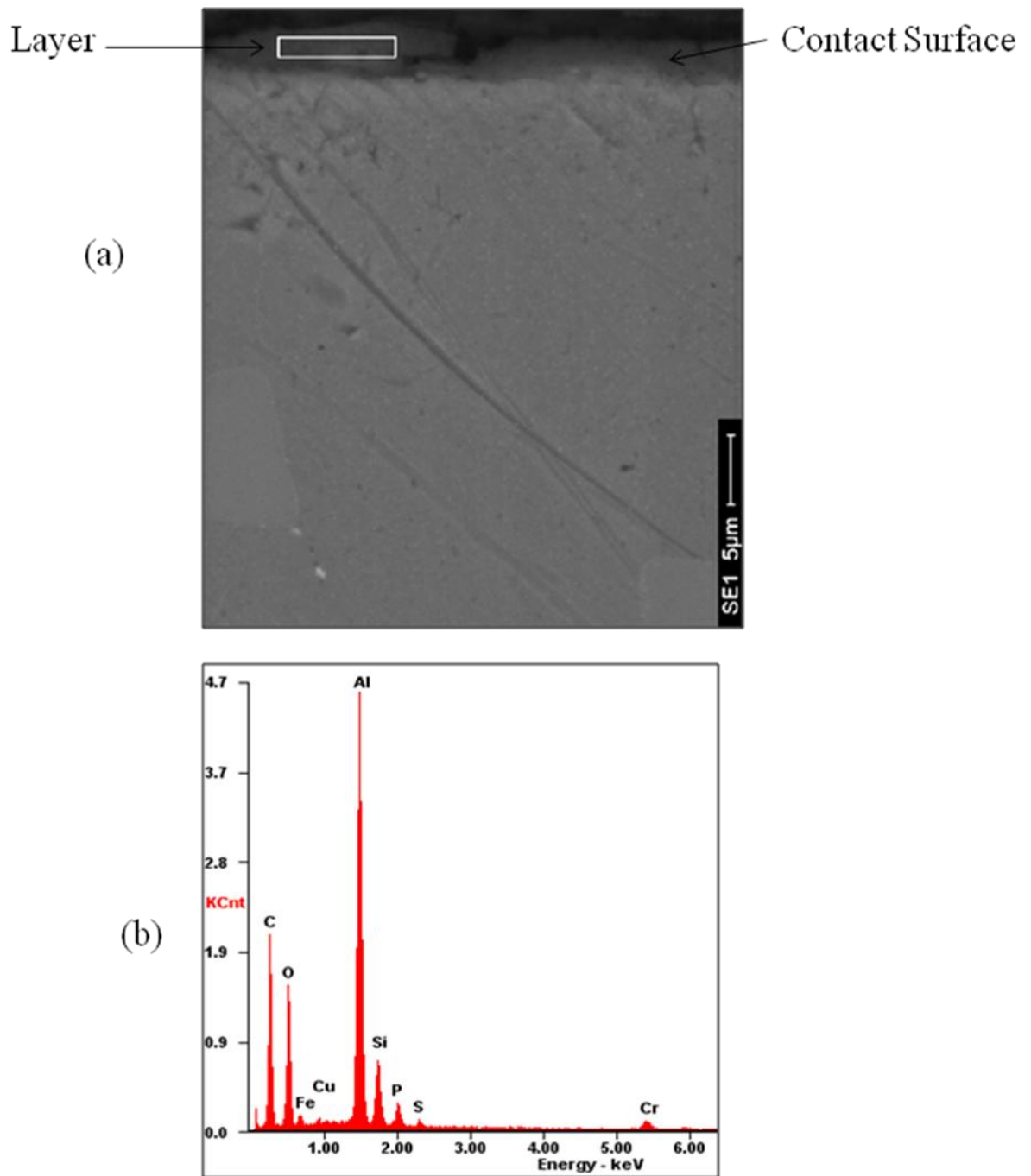
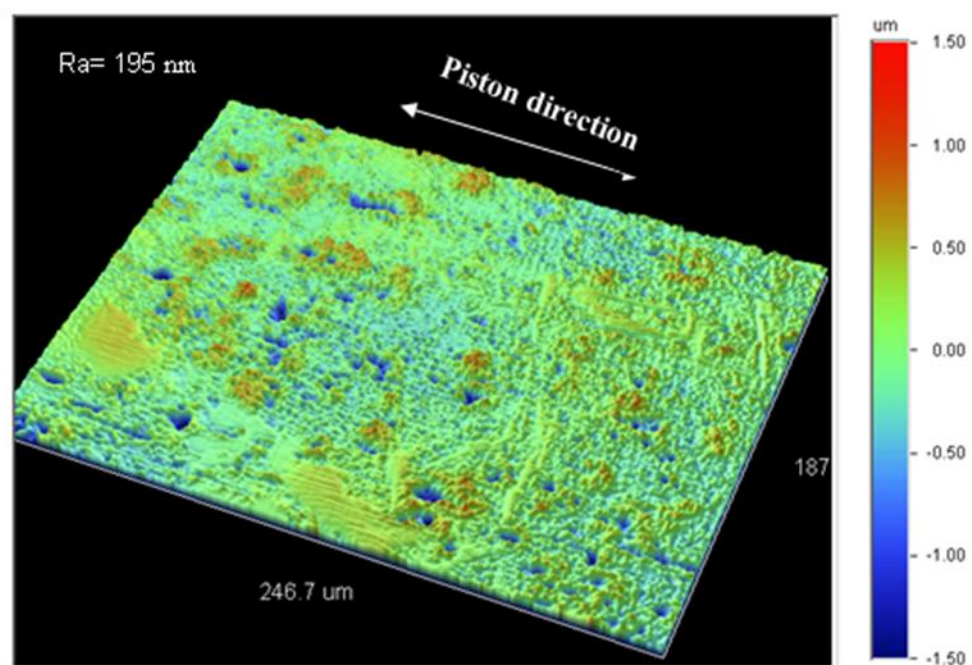
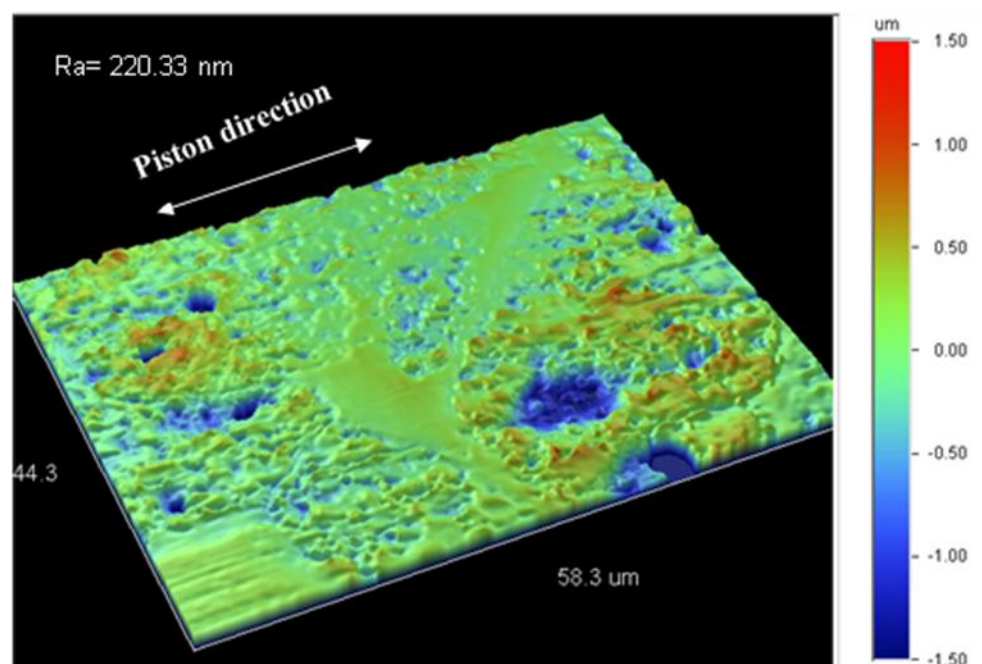


**Fig. 4.15.** Secondary SEM micrographs showing a layer (the rectangle area) formed on the contact wear surface (a) and the EDS spectra identify the components of the regions marked in the sand-cast Al-Si alloy (b).



(a)



(b)

**Fig. 4.16** Optical surface profilometer morphology of wear surface of sand-cast engine at two magnifications, (a) 25 $\times$  and (b) 100 $\times$ . Roughness was determined on an area of  $3.0 \times 4.2 \text{ mm}^2$ .



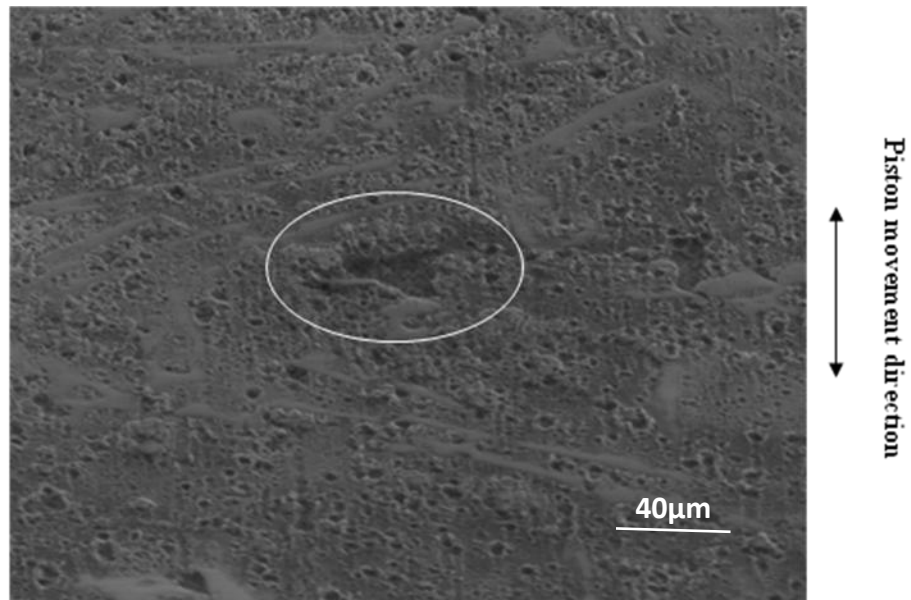


**Fig. 4.17** Secondary SEM image of normal wear surface on the sand-cast engine showing delamination happened on the wear area.

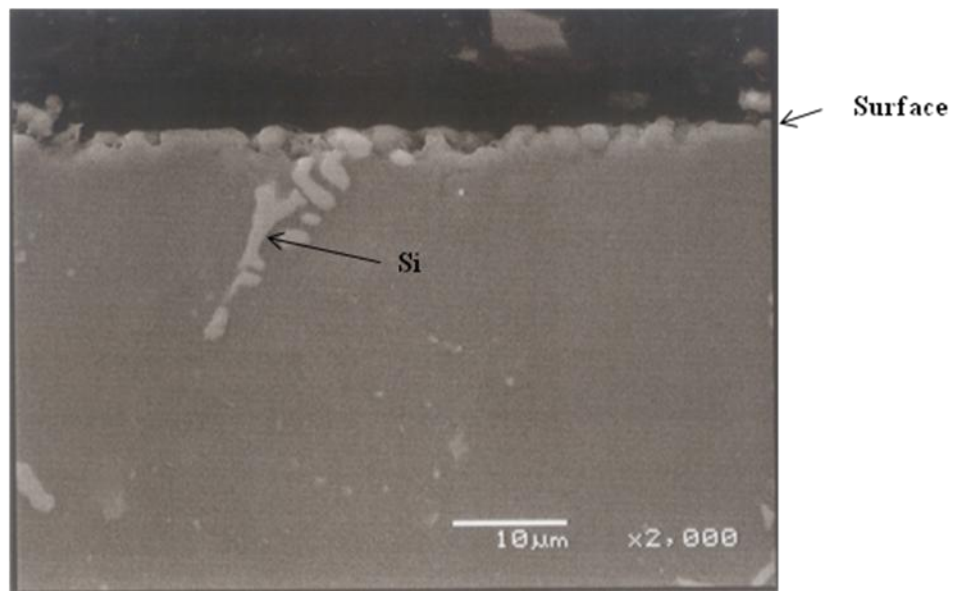


**Fig. 4.18** Cross-sectional optical and SEM showing Si fracture on the contact wear surfaces of sand-cast alloy.

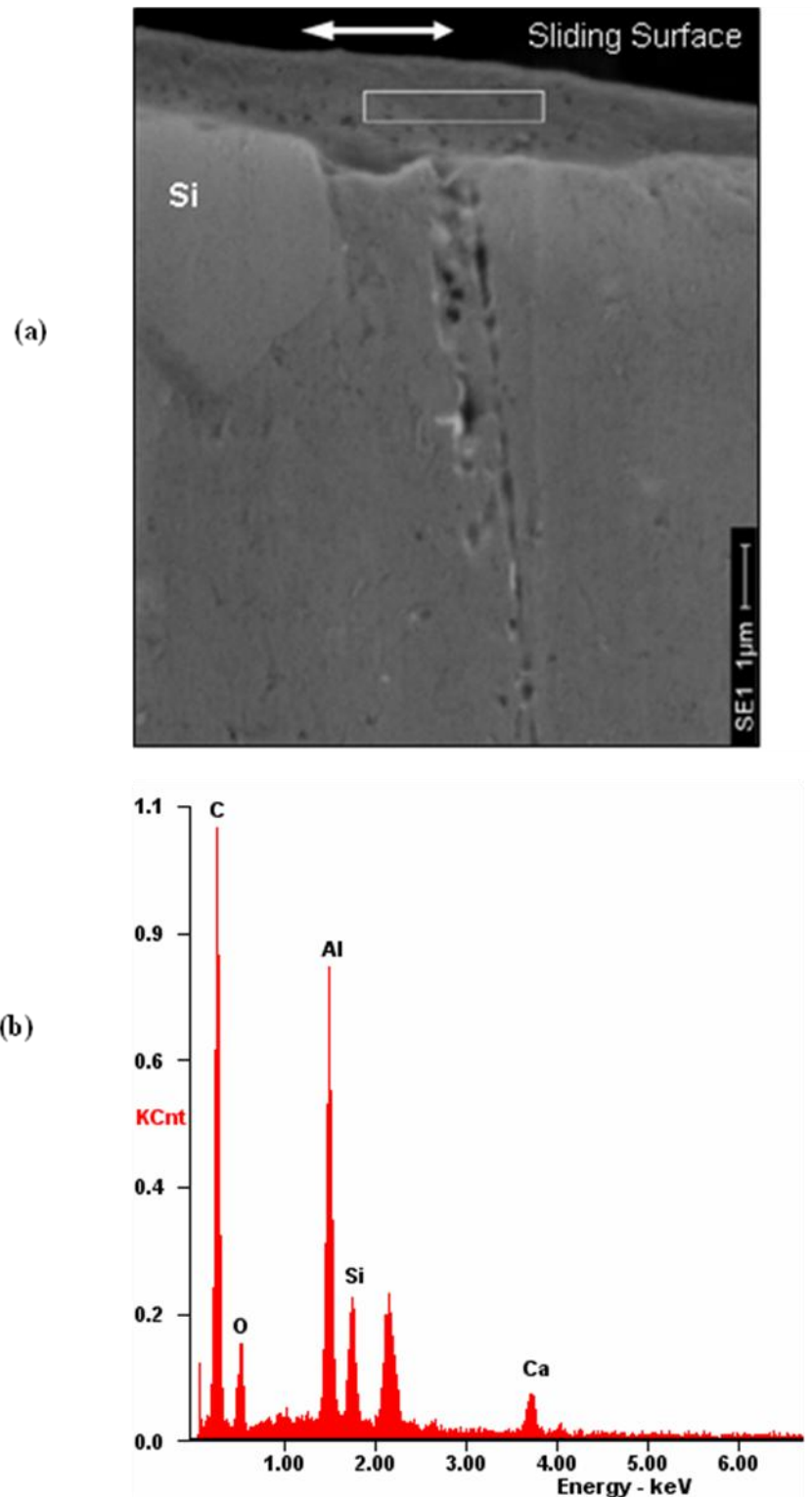


**Fig. 4.19** Secondary SEM micrograph of the layer formed on the contact wear ( $\sim 1\mu\text{m}$ ) of the brass-chilled engine, (b) the EDS spectra identify its components ( the marked area).



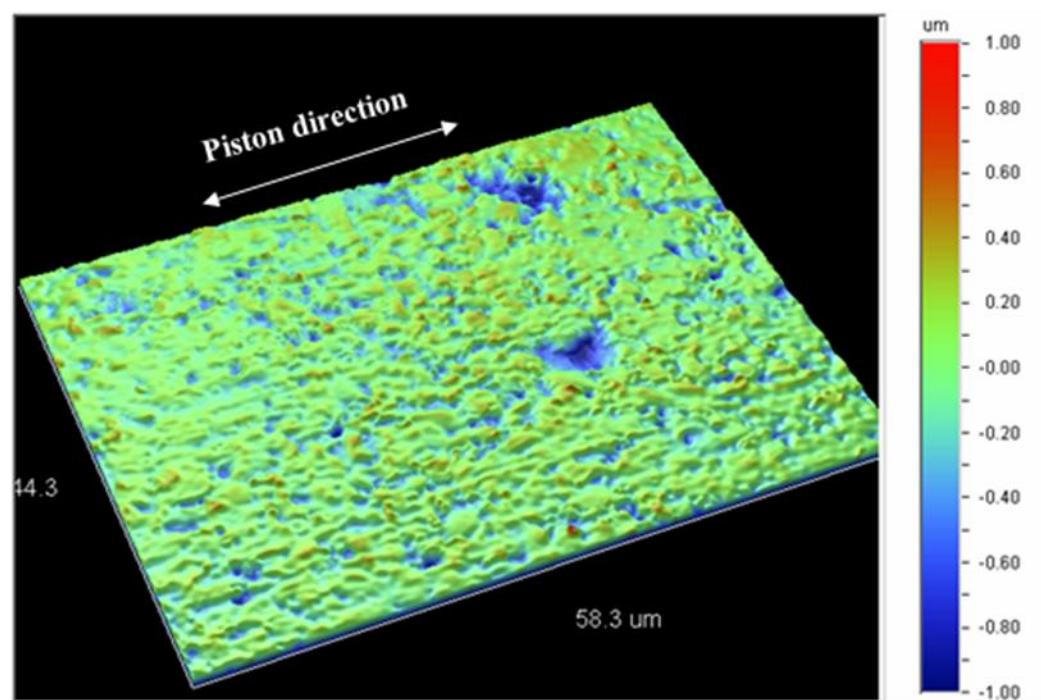
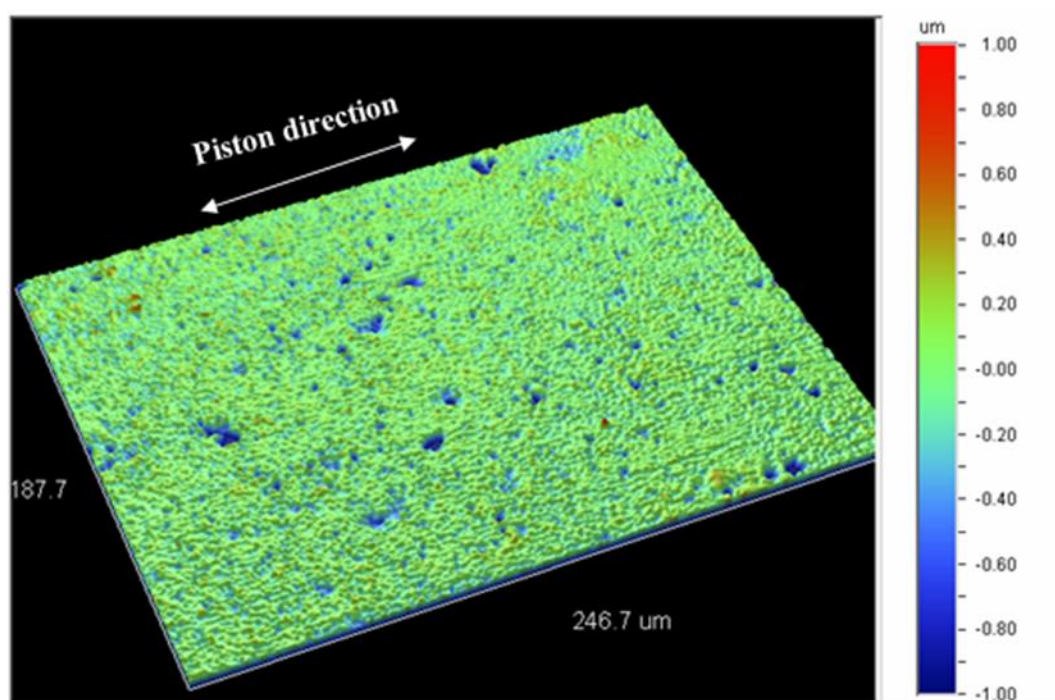


**Fig. 4.20** Optical surface profilometer morphology of wear surface at two magnifications for the brass-chilled engine, (a) 25 $\times$  and (b) 100 $\times$ .

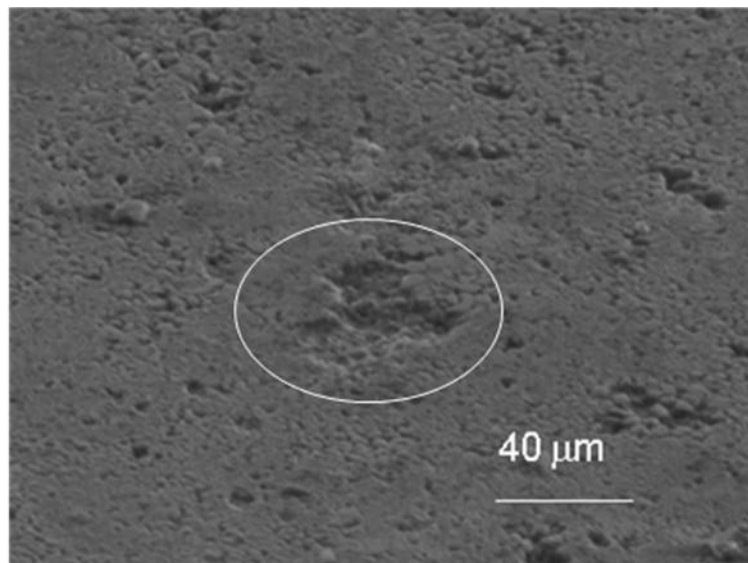


**Fig. 4.21** Secondary SEM micrographs of contact wear surface in the brass-chilled engine showing delamination of the contact surface

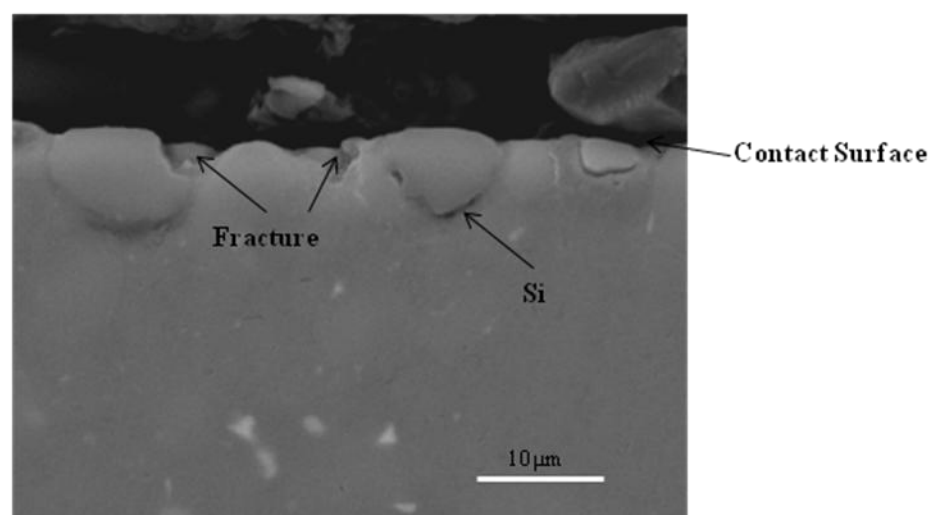


**Fig. 4.22** Cross-sectional SEM image showing Si fracture on the contact surfaces of the brass-chilled alloy.

## **CHAPTER 5**

### **DRY SLIDING WEAR BEHAVIOUR OF Al-Si ALLOYS UNDER CONTROLLED ATMOSPHERIC CONDITIONS**

#### **5.1 Introduction**

This chapter presents the results of the dry sliding wear behaviours of a near eutectic Al–11% Si alloy tested against a steel ring counterface under controlled air and argon atmospheres, using a detailed characterization of worn surfaces and subsurfaces. Dry sliding wear tests were performed in a load range between 0.2N and 170N in air and 0.2N and 100N in argon respectively with a constant velocity of 1m/s and a controlled relative humidity (RH) level of  $5\pm 2\%$  to study the wear mechanisms under controlled atmospheric conditions. A sliding distance of  $4\times 10^3$  m was kept constant for all the tests, unless otherwise terminated due to seizure.

Wear regimes were identified based on wear rate variations within the applied load under controlled dry air and argon atmospheres. Measurable mass loss value was 0.01 mg with the balance used to determine the volumetric wear rates. The friction force was recorded during wear tests and used to calculate COF variation within the sliding distance. To determine the wear mechanisms and transitions between them for the Al–11% Si alloy, an optical microscope Axiovert 25 and a scanning electron microscope (SEM) equipped with energy dispersive X-ray spectroscopy (EDS) were used. The morphologies, worn surface compositions, cross-sections below worn surfaces (subsurfaces), and the loose debris particles generated during sliding wear were all characterized. The worn surface and subsurface hardnesses were measured, and the

hardness values reported represent an average of at least 3 measurements performed at the same depth. The results were analyzed, discussed, and then summarized.

## **5.2 Dry Sliding Wear Behaviour of Al-11% Si Alloy**

### **5.2.1 Wear Regimes and Wear Transitions in Air**

The volume-based wear rate of each sample tested at a given load was determined using the methods described in Chapter 3. The wear rates of the Al-11% Si alloy as a function of normal load tested under an air atmosphere are shown in **Fig. 5.1** on a logarithmic scale. The figure clearly indicates that the wear rates of the alloy increased with increasing the load from 0.2N to 160N. Further increase in the normal load of 170N caused an abrupt rise in the wear rate and resulted in a change of wear regime.

Two wear regimes: mild wear regime (MW) and severe wear regime (SW) were observed. In the MW regime, the wear rates increased from  $1.84 \times 10^{-5} \text{ mm}^3/\text{m}$  at a load of 0.2 N, to  $6.81 \times 10^{-3} \text{ mm}^3/\text{m}$  at a load of 160 N. There are two sub-regimes in MW named MW-1 and MW-2, in agreement with a previous study [40]. In MW-1, the wear rate increased linearly from  $1.84 \times 10^{-5} \text{ mm}^3/\text{m}$  (0.2 N), to  $9.20 \times 10^{-4} \text{ mm}^3/\text{m}$  (30 N). There was a transition regime between 30N and 52N in which the magnitude of the wear rate increased from  $5.72 \times 10^{-4} \text{ mm}^3/\text{m}$  to  $4.50 \times 10^{-3} \text{ mm}^3/\text{m}$ . In MW-2, the wear rates also linearly rose from  $4.50 \times 10^{-3} \text{ mm}^3/\text{m}$  (52N) to  $9.74 \times 10^{-3} \text{ mm}^3/\text{m}$  (160N). The sample surfaces after wear were different for samples tested in each regime, as will be discussed later.

To determine whether or not the wear rates were stable or not during MW regime wear tests, two loads of 10N and 70N, respectively, were chosen to conduct the wear tests. The relationship between volume loss and sliding distance can be seen in **Fig. 5.2**,

which reveals that a near linear relationship existed between the volume loss and the sliding distance [**Figs. 5.2 (a) and (b)**]. These figures indicate that the wear progressed under the steady-state conditions.

At a load of 170N, severe wear occurred with a rate of  $9.45 \times 10^{-1} \text{ mm}^3/\text{m}$ , which was 100 times greater than at 160N ( $9.74 \times 10^{-3} \text{ mm}^3/\text{m}$ ). The test was stopped at a sliding distance of  $2 \times 10^3 \text{ m}$  when machine vibration and a sudden jump in the friction force were observed. Also, large scale material transfer from the sample surfaces to the counterface ring occurred. The worn surfaces were severely deformed and had a shiny, metallic appearance that was typical of severe wear. Metallic and coarse plate-like wear debris was formed from the extrusion at the sample's leading edge.

Typical variations in the steady-state COF vs. the sliding distance for the Al-11% Si alloy samples tested at loads of 70 N and 170 N under a controlled air atmosphere are shown in **Fig. 5.3**. The average COF value at 70N was  $0.47 \pm 0.06$ , and increased to  $0.6 \pm 0.07$  at 170N. This increase of COF was due to the extensive metallic material transfer to the counterface ring surface, and the resultant surface roughening.

### **5.2.2 Wear Regimes and Wear Transitions in an Argon Atmosphere**

Dry sliding wear tests were performed in argon using a block-on-ring type wear machine placed inside an environmental chamber within a load range of 0.2-100N with a controlled RH of  $5 \pm 2\%$ . A pure argon gas flowed continuously into a small chamber built around the sample-counterface assembly at an exit pressure of 2 Psi during the wear tests. The charging time of the argon into the environmental chamber prior to the tests was around 20 minutes, and the sliding distance for each test was normally  $4 \times 10^3 \text{ m}$  for

all loads, except in severe wear conditions where the total sliding distance was limited by the onset of seizure.

**Fig.5.4** uses a logarithmic scale to compare the wear rate vs. load curves of an Al-11% Si alloy tested in argon and air atmospheres with  $5 \pm 2$  % RH. Because M. Cheng and A.T. Alpas definite ultra-mild wear (UMW) as a lubricated condition in which a negligible amount of material is removed [71], low-mild wear (LMW) is used in the study to replace UMW except literature survey. The figure clearly shows that in an argon atmosphere, the wear rates increased along with the applied load. At loads below 10N, the alloy attained low wear (LMW) because the wear rates (in argon) were of the order of  $10^{-5}$  mm<sup>3</sup>/m or less. Between 10N and 80N, the wear rates belonged to those of the mild wear regime. No MW sub-regimes, however, could be identified within the accuracy of these measurements. The wear rates increased from  $1.20 \times 10^{-5}$  mm<sup>3</sup>/m (10N) to  $3.75 \times 10^{-3}$  mm<sup>3</sup>/m (80N). At a load of 100N, the wear rate was  $9.10 \times 10^{-2}$  mm<sup>2</sup>/m, and a transition from MW to SW occurred.

**Figs. 5.5 (a) and (b)** illustrates the changes in volume loss for the Al-11% Si alloy sample at different stages of sliding in an argon atmosphere at 10N and 50 N. It can be seen that volume loss increased linearly with the sliding distance, indicating that steady wear state was attained.

COF variations within the sliding distance under an argon atmosphere at different loads are shown in **Fig.5.6**. The COF initially increased to a maximum, and then dropped to a steady-state value. The distance at which a maximum friction coefficient was observed ranged from 50 to 100 m. The average COF in argon at 10N was  $0.23 \pm 0.04$ . With increases in load, the COF values remained around  $0.5 \pm 0.051$ .

### **5.2.3 Wear Performance Comparisons of Al-11% Si Alloy and A390**

The wear performance of the Al-11% Si alloy tested under dry air and argon atmospheres with a relative humidity level of 5% were compared with those of the A390 Al alloy with 18.5% Si [40, 46] to assess the wear performance of the eutectic alloy compared with to a high silicon content alloy (18%). **Fig.5.7 (a)** revealed that the main wear regimes of the Al-11% Si were the same as those of the A390 in an air atmosphere—namely a MW regime consisting of the two sub-regimes (MW-1 and MW-2), and a SW regime. The Al-11% Si alloy featured a lower load at which transition from MW-1 to MW-2 occurred was lower than found with the A390. Another notable difference was that the MW wear rates were lower in the Al-11% Si. The onset of the second sub-regime MW-2 was characterized by a rapid increase in wear rates in the load range of 30 - 52 N. The same transition occurred between 35 N and 60 N in A390. The Al-11% Si alloy samples tested at loads above 160 N showed very high wear rates that corresponded to the SW regime. The transition loads that prompted the SW in A390 occurred at a similar load of 150N.

The argon atmosphere [**Fig.5.7 (b)**] supported three regimes in both alloys. Below 10N, LMW was observed with wear rates that were less different in both alloys. MW happened between 10N and 80N, while SW occurred above 80N in both alloys. The wear was sensitive to load increase in both alloys. So, there was not much difference between these two alloys in inert atmospheres.

### 5.3 Examinations of Samples Tested in Air

#### 5.3.1 Observation of Worn Surfaces

The optical profilometer images (Wyko) taken from the worn surface's middle section in 5% RH air shown (**Figs. 5.8-5.11**) were obtained after sliding at loads of 1N, 10N, 100N and 170N. The magnifications were all 25 times, and **Fig. 5.12** illustrates the variation of worn surface roughness within normal loads.  $R_a$  is the average roughness,  $R_q$  is the root mean square roughness, and  $R_t$  is the maximum height of the profile. The roughness increased with the normal load. In MW, the roughness ( $R_a$ ,  $R_q$  and  $R_t$ ) increased slowly from 0.907  $\mu\text{m}$ , 1.28  $\mu\text{m}$ , and 16.99  $\mu\text{m}$  at 1N, to 3.04  $\mu\text{m}$ , 3.88  $\mu\text{m}$ , and 24.4  $\mu\text{m}$  at 160N, respectively. The roughness, however, increased dramatically after the transition from MW to SW. At a load of 170N, the roughness ( $R_a$ ,  $R_q$  and  $R_t$ ) was 38.55 $\mu\text{m}$ , 48.31 $\mu\text{m}$ , and 290.27 $\mu\text{m}$  -- more than ten times than sat 160N.

The worn Al-11% Si surfaces were examined using a scanning electron microscopy. Generally, a transferred layer--either in continuous or discontinuous form--was observed for the samples tested in an air atmosphere. Dark, compacted surface layers partially covered the wear tracks. **Figs. 5.13 (a) and (b)** show the secondary and back scattered SEM micrographs of worn surface morphology at the applied load of 5N after a sliding distance of  $4 \times 10^3$  m-- revealing two distinct regions on the worn surface: smooth and crater. In the smooth region, ploughing and scoring extended parallel to the sliding direction, while loose debris particles collected in most of the craters. The widths of the surface grooves were between 4  $\mu\text{m}$  and 20  $\mu\text{m}$ , and the crater diameters got as large as 120  $\mu\text{m}$ . Generally, small equiaxed particles were observed in the crater areas, as shown in **Fig.5.14**. The EDS analysis of the smooth and crater areas (marked as A and B,



respectively, in **Fig. 5.13**), given in **Fig.5.15**, showed that both areas consisted of a mixture of oxidized elements from the Al-11% Si sample and the ring counterface.

The secondary SEM images presented in **Figs. 5.16 (a) and (b)** show the worn surface of the sample tested at loads of 10 N and 100N for a sliding distance of  $4 \times 10^3$  m in air. Grooves extending in the direction of sliding were formed on both surfaces, but the surface grooves grew much wider when the load increased (8-27  $\mu\text{m}$  at 10N and 70-200  $\mu\text{m}$  at 100N), compared to those observed at 5N. It follows that as the normal load increased, deformation became more severe and the grooves became deeper.

**Fig. 5.17** shows the secondary SEM images of the worn surface morphology generated during severe wear. These images were taken from a sample tested at 170 N for a sliding distance of  $2 \times 10^3$  m. The worn surface showed the plastic flow with a characteristic metallic wear of the ridges. Edge cracking was also seen. The surface had a shiny, metallic appearance, while overlapping metal layers were formed by the extrusion of severely deformed material on the surface.

### **5.3.2 Cross- Sectional Observation of Worn Subsurfaces**

The optical microscope images in **Fig. 5.18** provided cross-sectional views of worn surfaces at loads of 5N, 10N, 40N and 100N in air--revealing a severely deformed zone beneath the worn surfaces. An increase in load also seemed to prompt the formation of a continuous layer. As the applied load increased, the percentage of the Al (Si) layers between the oxidized layers increased [**Figs.5.18 (b) and (c)**] until an Al-Si-O layer [**Fig.5.18 (d)**] formed on the worn surface. Back transfer of Al to the surfaces of the oxidized tribolayers generates a multilayered structure consisting of Al (Si) layers sandwiched between oxidized and mechanically mixed layers. **Fig. 5.19** illustrates the

average microhardness of the worn surface in air. Each value is the average hardness of at least 15 measurements. In MW, the hardness of the worn surface first increased with the test load from 248 HV at 10N, to 1700 HV at 70N, and then decreased to 620HV at 160N.

**Fig. 5.20** provides the optical micrographs taken from the transverse tapered cross-sections of Al-11% Si alloy at loads of 10 N and 70N. The tapered sections, taken at an angle of  $5.7^\circ$  to the worn surfaces, provide a 10 times magnification of the subsurface zones. The grooves were deeper and wider at 70N compared to those observed at 10N, and it clearly showed mechanically mixed and oxidized tribolayers on the both surfaces. The tribolayers at 70N, however, were thicker compared to those at 10N.

Tribolayers with thicknesses varying between 4 to 32  $\mu\text{m}$  were generated at 10N (MW-1) [**Fig. 5.20 (a)**]. An examination of the material underneath the worn surfaces revealed that at 70N (MW-2), the tribolayers reached thicknesses of the order of 70 - 80  $\mu\text{m}$  [**Fig. 5.2(b)**]. The tribolayers in MW-2 displayed a layered structure consisting of a mechanical mixture of fractured particles.

The severity of subsurface damage and deformation can be characterized by microhardness measurements taken below the worn surface and plotted as microhardness-depth diagrams. The depth at which the hardness attains a base value is then defined as the plastic zone size. **Fig. 5.21** shows the variations in local microhardness for the aluminum matrix located under the Al-11% Si alloy's worn surface at loads of 10 N and 70 N. The hardness measurements were carried out on transverse tapered sections cut at an angle of  $5.7^\circ$  to the contact surface as a way obtaining a large area of the hardness indentations. The hardness values were an average of 3 measurements performed at the same depth. The microhardness values decreased as measurements were taken

progressively farther from the contact surface. The plastic zone sizes for samples tested at 10N and 70N were about 140 $\mu$ m and 260 $\mu$ m, respectively, and the hardness increased from 85HV to 280HV and 1700HV, respectively—illustrating that the subsurface hardness at 70N was much higher than it was at 10N.

Subsurface microstructures reveal the level of damage in the tribolayers, and the material below the tribolayers. The subsurface microstructures of the Al-Si alloy presented in **Fig. 5.22 (a)** shows the cross-sectional microstructures of the Fe-Al-Si-O tribolayers [**Fig. 5.22 (b)**] formed at a load of 40N. The microstructural features varied along the depth below the worn surface, and while fractured silicon particles were present in the material as deep as 60-70  $\mu$ m below the contact surface, some portions of the tribolayers above these particles were about to be removed during the sliding contact process. They were no longer supported by the underlying material and either transferred to the counterface, or formed loose debris. **Fig. 5.23** shows the cross-sectional microstructures of the tribolayers formed at the loads of 100N, and the Al-Si-O tribolayer [**Fig. 5.23 (b)**] was removed by spallation.

### **5.3.3 Wear Debris**

The wear debris generated during dry sliding in an air atmosphere was collected and examined using a scanning electron microscopy equipped with an energy dispersive X-ray spectroscopy. An increase in the applied normal load formed wear debris of various shapes and sizes. The debris size ranged from a few microns, to a few millimeters. Visually, the debris produced at 20 N appeared in the form of a dark, brown powder. The SEM micrograph (**Fig. 5.24**) shows the debris produced at a load of 20 N after a sliding distance of  $4 \times 10^3$  m that was mainly composed of very fine, equiaxed particles which

were approximately 0.5-17 $\mu\text{m}$ , but also contained plate-like and ribbon-shaped iron particles in smaller amounts that reached 170  $\mu\text{m}$  in length and 50  $\mu\text{m}$  in width. The EDS analysis given in **Fig. 5.25** revealed that the fine and large debris particles were a mixture of Al, Si, Fe, and oxygen. The ribbon-shaped particles had an appearance similar to machined chips, and were mainly composed of Fe-- indicating that they were cut from the steel counterface [**Fig. 5.25(a)**].

As the load increased, the size and the fraction of metallic, plate-like particles in the debris increased. The SEM micrographs provided in **Figs. 5.26 (a) and (b)** show the typical debris morphologies produced at 70 N after sliding to a distance of  $4 \times 10^3$  m. They were thin (5-20  $\mu\text{m}$ ) and relatively flat, reaching a size of 500-600  $\mu\text{m}$ . The EDS analysis presented in **Fig. 5.23 (b)**, shows that they were metallic flakes, rich in Al with small amounts of Fe and O. The presence of Al-rich debris indicates that some portions of the tribolayers were removed, and the counterface came in contact with the exposed Al-Si surface, removing pieces of it.

**Fig. 5.27** presents the debris morphology produced in the severe wear regime from the Al-11% Si alloy. The wear debris from the SW regime was composed of large, metallic flakes. The worn surfaces, wear debris and the transfer layer on the counterface all had chemical compositions that were similar to that of the unworn Al-Si samples-- indicating that SW corresponded to load levels where the tribolayers either did not formed or could not be retained on the worn surfaces due to the thermal softening of the alloy. The characteristic features of the worn surfaces and the debris particles generated during MW and SW are summarized in **Table 5.1**.

## 5.4 Examination of Tested Samples in Argon

### 5.4.1 Worn Surfaces

**Figs. 5.28-5.31** present the optical profilometer images of the worn surfaces after sliding at loads of 1N, 50N, 80N, and 100N. **Fig. 5.32** illustrates the variations in worn surface roughness with normal loads. The roughness increased along with the normal load, with the roughness ( $R_a$ ,  $R_q$  and  $R_t$ ) increasing slowly from 1.1 $\mu\text{m}$ , 1.4  $\mu\text{m}$  and 8.3  $\mu\text{m}$  at 1N to 10.0  $\mu\text{m}$ , 12.3  $\mu\text{m}$  and 70.8  $\mu\text{m}$  at 80N, respectively. The roughness did not increase dramatically like that happened under an air atmosphere from MW to SW, however. At a load of 100N, the roughness ( $R_a$ ,  $R_q$  and  $R_t$ ) was 11.2  $\mu\text{m}$ , 13.3  $\mu\text{m}$ , and 74.4  $\mu\text{m}$ , respectively. Comparisons of worn surface roughness under air and argon atmosphere can be found in **Table 5.2**.

SEM micrographs of the samples tested in an argon atmosphere at 1N, 50N and 80N are shown in **Figs. 5.33, 5.34, and Fig.5.35**, respectively. At 1N, the surfaces appear smooth with very fine grooves parallel to the sliding direction, and there was no evidence of craters or cavities. At higher load, like 50N, the surfaces revealed fine grooves and narrow, white patches in the sliding direction. The high-magnification image of these patches [**Fig. 5.34 (b)**] indicated some shearing. When the load increased to 80N, the grooves became wider and deeper, covering much larger patches compared with those at 50N. Above 80N, SW occurred and the surface had a shiny, metallic appearance just like that of the samples tested under air atmosphere (**Fig.5.35**). **Fig. 5.36** shows the wear edge of the specimens at 1N and 50N in an argon atmosphere. At 50N, flake-like layers were observed [**Fig. 5.35 (a)**]. The EDS analyses presented in **Fig. 5.37** indicate that the worn surface was composed of Al-Si-Fe-O at 1N, and Al-Si with much less O at 50N.

#### 5.4.2 Subsurface Microstructures

**Fig. 5.38** displays the optical micrographs taken from transverse, tapered cross-sections of samples at loads of 10N, 50N, and 80N in argon. At a load of 10N, a compact tribolayer was formed, while a ductile tribolayer was seen at a load of 50N. At the higher load of 80N, the surface was heavily damaged. **Fig. 5.39** shows the variations in local microhardness for the aluminum matrix under the worn surface at loads of 10 N, 50N, and 80N in argon. The microhardness values increased as the measurements were taken progressively closer to the contact surface at loads of 10N and 50N. On the other hand, the microhardness values decreased at 80N, and maximum hardness was obtained at 160 mm beneath the worn surface—suggesting that the microhardness near the worn surface decreased as the load increased.

The tribolayers formed on the contact surface during the wear tests in argon at 10N, 50N, and 80N had different morphologies and chemical compositions. EDS analyses were conducted to obtain the elemental chemical composition of the tribolayers, which formed during a stable stage at 10N and were rich in matrix Al, low Si, and low Fe. The distributions of Al, Fe, and Si were homogeneous. At 50N they had the same chemical compositions as the Al-Si alloy matrix (**Fig. 5.40** and **Fig. 5.41**). As the load increased, the percentage of the counterface covered with Al transfer layers increased, and the transfer patches became almost continuous and enlarged to a macro scale.

In the argon atmosphere, the debris had a flaky morphology under all conditions. The sizes of the debris varied by a few microns, and were larger at higher loads than at lower loads. The formation of metallic plates/ flakes or delamination wear debris was attributed to subsurface crack initiation and growth at critical depth.

## 5.5 Discussion

### 5.5.1 Wear Comparison under Air and Argon Atmospheres

The wear results presented clearly indicate that the wear resistance of Al-11% Si was better under an argon atmosphere than under an air atmosphere, for certain wear regimes (**Fig.5.4**). Particularly below 25N, nearly one order of magnitude of improvement can be observed. The wear rate increases with the load under both air and argon conditions.

In the air atmosphere, at low loads, the worn surface revealed craters (**Fig.5.13**), and the corresponding debris displayed mainly fine powders (oxide particles, **Fig.5.25**). The worn surfaces in 5% RH air were characterized by mixed and oxidized tribolayers composed of Fe, Al, Si, and O [**Fig. 5.20 (a)**]. The tribolayers formed in the argon test during an UMW regime were composed of Al-(Si) with a very small amount of Fe and less O [**Fig. 5.40 (b)**]. The surface generated in argon tests was relatively smooth and exhibited only grooves, with no evidence of the formation of craters or an accumulation of loose debris particles on the contact surfaces, contrary to those observed in air. Mild wear happened in argon atmospheres above 10N, producing tribolayers composed of Al-(Si) and a very small amount of Fe (**Fig.5.41**), suggesting that the structures and compositions of the tribolayers formed in the two different environments are totally different.

The deformed zone underneath the tribolayer was also different. The tribolayers formed in air were soft (about 275 kg/mm<sup>2</sup>) and brittle, with the depth of the deformed zone about 140µm at 10N (**Fig.5.21**). On the other hand, the Al-(Si) tribolayers formed in an argon atmosphere at the same load was harder (about 875 kg/mm<sup>2</sup>), as recorded in

**Fig.5.39.** The depth of the deformed zone under the tribolayer was approximately 100  $\mu\text{m}$ , and the higher hardness values observed in the tribolayer formed under an argon atmosphere can be attributed to the presence of a homogeneous mixture of Al, Si, and Fe that has formed from the fracture and compaction of heavily strained asperities. Based on these results, the Al-(Si) tribolayers formed in argon during the UMW regime were harder and more ductile compared to those generated in an air atmosphere, implying that the subsurface damage was more extensive when the tests were done in air.

As the load increased from 10N to higher loads, the tribolayers that formed on the sample tested in air contained more and more aluminum, and less iron and oxygen. The tribolayers formed under argon, however, were composed of the same chemical compositions as the Al-Si alloy matrix.

The results of the present study revealed distinctly different mechanical mixed layers for the specimens tested under argon and oxygen atmospheres. Under an argon atmosphere, there was a stable and strong interface that illustrated the strong adhesion between the layer formed and the matrix. The composition of the mechanical mixed layer formed under oxygen atmosphere at higher loads shows much less Fe content, and an enrichment of Al from the matrix. It remained as metallic Al in the argon atmosphere, but existed as oxide under oxygen atmosphere.

Another interesting result was obtained from studying the deformation zone, using hardness measurements beneath the worn surface. The hardness increased continuously up to the surface in air at all loads in MW (**Fig. 5.21**), while in argon, only loads below 50N had the same trend and a soft zone was observed at 80N in argon (**Fig.5.39**). As a



result of decreased hardness, larger deformation caused material metal transfer from sample to ring, leading to seizure at relatively lower transition loads from MW to SW.

### **5.5.2 Wear Mechanism under Controlled Atmospheres**

#### **5.5.2.1 In Air**

Transitions in wear behaviour can be attributed to a competition between strain hardening and thermal softening that occurs at the contact surface under dry sliding wear conditions. The wear resistance is closely related to the formation and the stability of the tribolayers on the contact surfaces. As shown in the previous sections, the formation and removal of the tribolayers during sliding wear depend on the sliding speed, load as well as on the atmospheric conditions. During sliding wear in air, three stages have been identified in the formation of tribolayers. First, the original surface films are mechanically broken down until increasing metal to metal and oxide to metal contact occurs, so that as fresh metal surfaces are exposed to air, they oxidize (Region I). Next, wear particles covered with an oxide film build up in the wear track, forming compacted oxide islands and separating the surfaces to reduce the percentage of metal to metal and metal to oxide contact, which also reduces friction (region II). Finally, the build up a wear particles layer is compensated by the breakdown of the oxide islands (Region III) [22].

At low loads in an air atmosphere, the wear mechanism is a combination of oxidative and abrasive. During the process of material removal process, the oxide particles accumulate at random sites in the direction of sliding (**Fig.5.4**). As these loosely bond, they detach easily [**Figs.5.18 (a) and (b)**]. During sliding, the hard oxide particles adhering on the surface do not flow easily. The matrix thus flows over these particles,

resulting in the formation of bands [Fig.5.18 (c)], so that at high contact pressure (or load), the oxide particles from the steel and the block surface adhere to the block surface [Fig.5.18 (d)]. Once this layer has formed, it protects the matrix and reduces the amount of removal that takes place as a result of delamination. Under high loads, with an increase in sliding distance, the rise in temperature due to friction leads to over-aging phenomena near the subsurface, which prompts softening until large material transfers shift from the samples to the counterface ring, promoting seizure that results in severe wear.

#### 5.5.2.2 In Argon

Unlike the wear that occurs in air, there are only two stages in an argon atmosphere. Stage I involves the original surface films mechanically broken down until metal to metal contact increases. The fact that the metal surfaces are not exposed to air means that no new oxide layers form. In stage II, the build up of a wear particles layer is compensated by the breakdown of contact metals, suggesting that the wear behaviour in argon can be attributed to the competing effects of strain rate and temperature developed during the sliding of two mating surfaces. Below 10N, in an argon atmosphere, the mixed mechanical layer was a homogeneous mixture of Al, Si, Fe and small amount of O (remains from the beginning) [Fig.5.40], resulting higher wear resistance than in air, as well as LMW (Fig.5.4). As the load increased, however, the tribolayer formed was removed, and percentage of metal to metal contact increased. A new tribolayer formed -- a mixture of Al-Si (Fig.5.41) -- displaying some ductility. According to Shunke et al. [22], fracturing an oxide film by brittle failure absorbs much less energy than shearing through ductile metal, which suggests that in the MW regime in an argon atmosphere, the wear rates were lower than those in an air atmosphere (Fig.5.4) at the same load—a fact

can be attributed to the fact that the tribolayers formed in argon were uniform and softer than those formed in air, which were brittle and easily removed. The wear was more sensitive to load in MW when tested in argon than in air, and that seizure wear occurred more easily (**Fig.5.5**) because the thermal softening dominate the wear process in the competition between strain hardening and thermal softening that occurs at the contact surface. Near surface temperatures were high enough to lower the shear strength of the sub-surface layer and promote extensive material transfer from the wearing alloy to the steel counterface. All of which can be proved by the fact that the microhardness of the worn surface decreased with the increase of the test load (**Fig.5.39**).

**Table 5.1** The characteristics of wear regimes in an air atmosphere

	<b>Mild Wear (MW)</b>		<b>Severe Wear (SW)</b>
	<b>MW-1</b>	<b>MW-2</b>	
<b>Wear rate (mm<sup>3</sup>/m)</b>	-Of the order $10^{-4}$ - $10^{-3}$ -Stable	-Of the order $10^{-3}$ - $10^{-2}$ -Stable	-Higher than $10^{-1}$ - Unstable
<b>Tribolayers</b>	-Tribolayers(Fe-Al-Si-O) -Continuous	-Multilayered structure Tribolayers(Fe-Al-Si-O)+Al layer	-Al-Si tribolayer
<b>Wear debris</b>	-Dark-brown coloured powder mixed with Fe, Al, and Si and O -Very fine equiaxed particles+ small amounts of ribbon shaped particles ( Fe chips), and Plate-like particles (Fe-Al-Si-O)	-Plate-like particles composed of Fe, Al, and Si and O -Metallic Al flakes (Al-Si)	-large metallic flakes Al-Si particles
<b>Worn Surfaces</b>	-Surface with shallow grooves and - Crater areas filled with loose debris, -Microhardness increased with the increase of test load	-Surface with wide and deep grooves -Microhardness decreased with the increase of test load	Extensively deformed Much rough

**Table 5.2** Comparisons of worn surface roughnesses formed during wear under air and argon atmosphere

<b>In air</b>				<b>In argon</b>			
Load (N)	Ra (μm)	Rq(μm)	Rt(μm)	Loads (N)	Ra (μm)	Rq(μm)	Rt(μm)
1	0.907	1.28	16.99	1	1.1	1.39	8.28
10	1.79	2.36	23.73	10	1.6	1.78	15.2
100	3.35	4.36	26.7	50	5.4	6.83	42.15
160	3.04	3.88	24.4	80	10.04	12.34	70.79
170	38.55	48.1	290.27	100	11.18	13.32	74.42

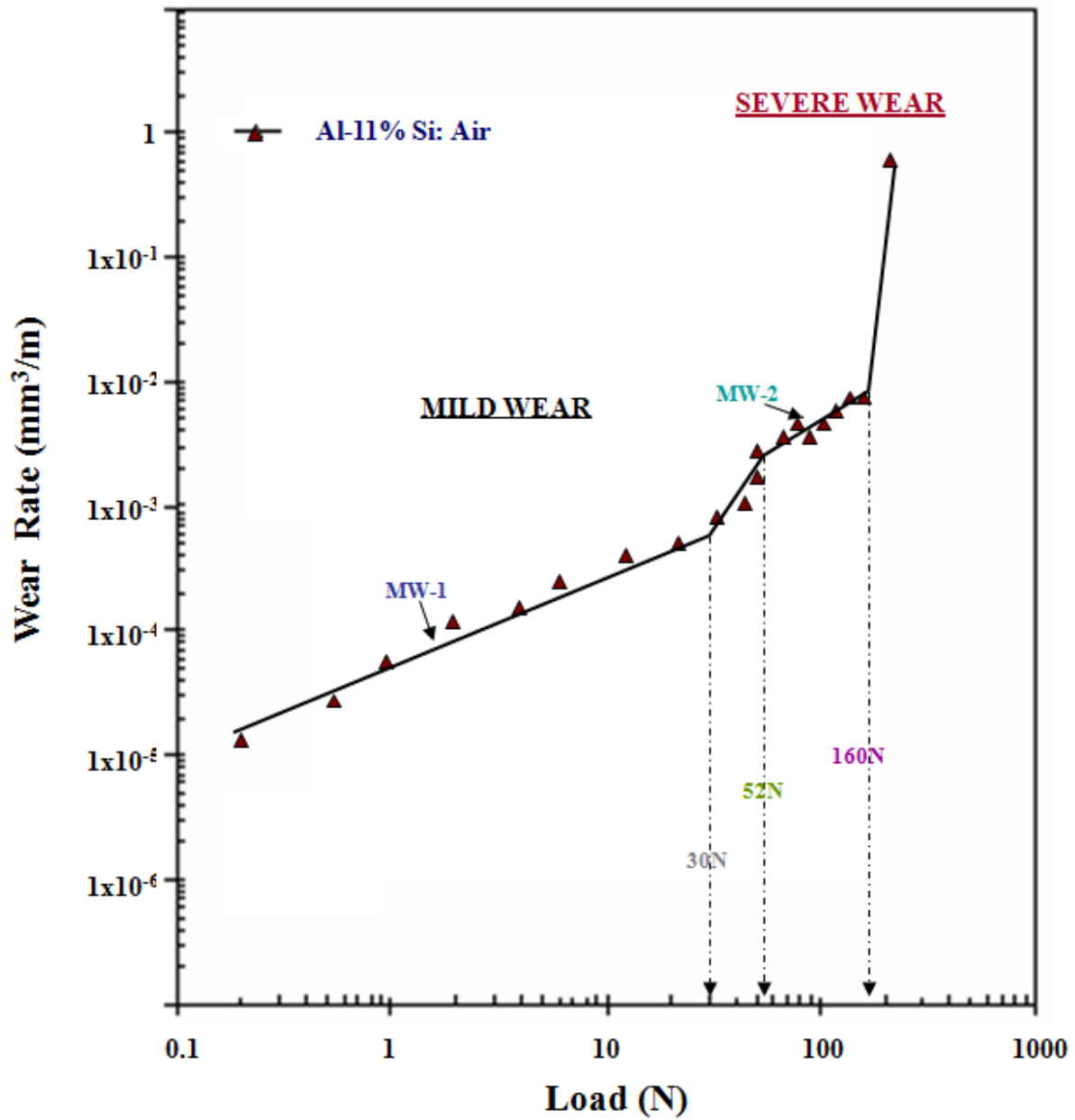


**Fig. 5.1** Wear rates and transitions of Al-11% Si alloy with increasing the test load. The tests were conducted at a constant speed of 1 m/s and a sliding distance of  $4 \times 10^3$  m in dry air (5% RH). MW-1 (at loads below 30 N) and MW-2 (at loads between 52 N and 160 N) are the sub-regimes of mild wear. Severe wear occurred at loads above 160 N.

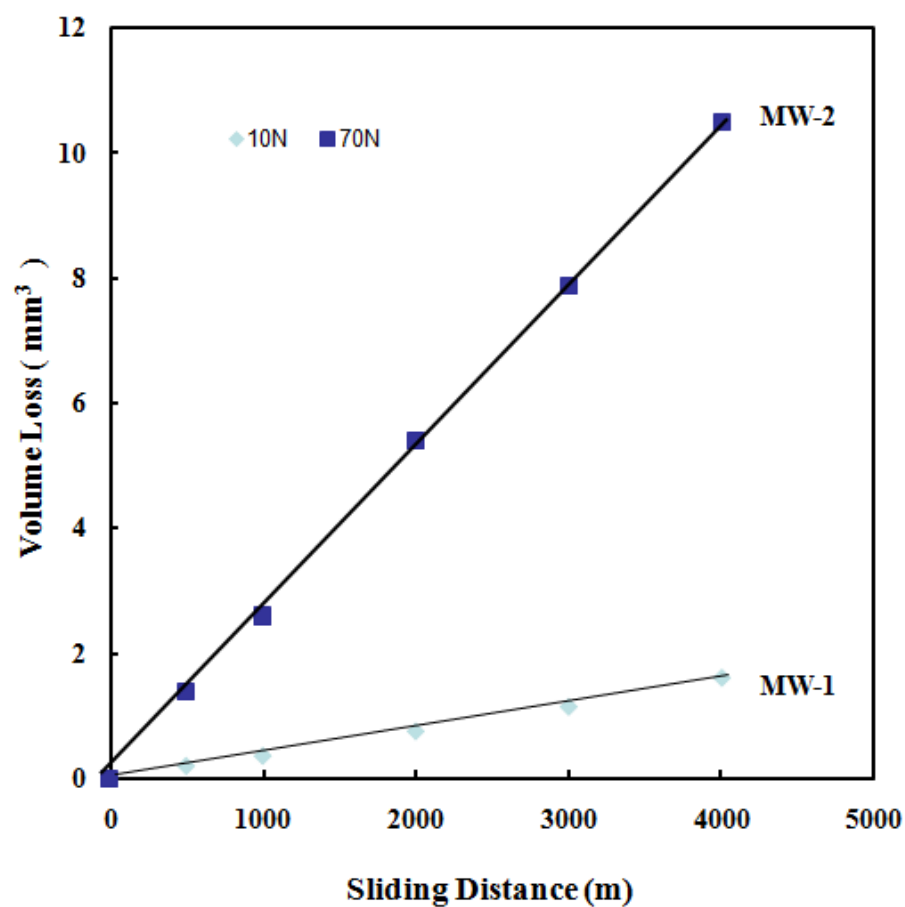
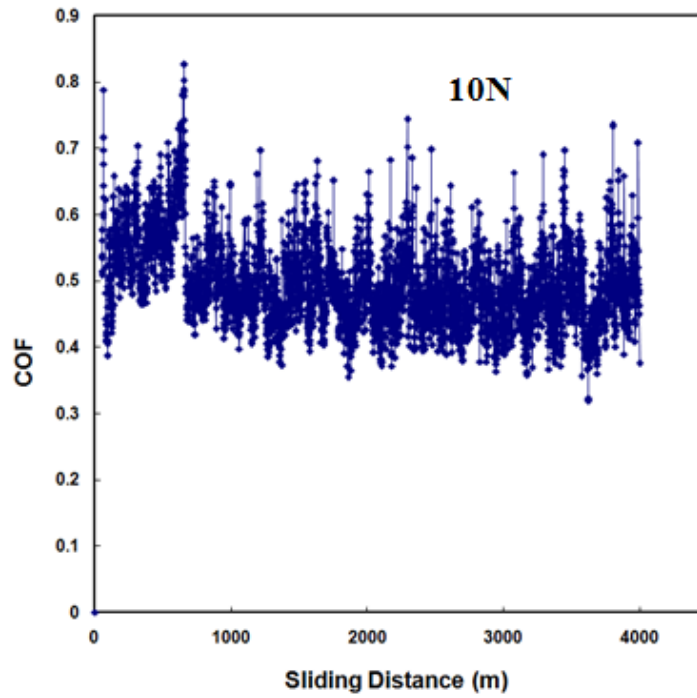
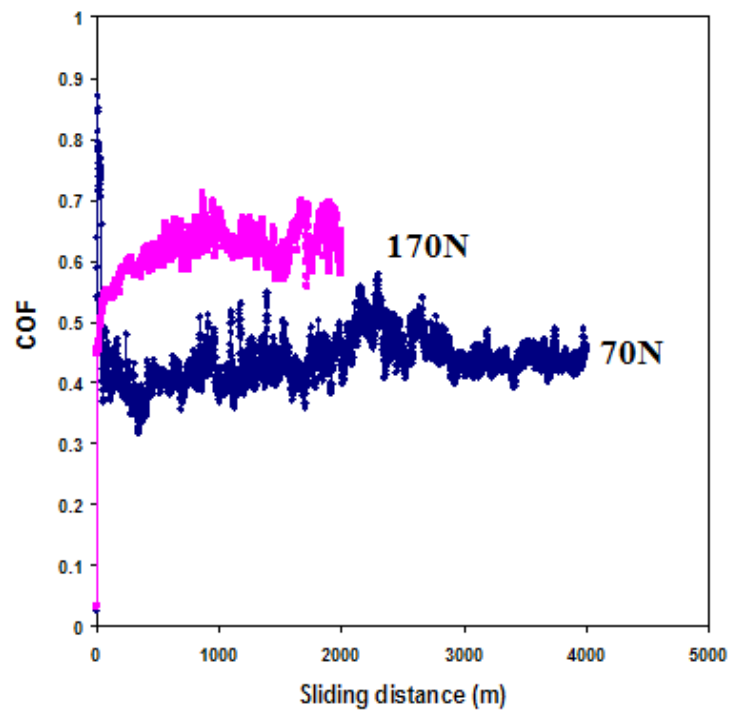


**Fig. 5.2** Volume loss vs. sliding distance plots of Al-11% Si alloy for mild wear at loads 10 N and 70 N in air ( $5 \pm 2\%$ ). Volume losses determined by mass loss measurements showed the steady state nature of the mild wear. The volumetric wear rate can be calculated from the slopes of the volumetric loss vs. sliding distance curves.



(a)



(b)

**Fig.5.3** Variation of the coefficient of friction (COF) with the sliding distance at three loads in air (5% RH): at 10N (a), at 70 N and 170 N (b).



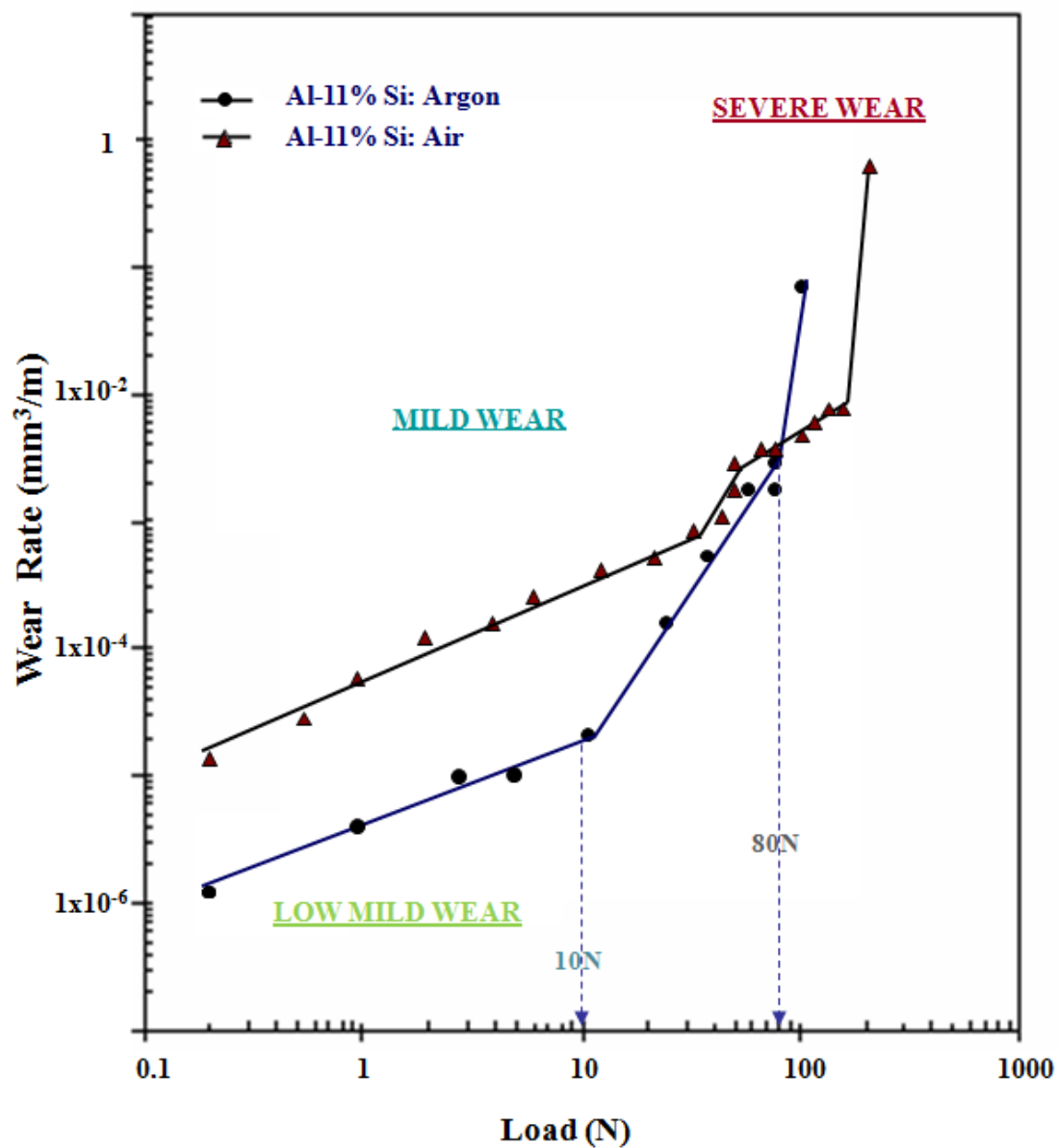
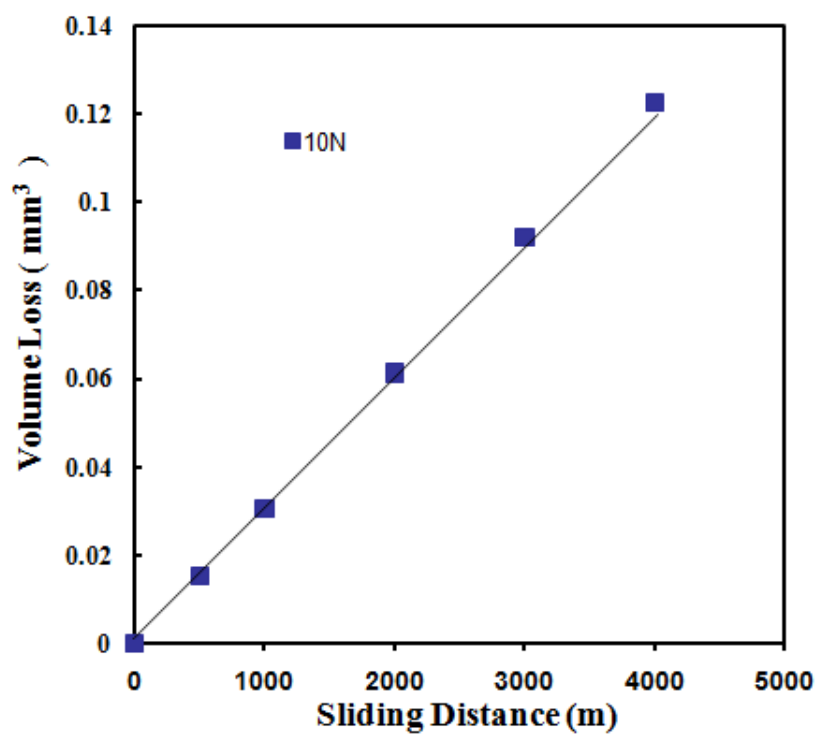
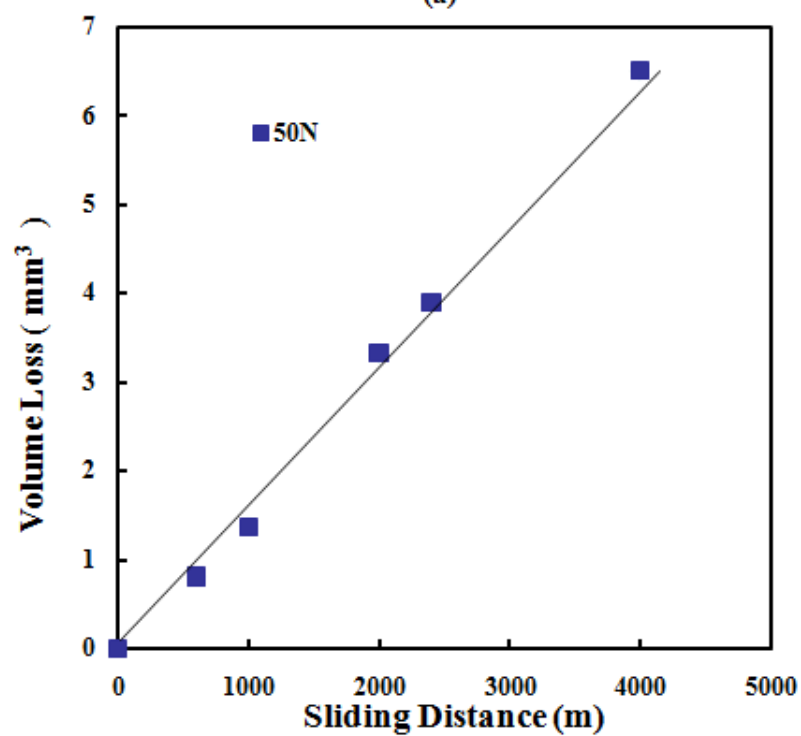


Fig. 5.4 Variation of the wear rates with the test load for Al-11% Si tested in an argon atmosphere and in air (5%RH). UMW was observed at loads <10 N, MW between 10N and 80N and SW above 80N.



(a)



(b)

**Fig. 5.5** The micrographs showing volume loss vs. sliding distance at sliding distance of 4000 m in argon at loads (a) 10N and (b) 50N.

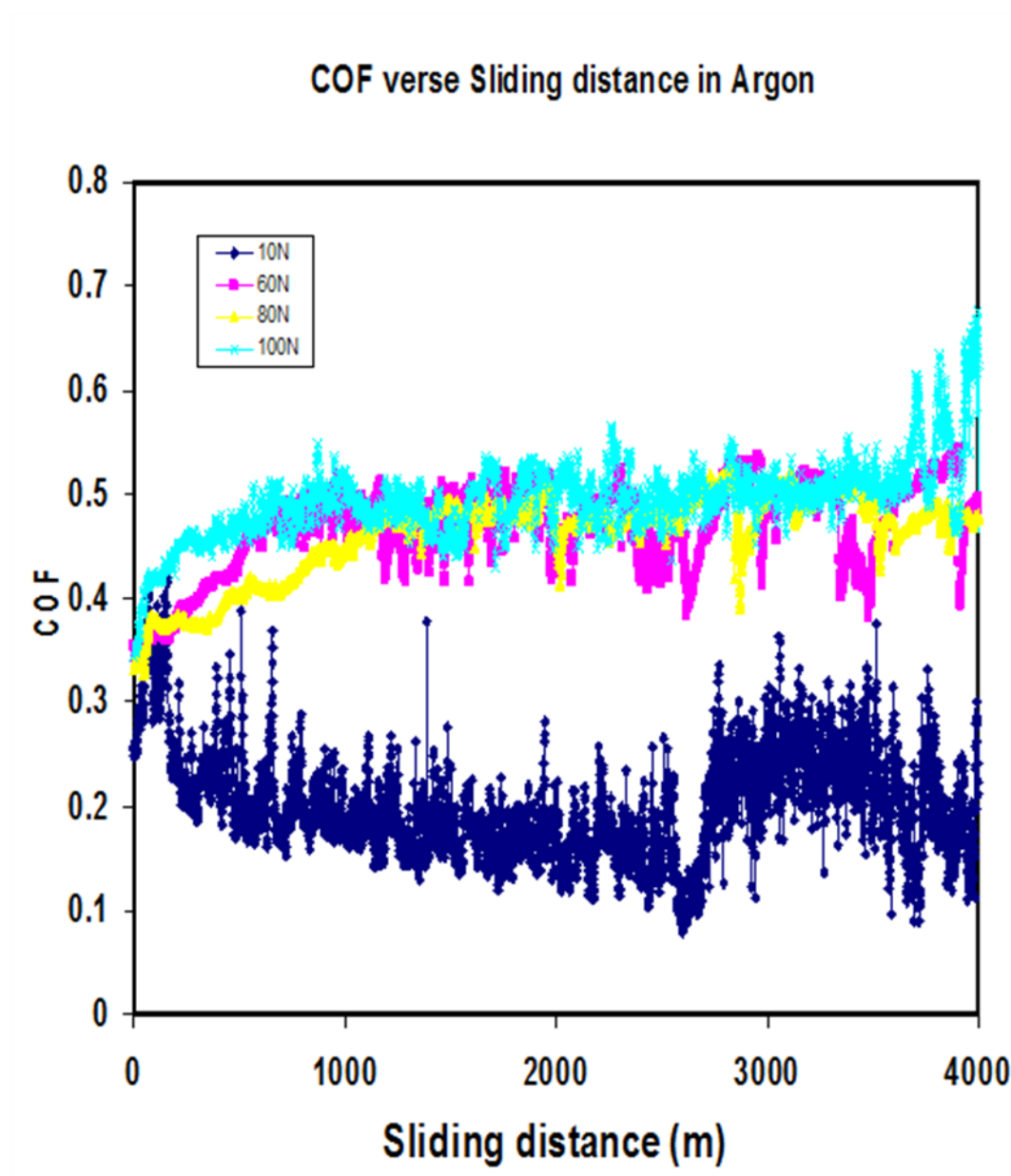


**Fig.5.6** Variation of the coefficient of friction (COF) with the sliding distance at two loads corresponding to mild and severe wear regimes in argon (5% RH): LMW at 10 N, MW at 60N, 80N and SW at 100 N.

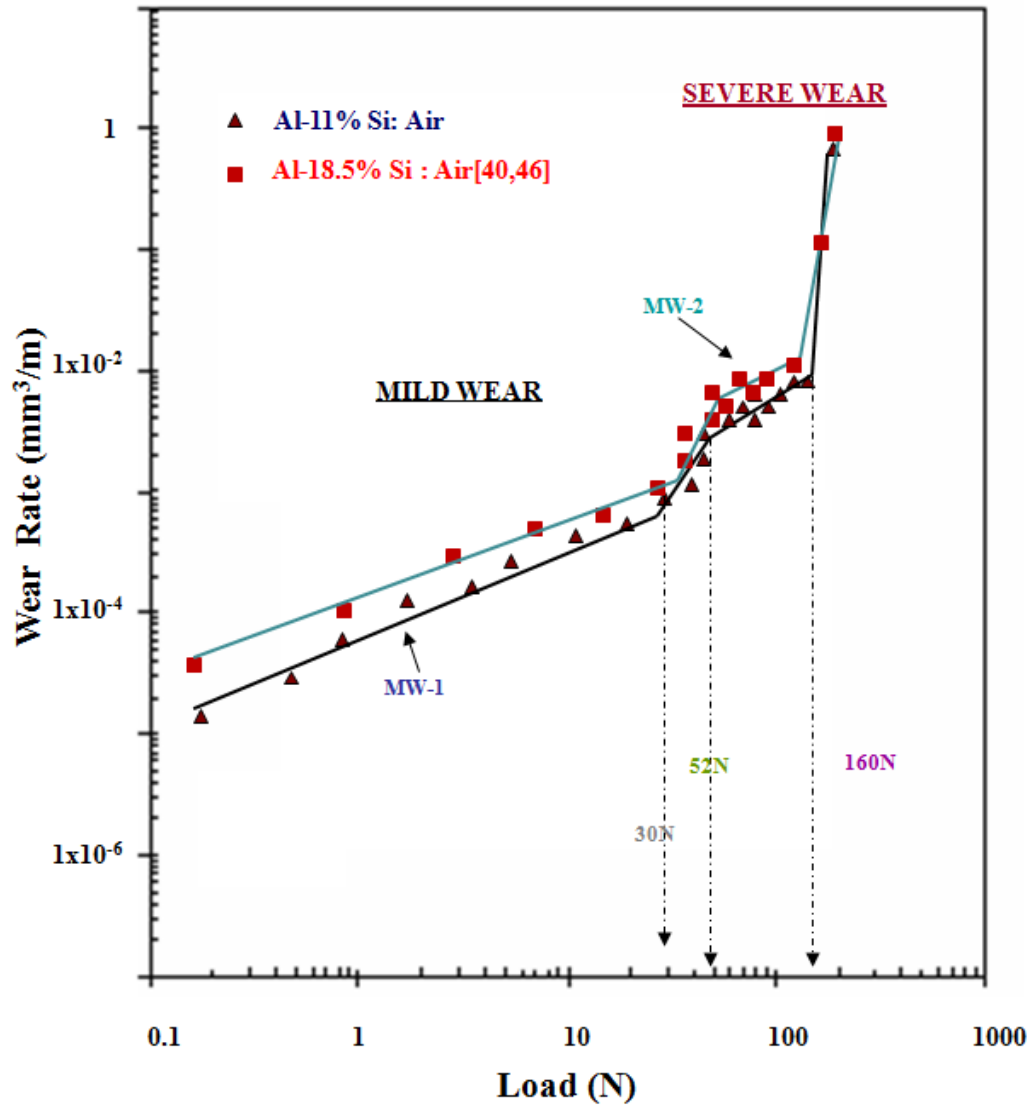


**Fig. 5.7 (a)** Wear regimes and transitions of Al-11% Si alloy with increasing the test load. The tests were conducted at a constant speed of 1 m/s and a sliding distance of  $4 \times 10^3$  m in air (5% RH). MW-1 (at loads below 30 N) and MW-2 (at loads between 52 N and 160 N) are the sub-regimes of mild wear. Severe wear occurred at loads above 160 N.

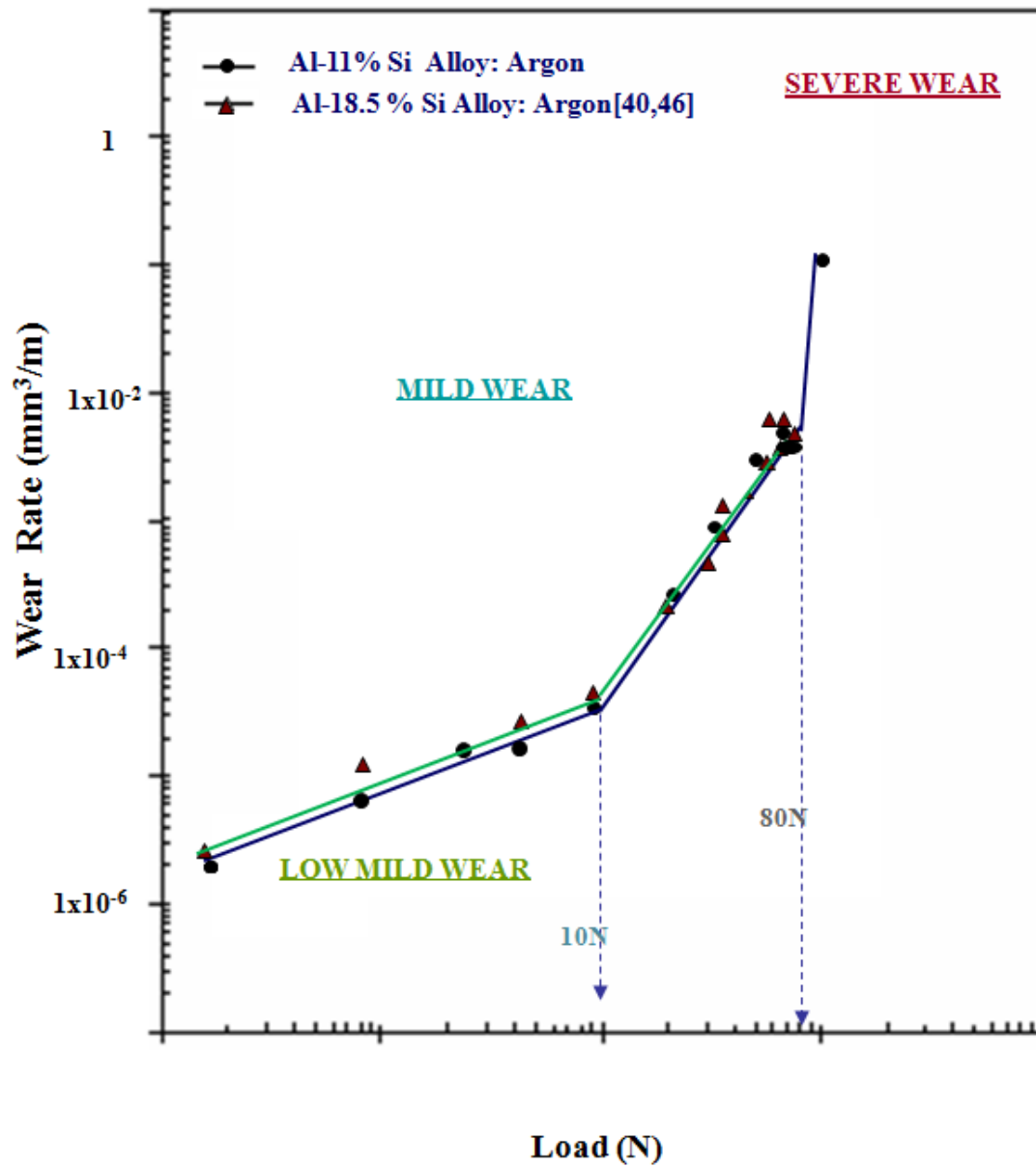
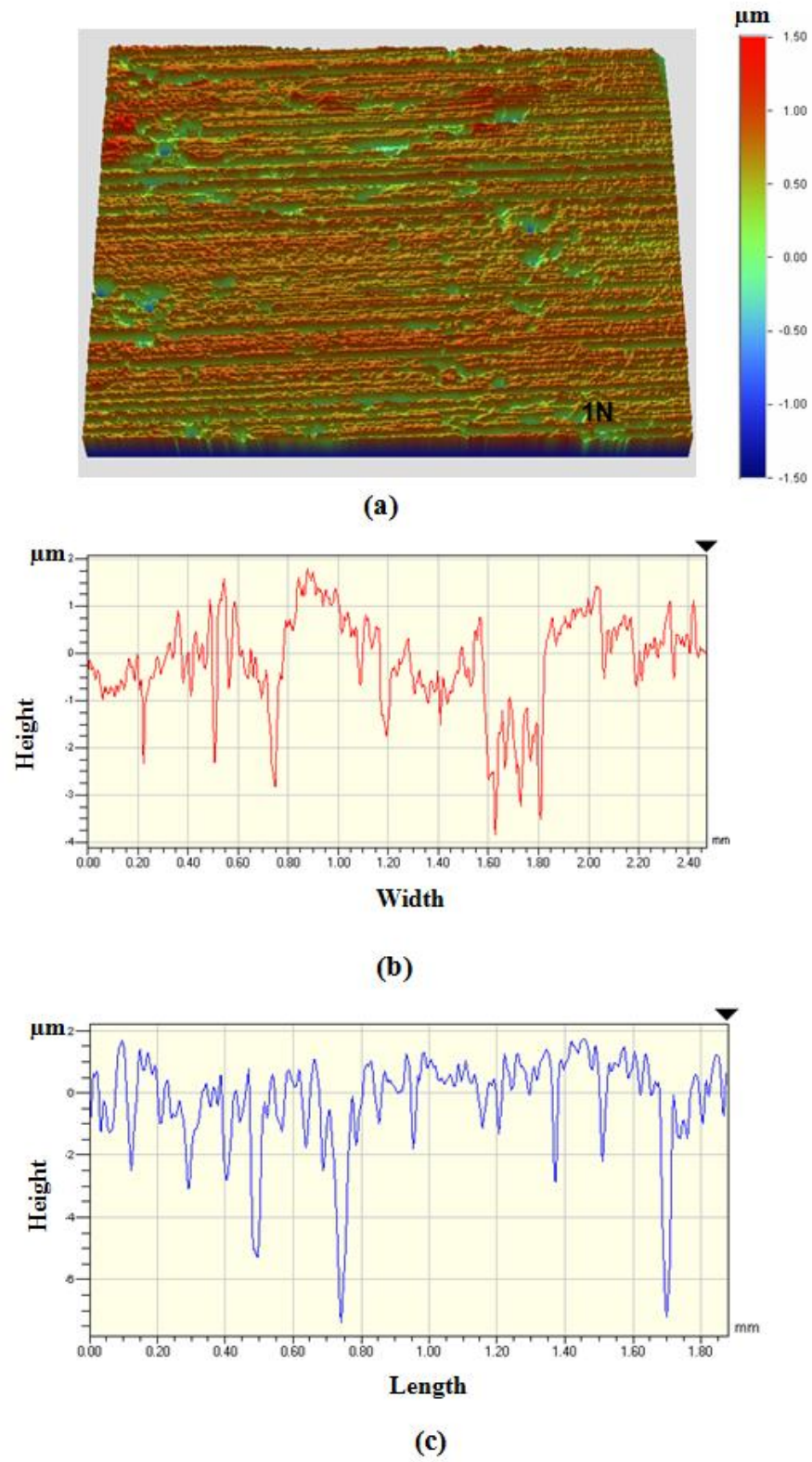
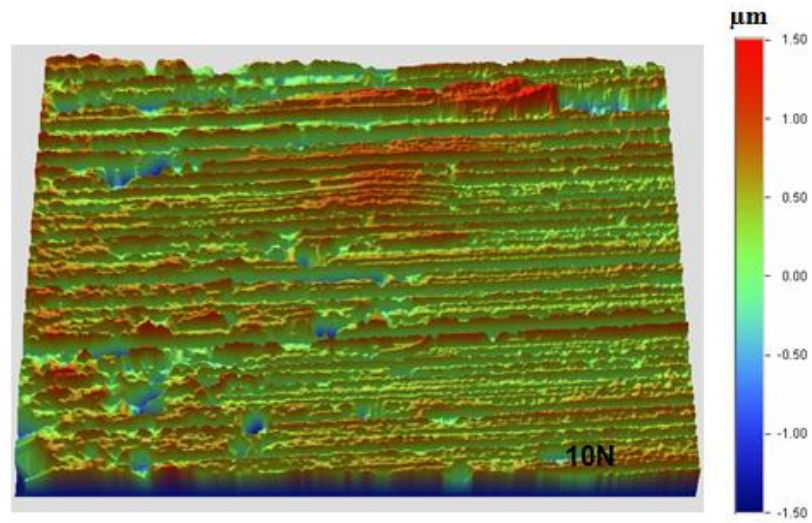


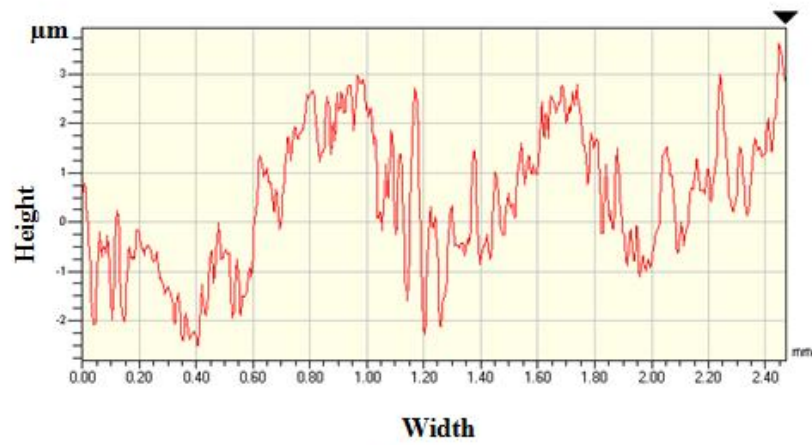
Fig. 5.7(b) Variation of the wear rates with the test load for Al-11% Si tested in an argon atmosphere (5%RH). LMW at loads <10 N, MW between 10N and 80N and SW above 80N.



**Fig.5.8** Pseudo-3D images (a) , X (b) and Y profile (c) of the middle worn surface at the load of 1N in air.



(a)



(b)

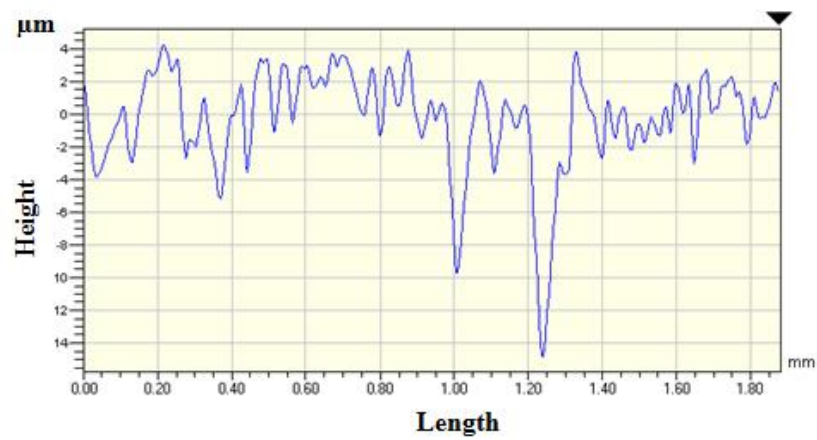


**Fig.5.9** Pseudo-3D images (a) , X ( (b) ) and Y profile (c) of the middle worn surface at the load 10N in air.



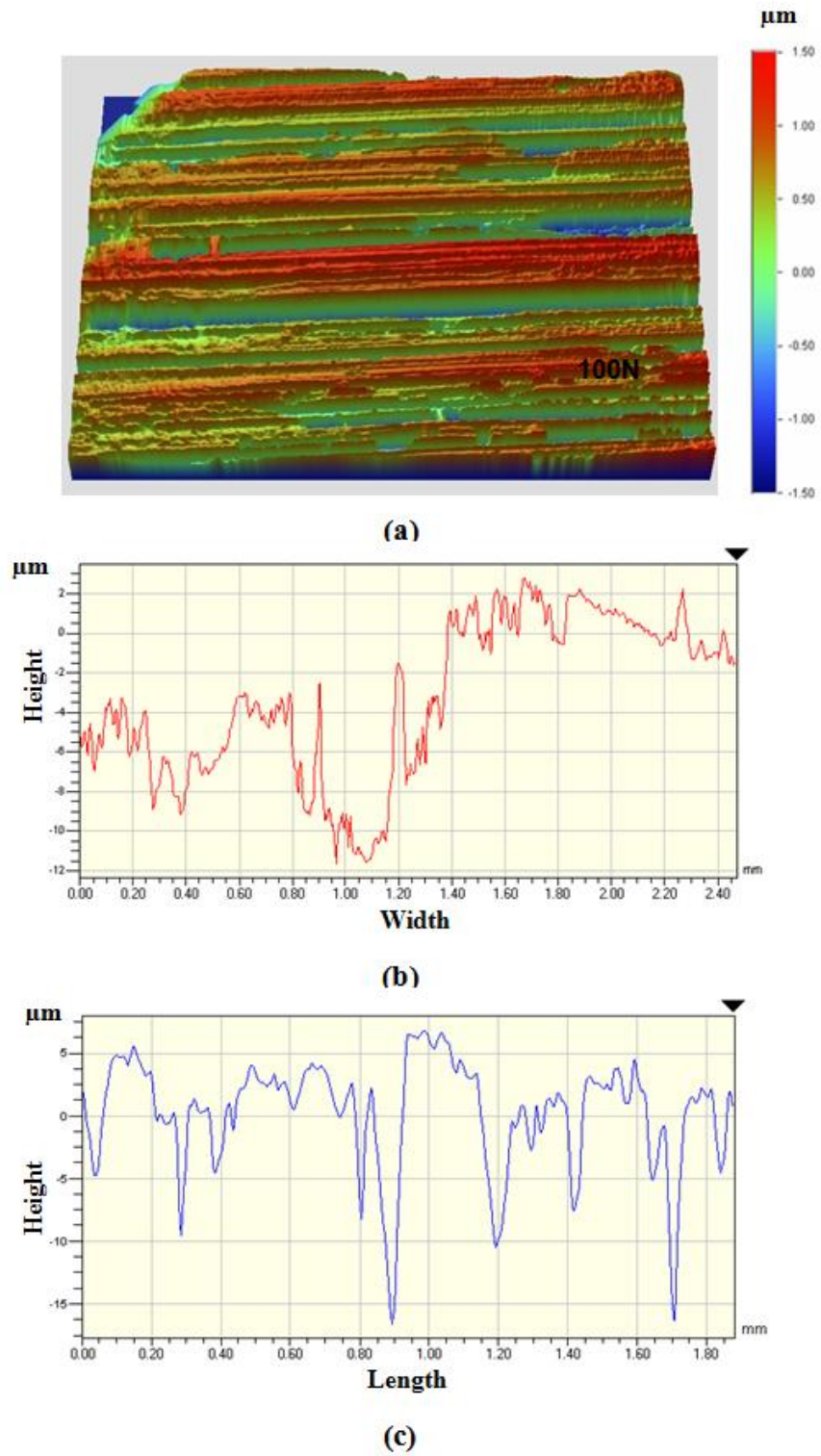
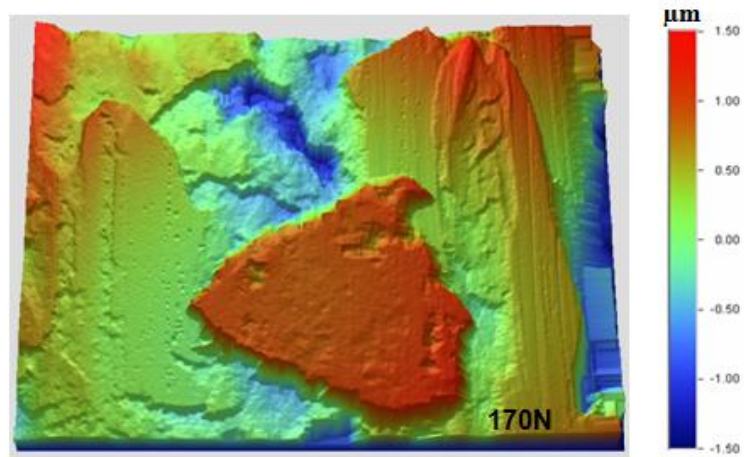


**Fig.5.10** Pseudo-3D images (a) , X (b) and Y profile (c) of the middle worm surface at the load 100N in air.

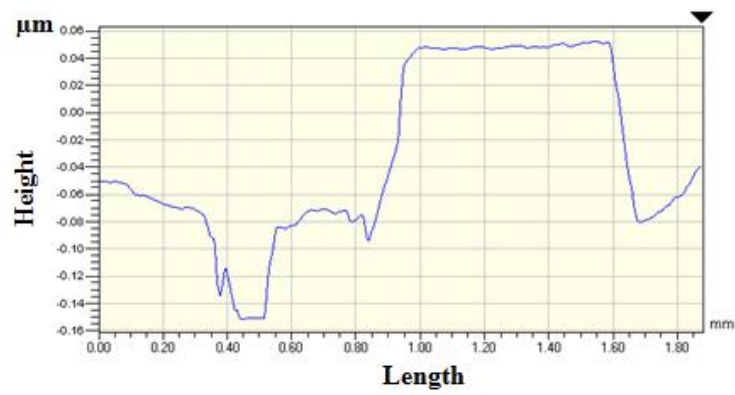




(a)

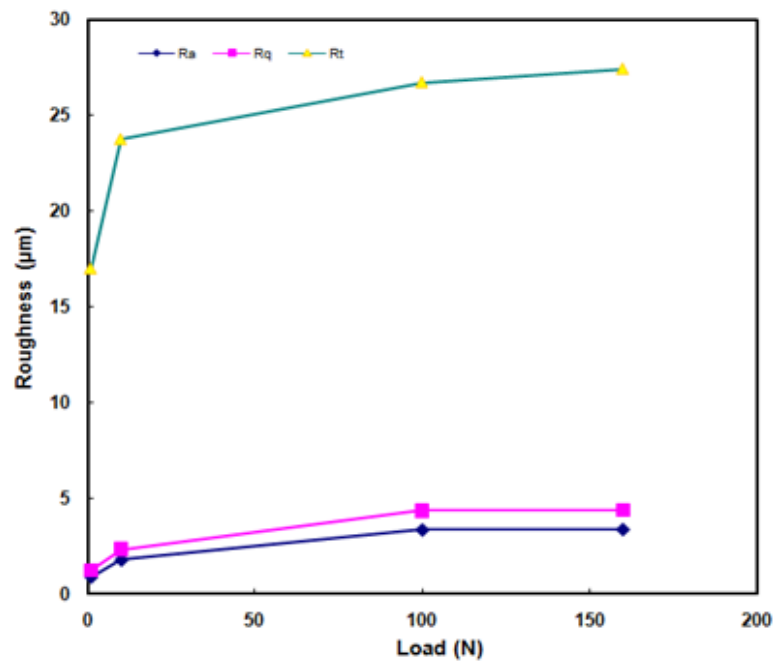


(b)

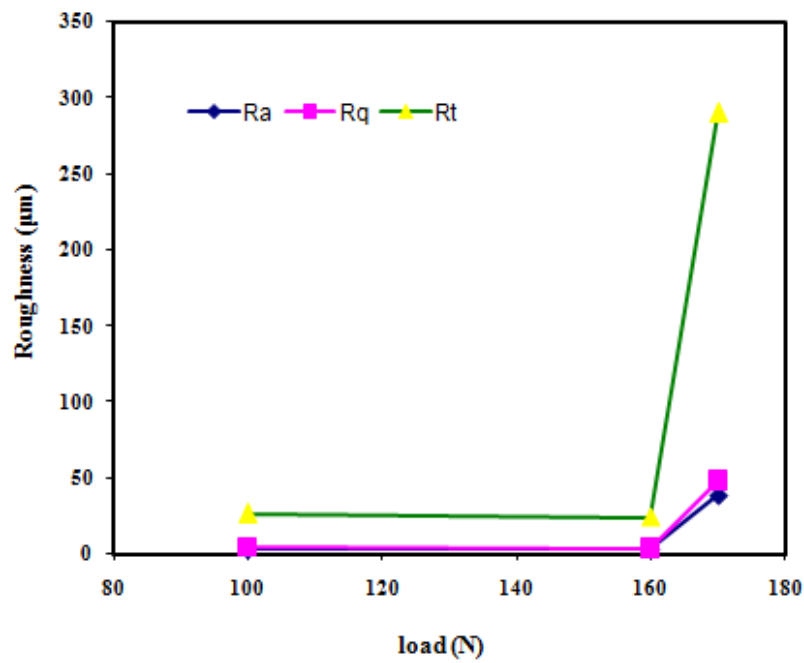


(c)

**Fig.5.11** Pseudo-3D images (a) , X ( (b) and Y profile (c) of the middle worn surface at the load 170N in air.

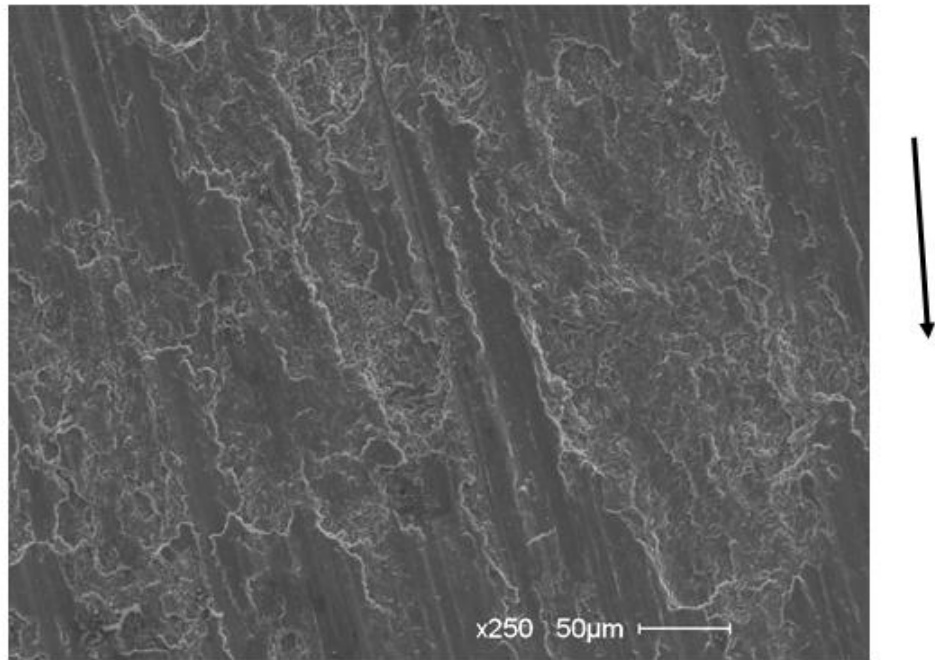


(a)



(b)

**Fig.5.12** Variations of worn surface roughness with load in air (a) in mild wear regime (b) transition from mild wear to severe wear.



(a)

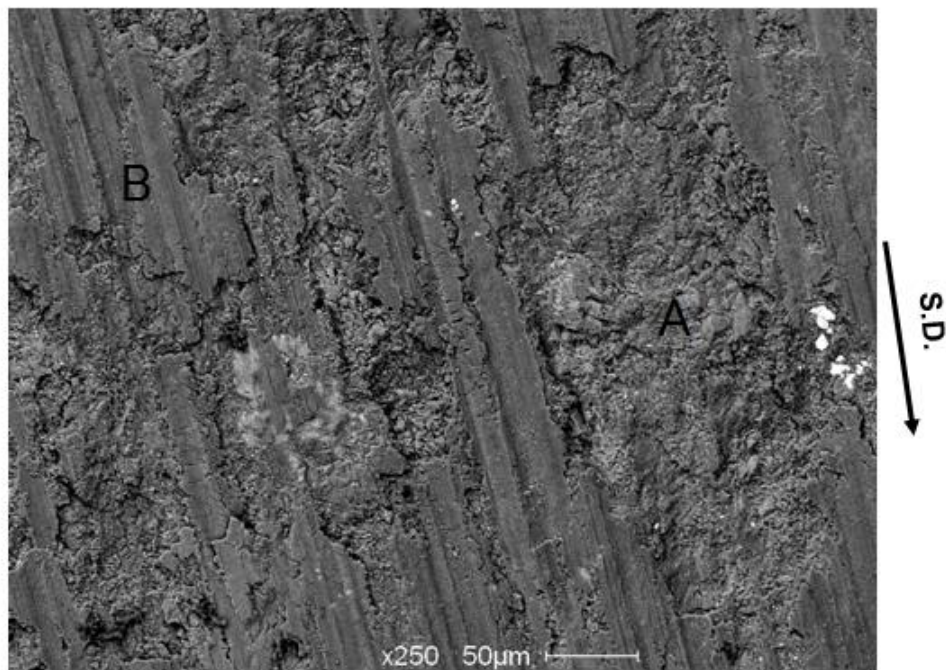


**Fig.5.13.** (a) A low magnification secondary SEM micrograph of the worn surface of an Al-11% Si alloy sample in the mild wear regime at 5 N (MW-1) after 4000 m. (b) Back-scattered SEM micrograph of the same area.

S.D.

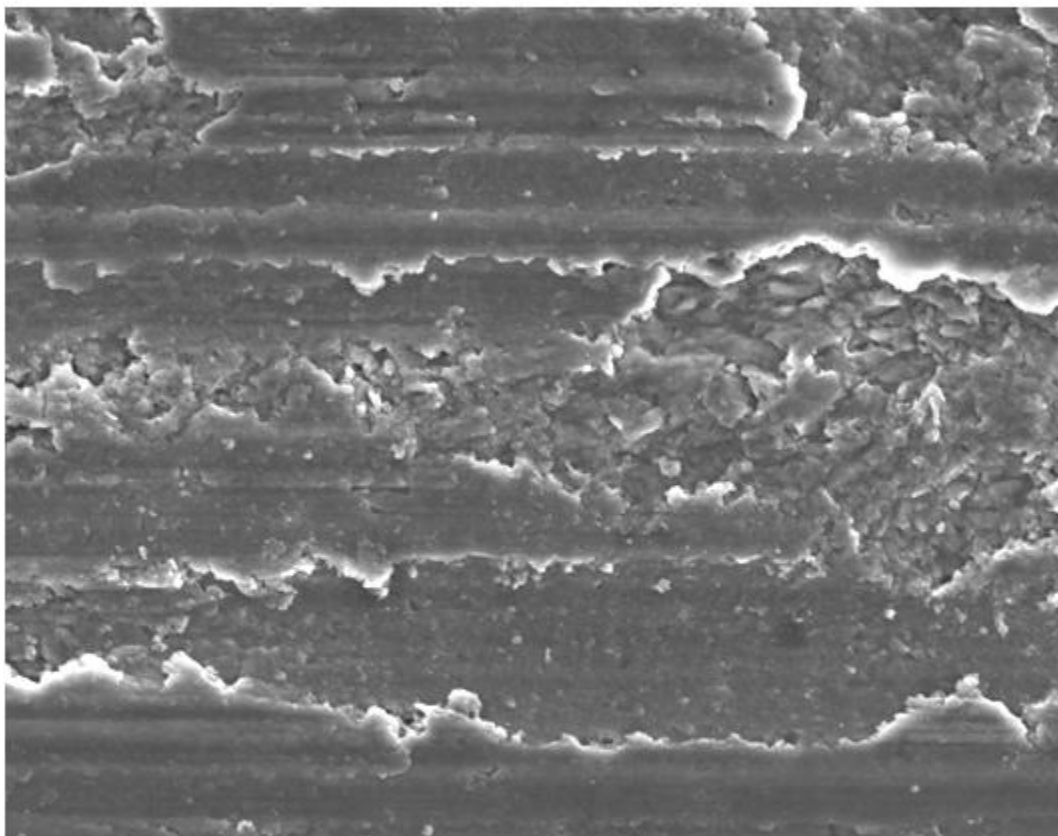
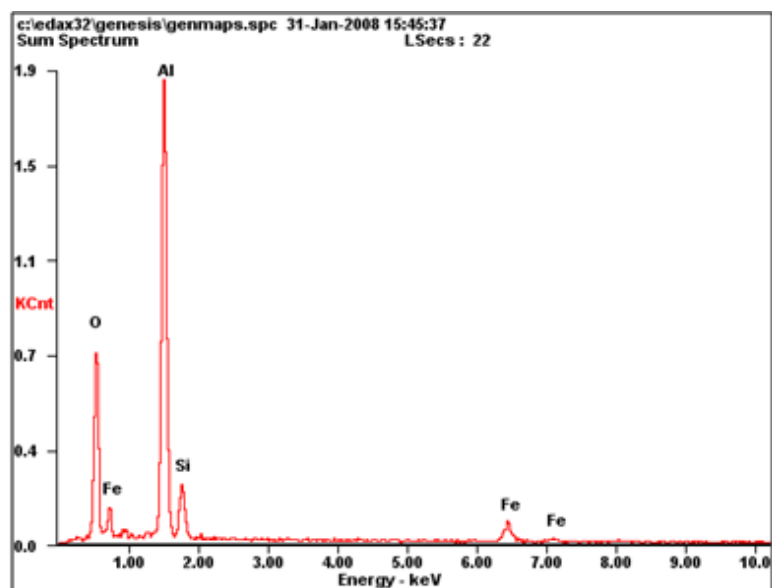
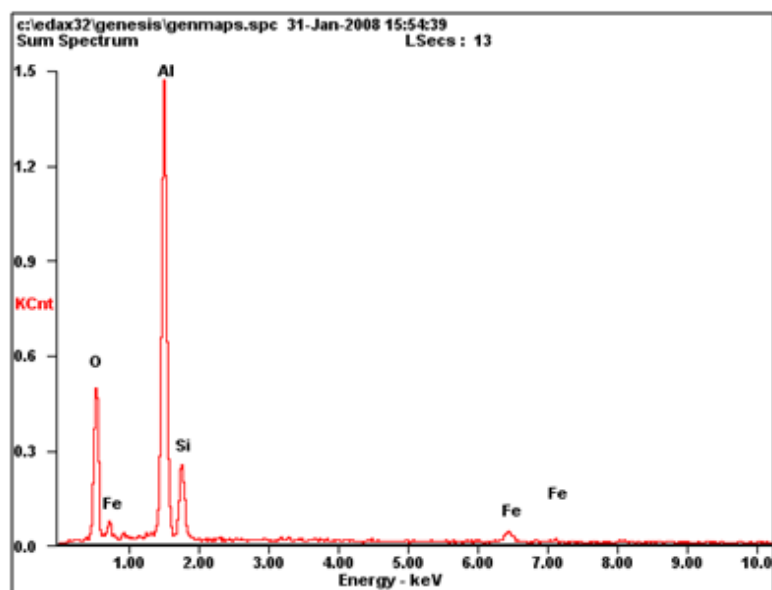


**Fig.5.14.** SEM micrograph of crater area in the worn surface at a load of 5N, showing equiaxed particles in the crater.



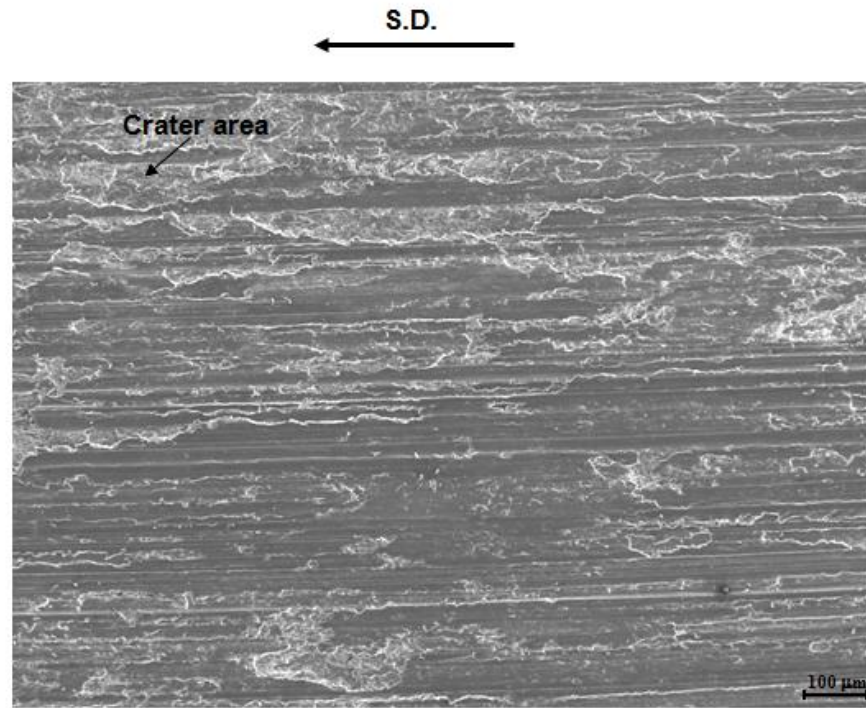
(a)



(b)

**Fig.5.15 (a)** The EDS spectrum of the regions marked as A (a) and B (b) are shown in Fig.5.13 respectively, indicating the formation of Fe rich oxidized tribolayer.





(a)

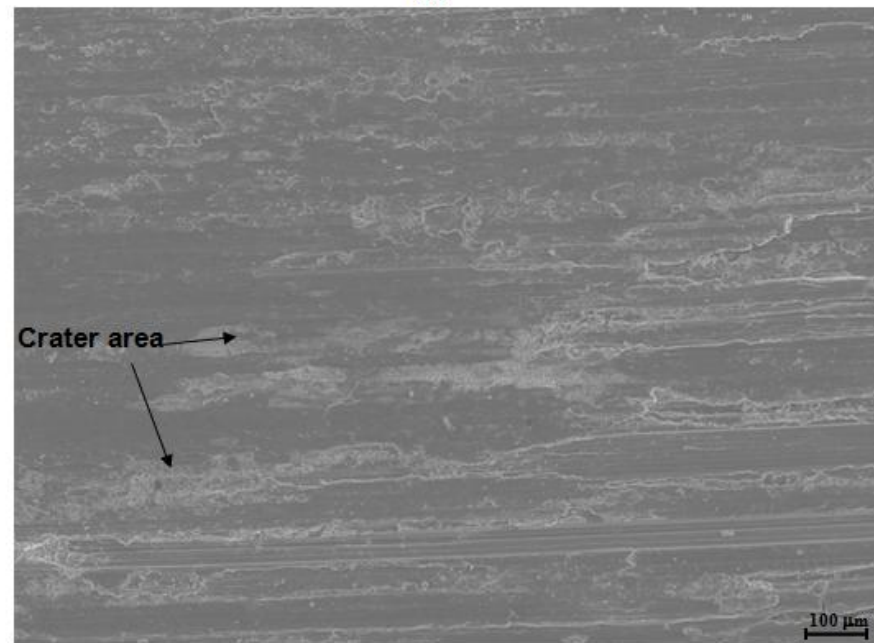
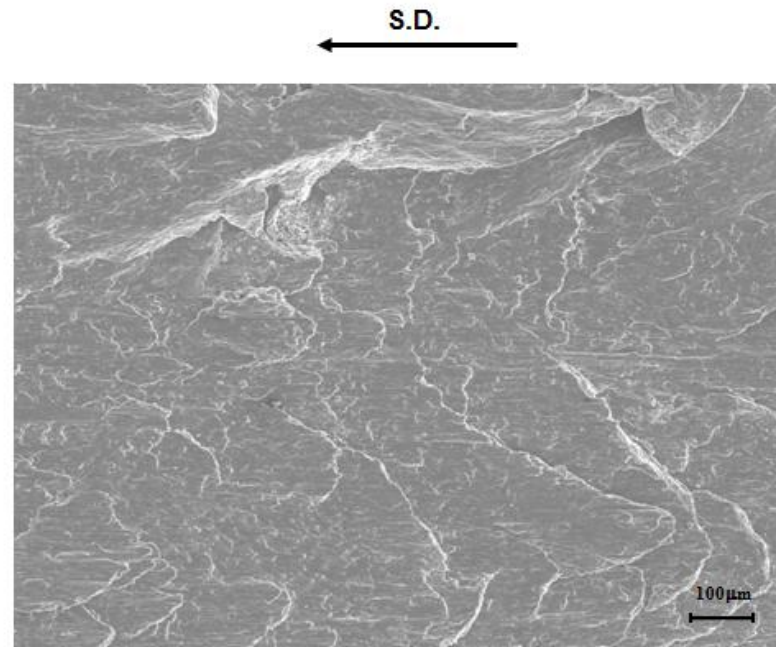
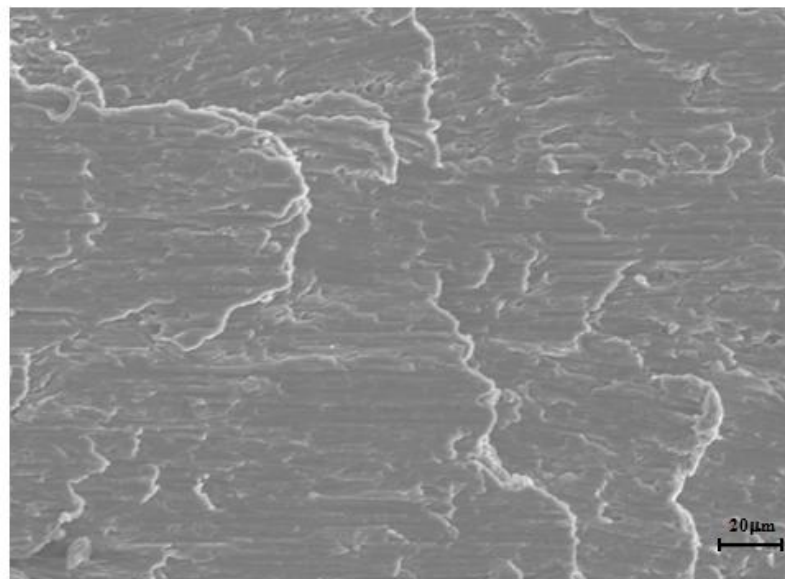


**Fig.5.16.** Secondary SEM micrograph of the worn surface of Al-11% Si Alloy sample at 10N (a) and 100N (b) after 4000 m tests.

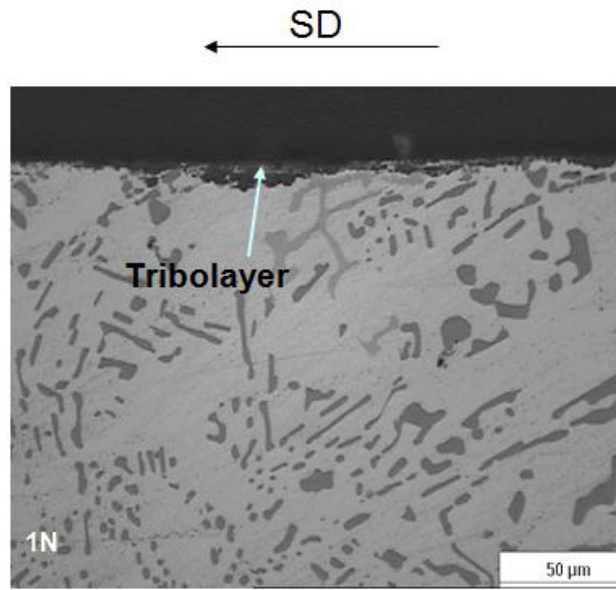


(a)

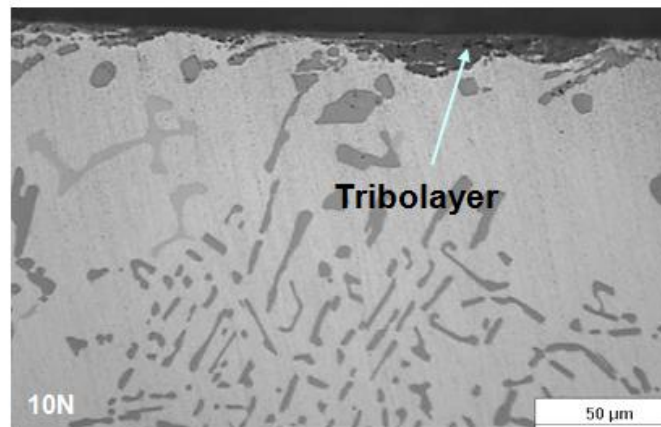


(b)

**Fig.5.17** Secondary SEM micrograph of the worn surface of 1Al-11% Si Alloy sample at 170N after 2000 m with low (a) and high (b)magnifications .



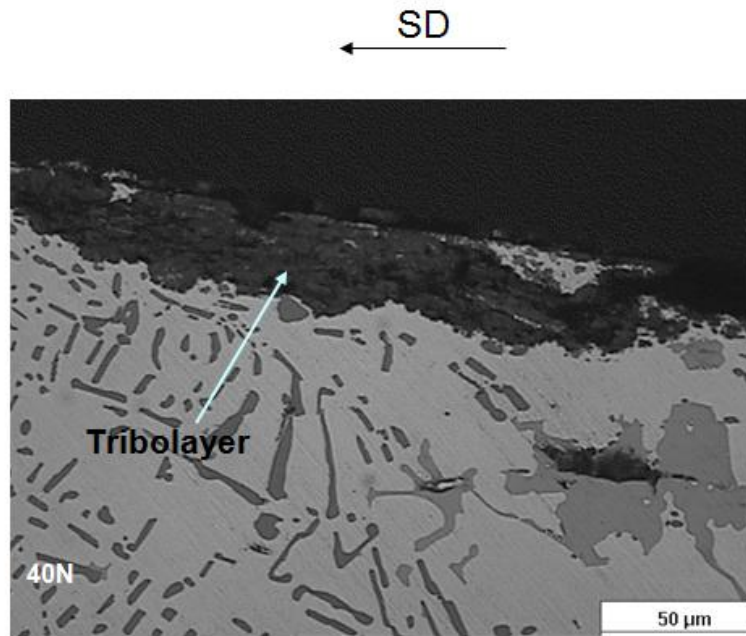
(a)



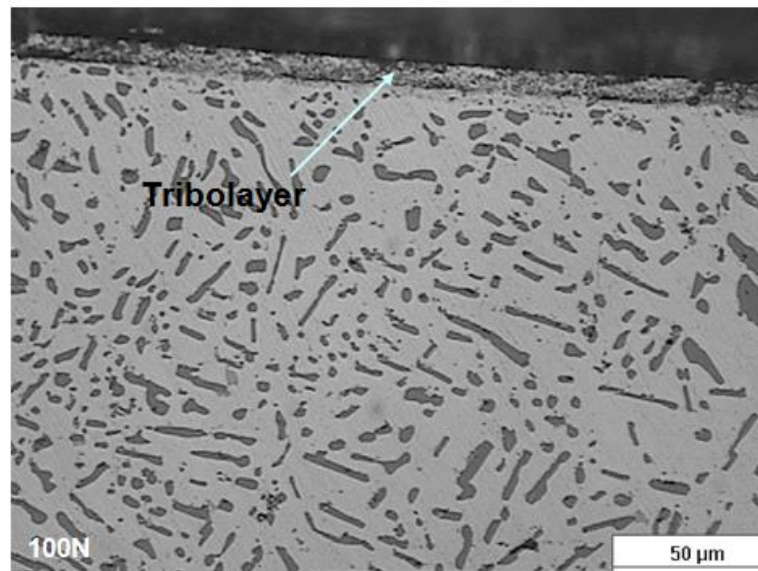
(b)

**Fig. 5.18** Cross-sectional optical micrographs showing the tribolayers in mild wear in air (a) 1N, (b) 10N, (c) 40N and ( d ) 100N.





(c)



(d)

**Fig. 5.18 Continued** Cross-sectional optical micrographs showing the tribolayers in mild wear in air (a) 1N, (b) 10N, (c) 40N and ( d ) 100N.

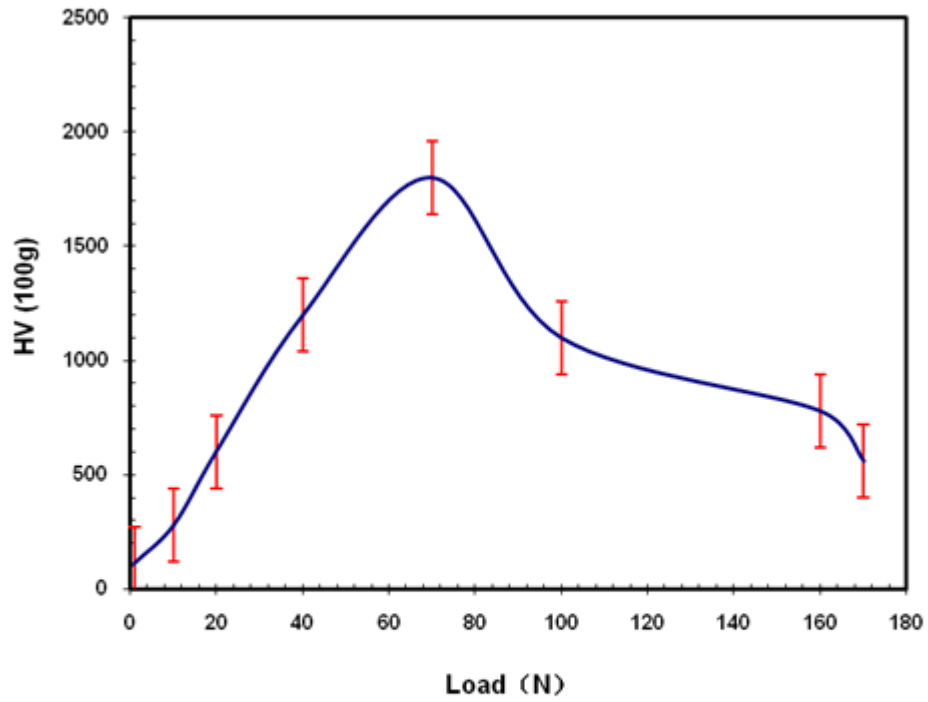
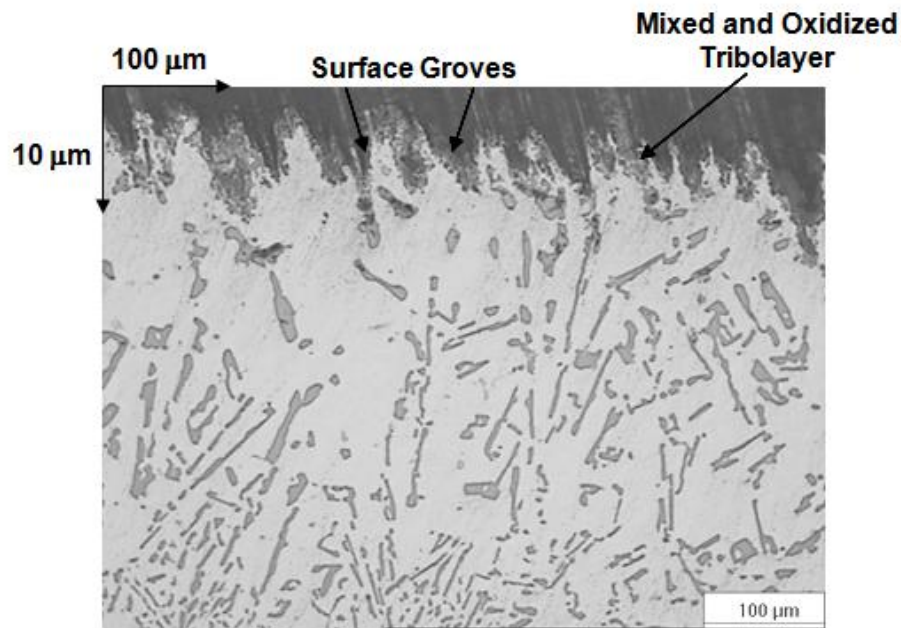
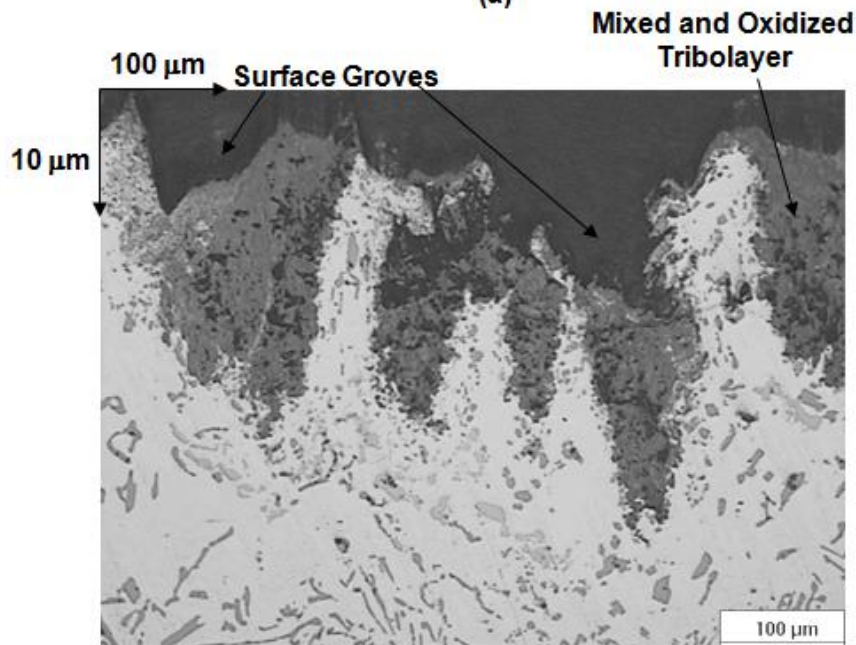


**Fig.5.19** Worn surface microhardness variation with load for the Al-11% Si alloy (Vickers indenter, 100gf).

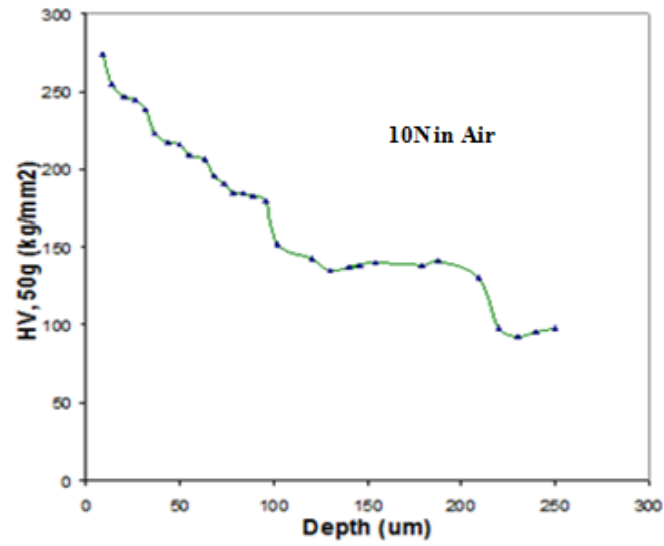


(a)

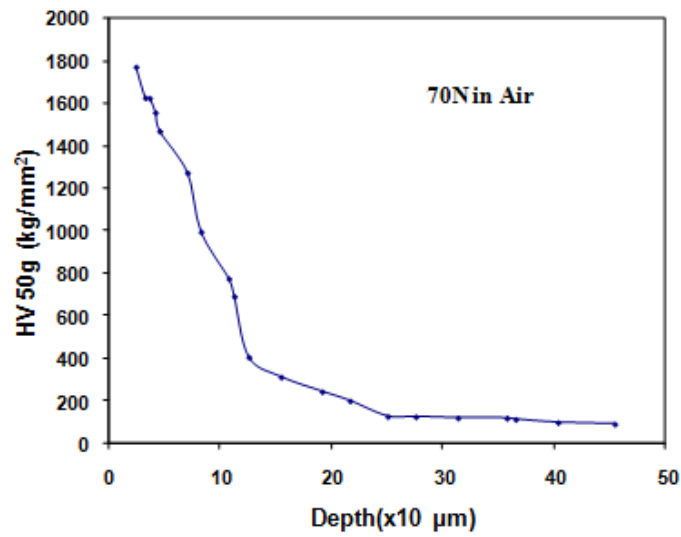


(b)

**Fig. 5.20** Subsurface optical micrographs of Al-11% Si alloy taken from the tapered sections cut at angle of  $5.7^\circ$  to the contact surfaces at loads of (a) 10 N and (b) 70 N in air (5% RH). The micrographs showed deeper and wider surface grooves, and a thicker mixed and oxidized tribolayer in MW-2 compared to MW-1.

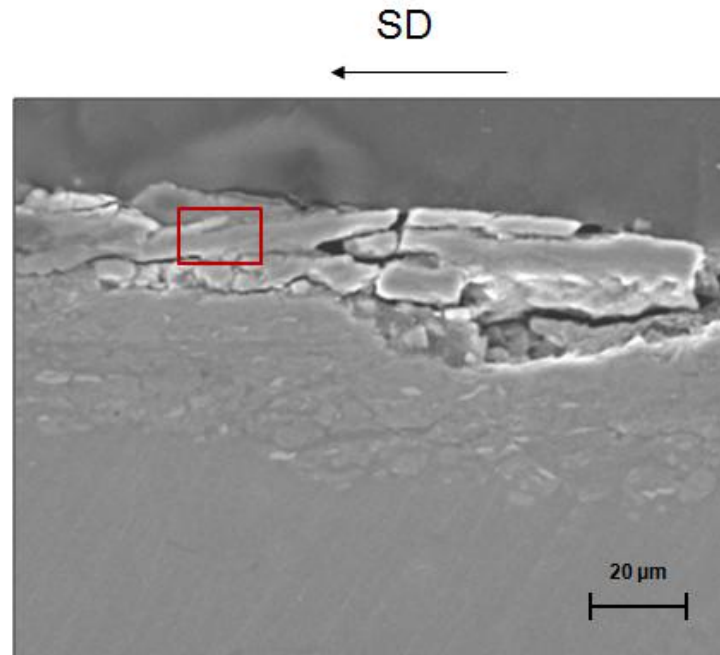


(a)

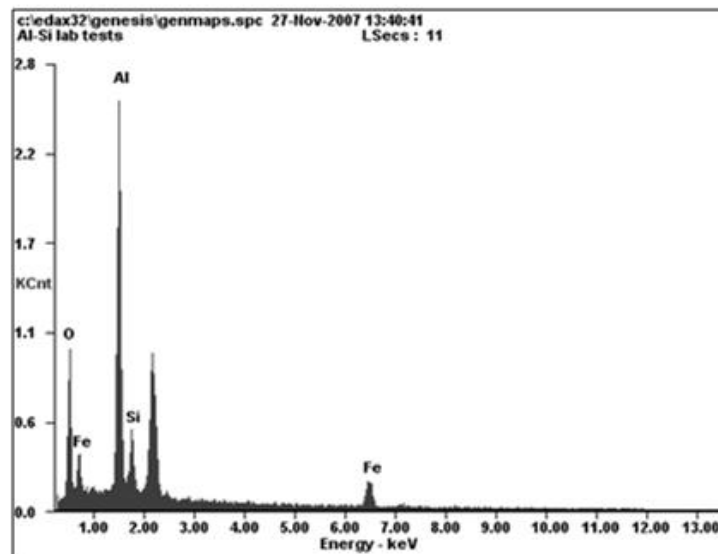


(b)

**Fig. 5.21** Subsurface microhardness (HV, 50g) profile at load of 10N (a) and 70N (b) in air after a sliding distance of 4000m. Microhardness measurements were performed on transverse tapered sections (cut at an angle of  $5.7^\circ$  to worn surface).

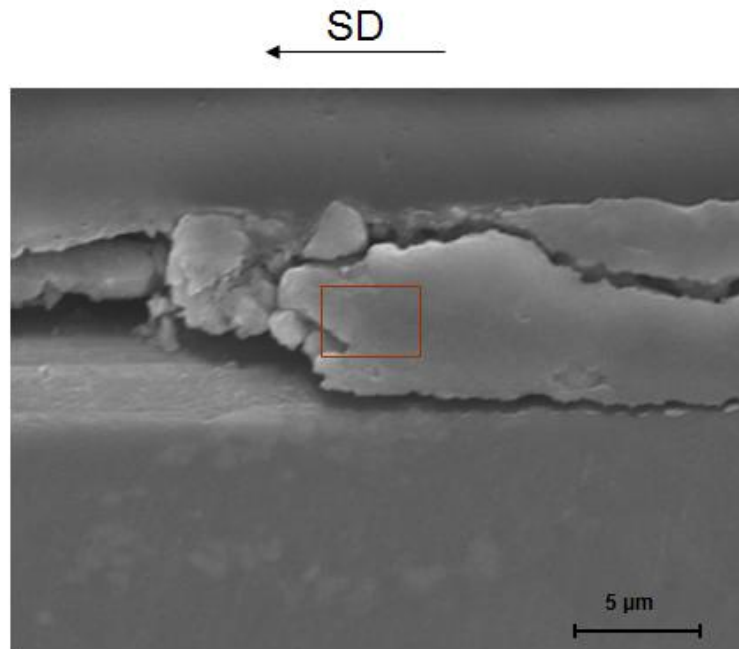


(a)

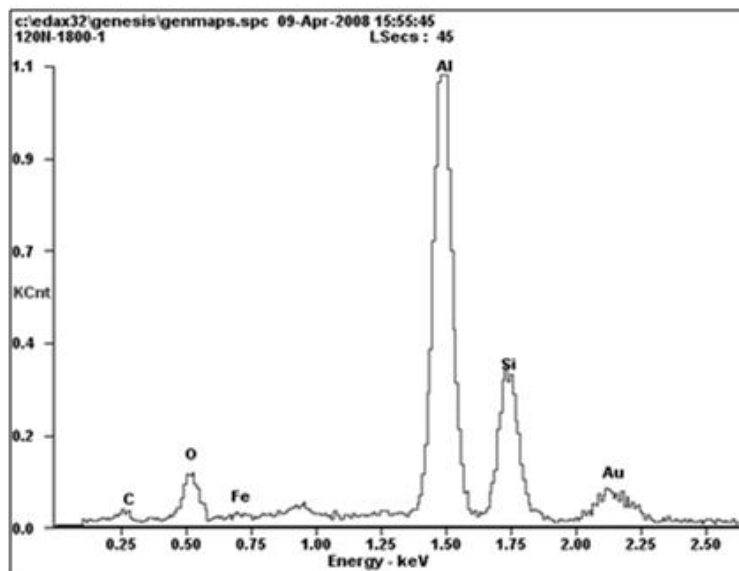


(b)

**Fig.5.22** The secondary SEM micrograph given in (a) shows worn subsurface morphology of the Al-11% Si alloy at 40 N in air (5% RH) and evidence for removal of the tribolayers by delamination, as shown by the portion of the tribolayer which was about to be removed., (b) the EDS spectrum of the regions marked indicating the formation of Fe rich oxidized tribolayer at 40N .



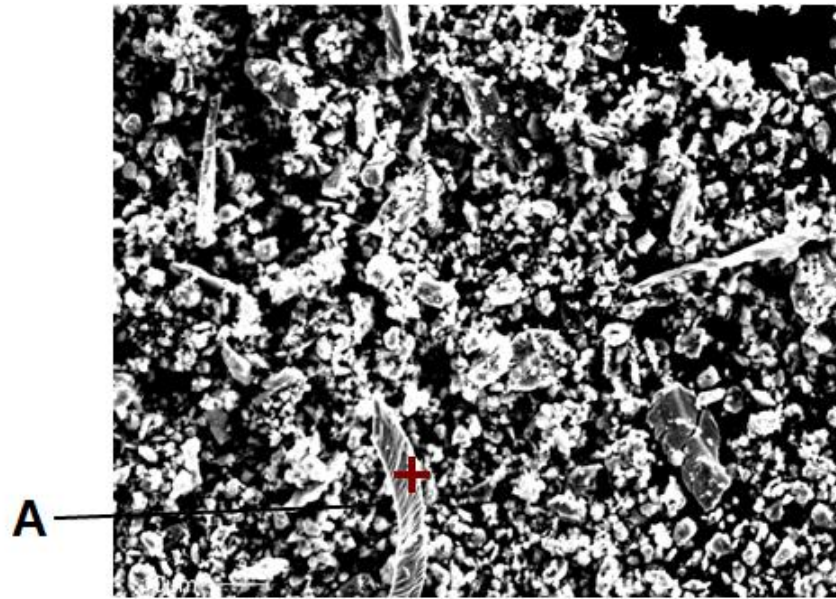
(a)



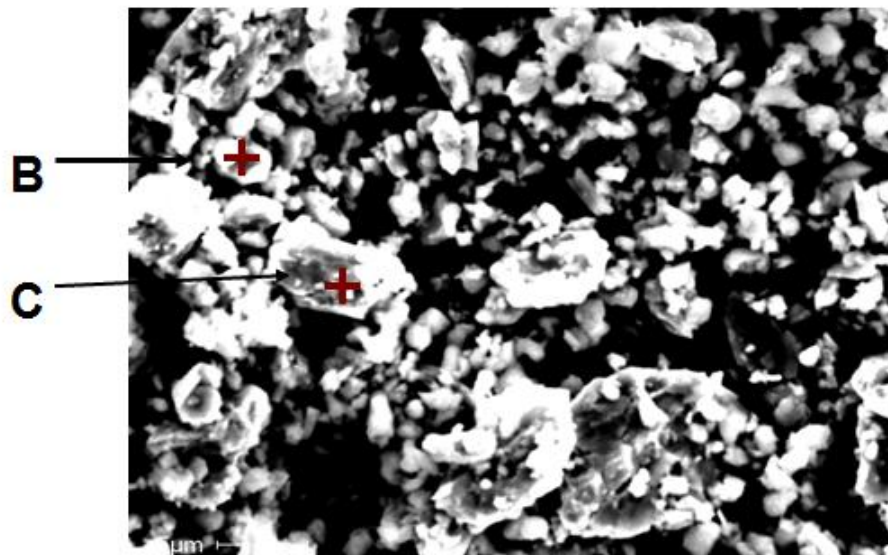
(b)

**Fig.5.23** The secondary SEM micrograph given in (a) shows worn subsurface morphology of the Al-11% Si alloy at 100 N in air (5% RH) and evidence for removal of the tribolayers by spallation, (b) the EDS spectrum of the regions marked indicating the formation of tribolayer at 100N .



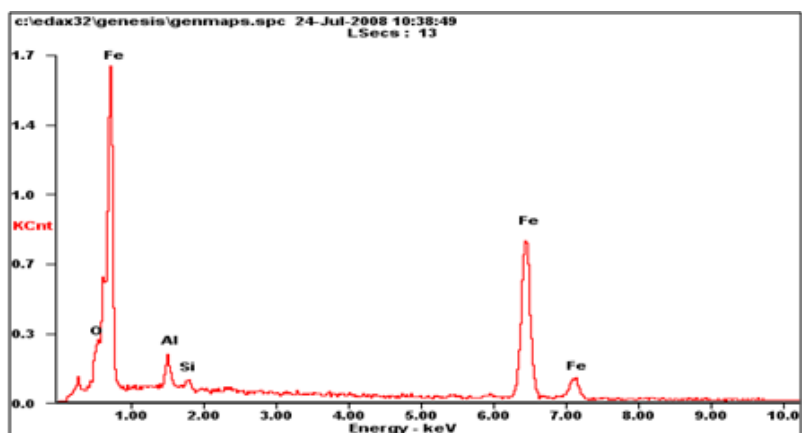


(a)

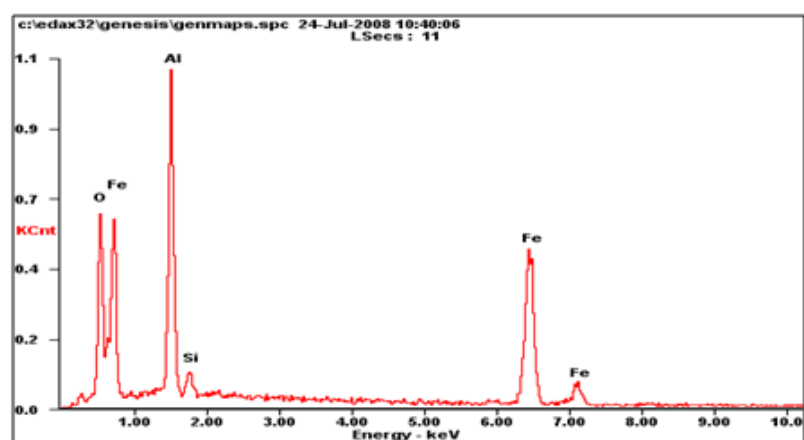


(b)

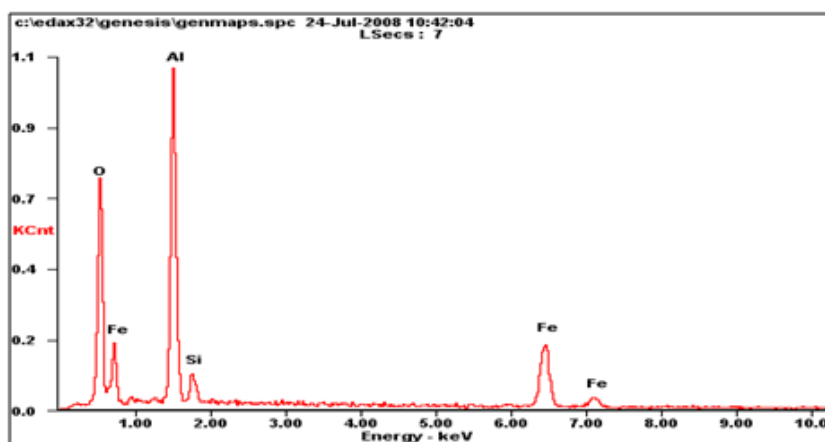
**Fig. 5.24** SEM micrograph showing two magnification views of the wear debris produced at 20 N in air (5% RH). (a) The micrograph indicates that the debris was mainly composed of fine particles, but plate-like and ribbon shaped particles were also observed. (b) A high magnification secondary SEM micrograph of the fine particle debris.



(a)



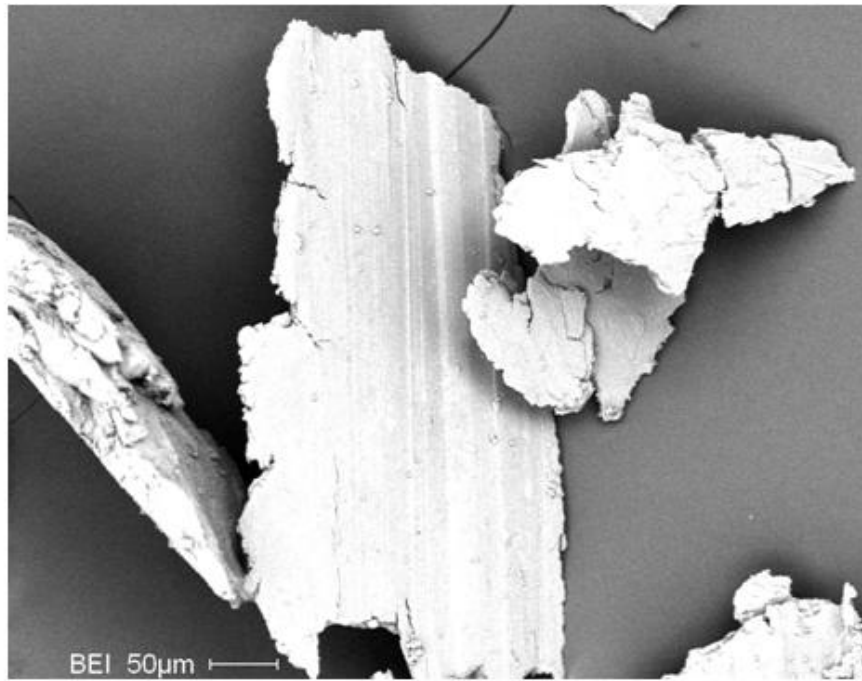
(b)



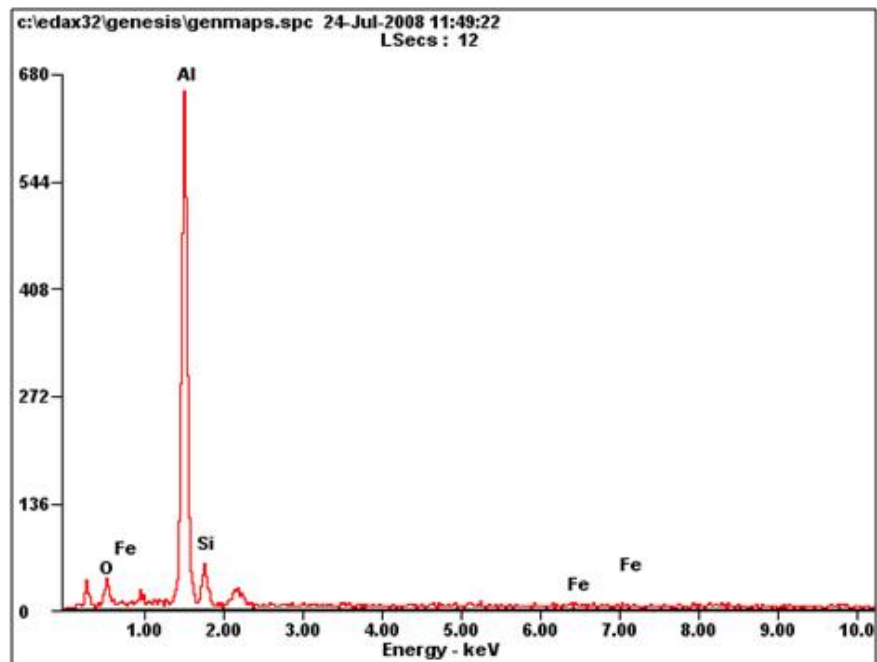
(c)

Fig. 5.25 EDS spectra of the debris produced at 15N from the regions marked as A, B and C in Fig. 5.24: (a) ribbon shaped Fe chips (A), (b) fine particles (B) and (c) large particles (C)



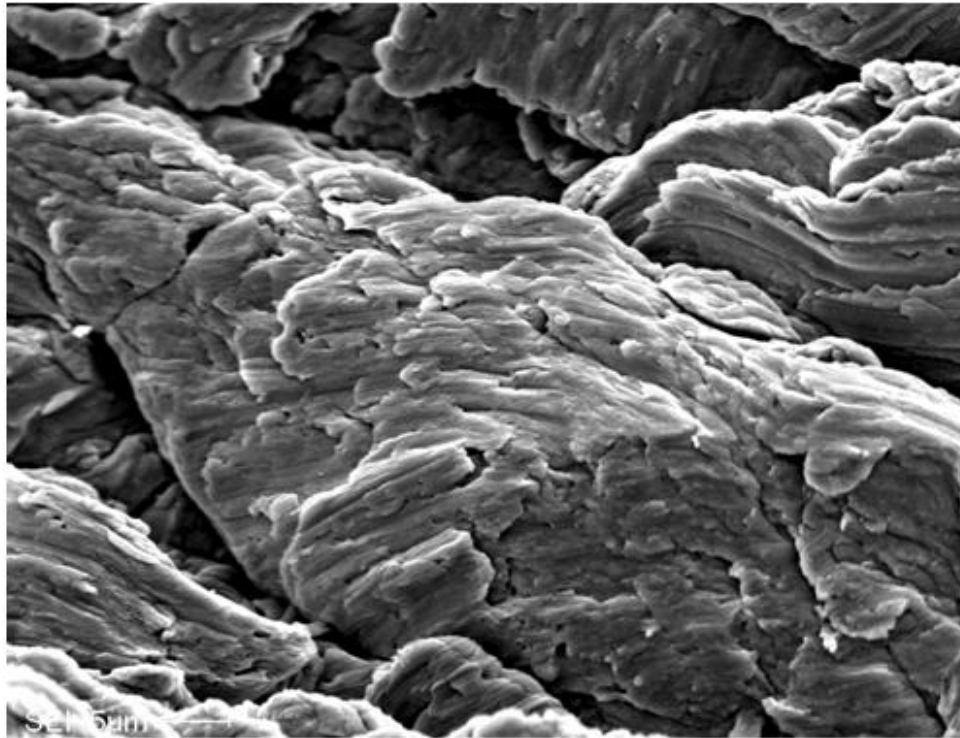


(a)

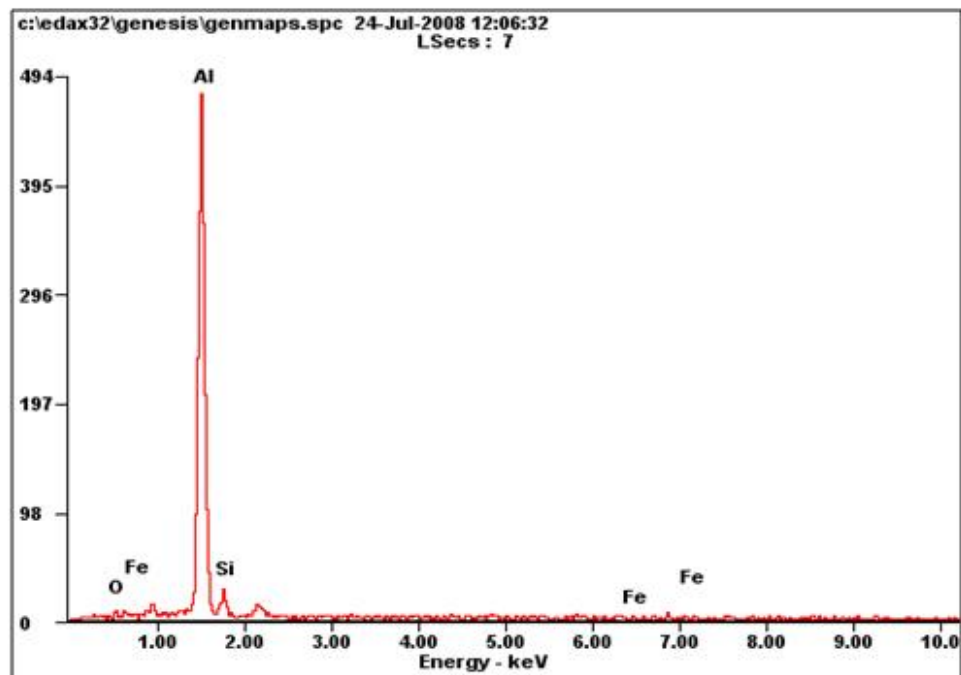


(b)

**Fig. 5.26** SEM (a) and EDS (b) spectrums of the debris produced at 70N from the debris particles showing that they were rich in Al content with small amounts of Fe and O.

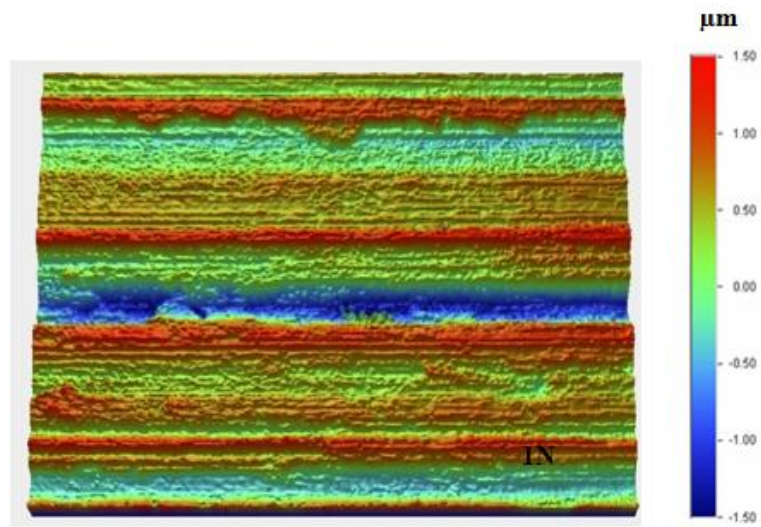


(a)

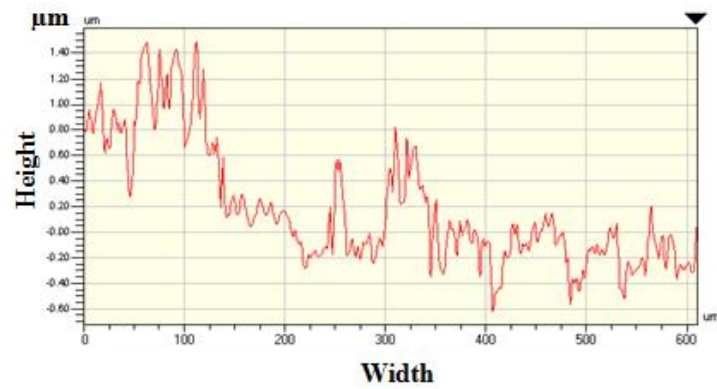


(b)

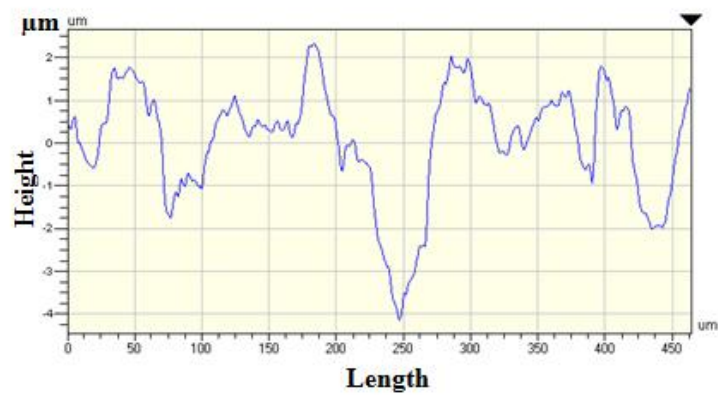
**Fig. 5.27** SEM (a) and EDS (b) spectrums of the debris produced at 170N from the debris particles showing that their chemical compositions were similar to that of unworn Al-Si samples.



(a)

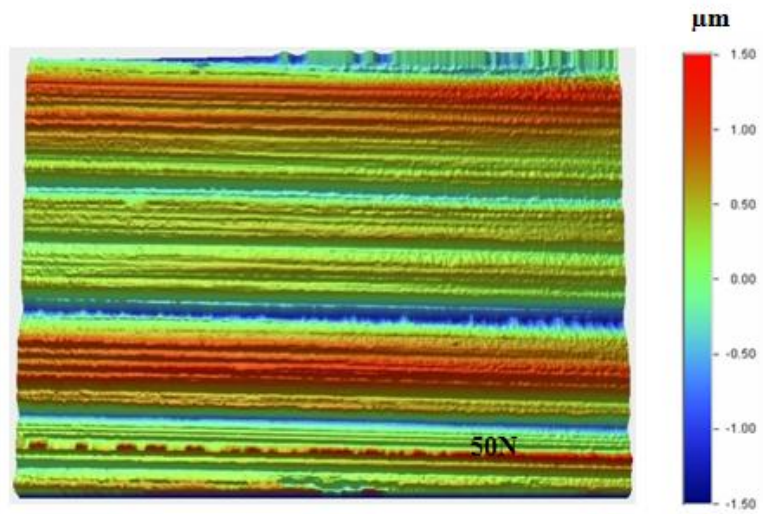


(b)



(c)

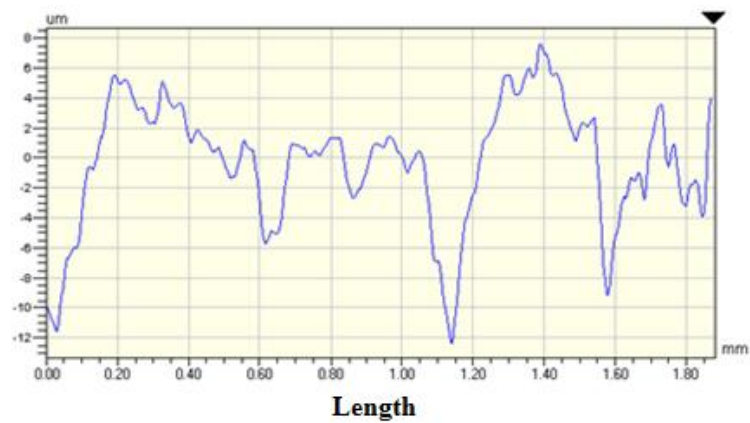
**Fig.5.28** Pseudo-3D images (a) , X (b) and Y profile (c) of the middle worm surface at the load 1N in argon.



(a)



(b)



(c)

**Fig.5.29** Pseudo-3D images (a) , X (b) and Y profile (c) of the middle worn surface at the load 50N in air.



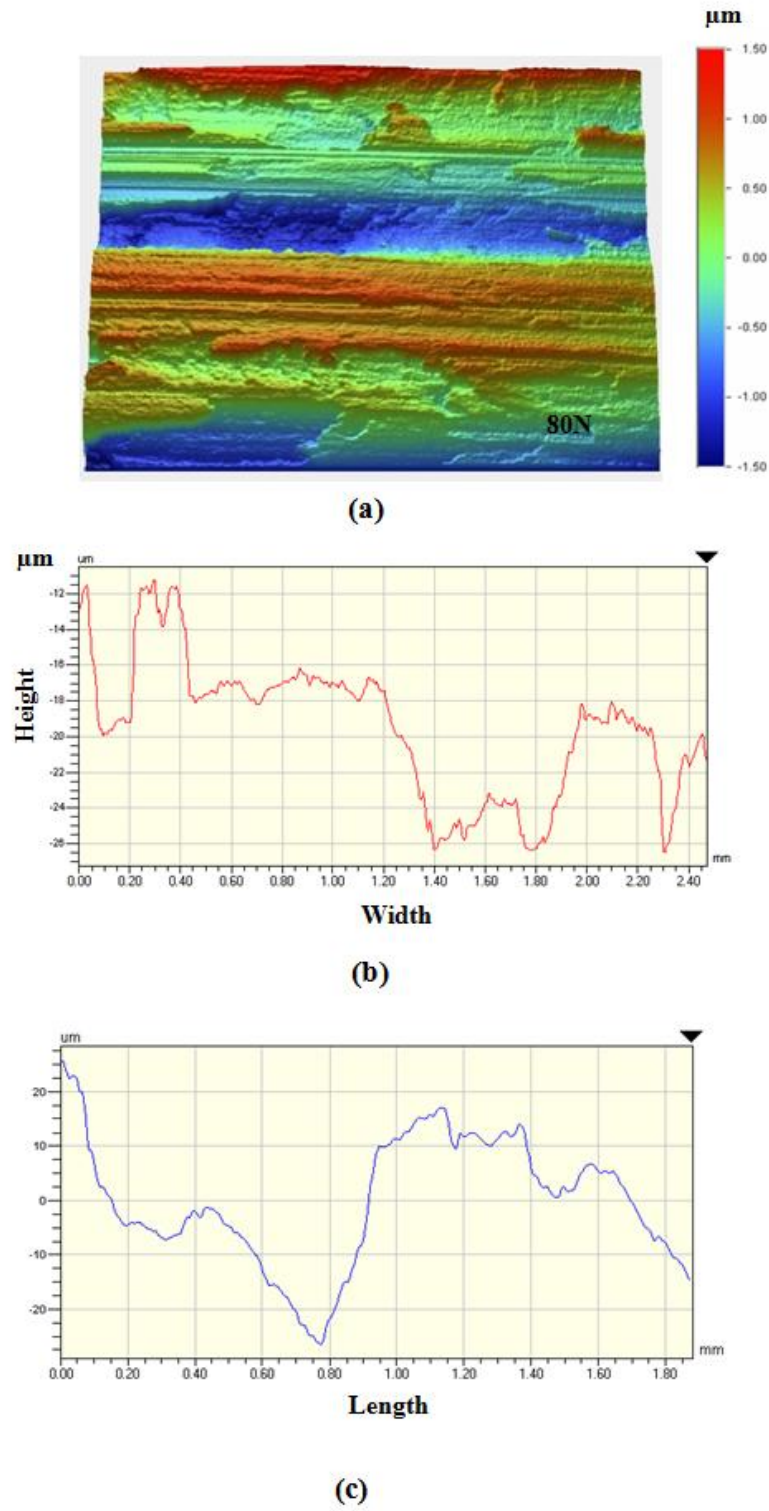


**Fig.5.30** Pseudo-3D images (a) , X ( b) and Y profile (c) of the middle worm surface at the load 80N in argon.

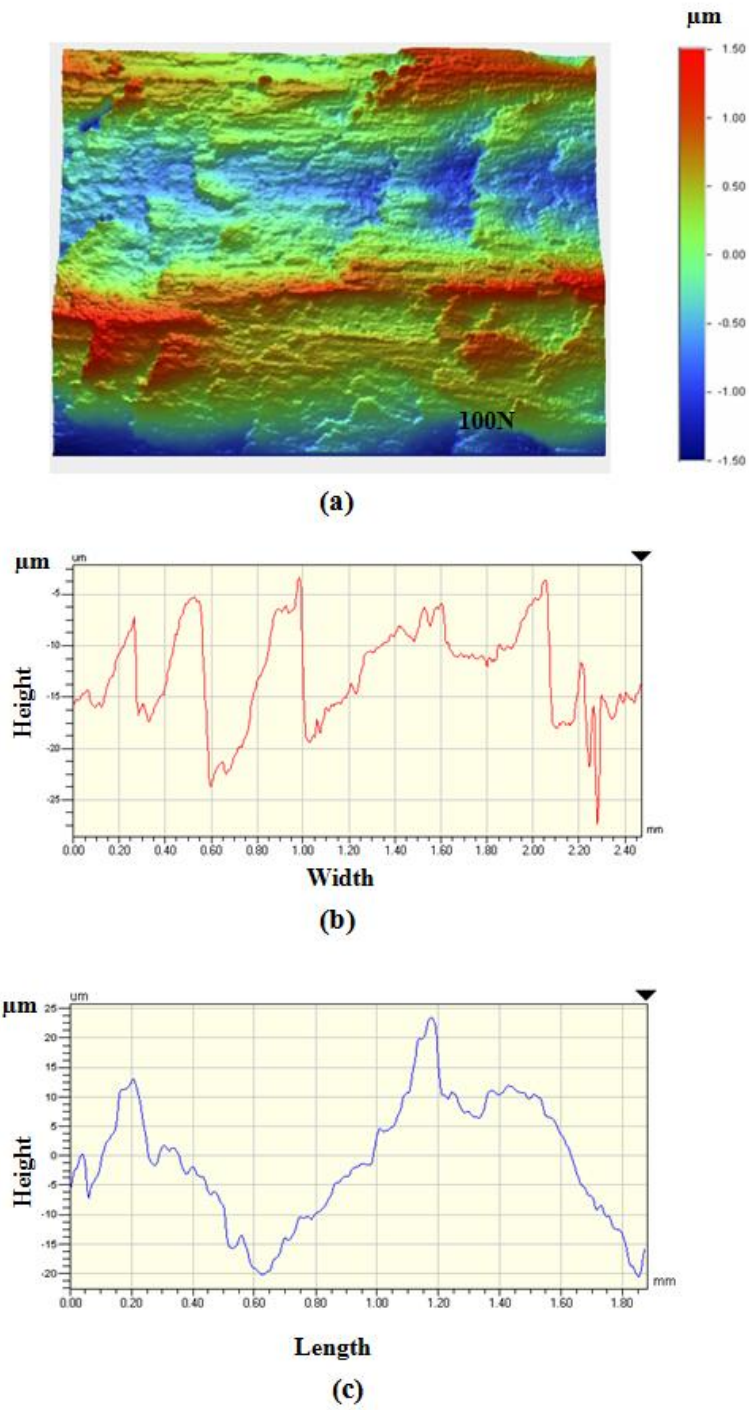


**Fig.5.31.** Pseudo-3D images (a) , X (b) and Y profile (c) of the middle worm surface at the load 100N in argon.

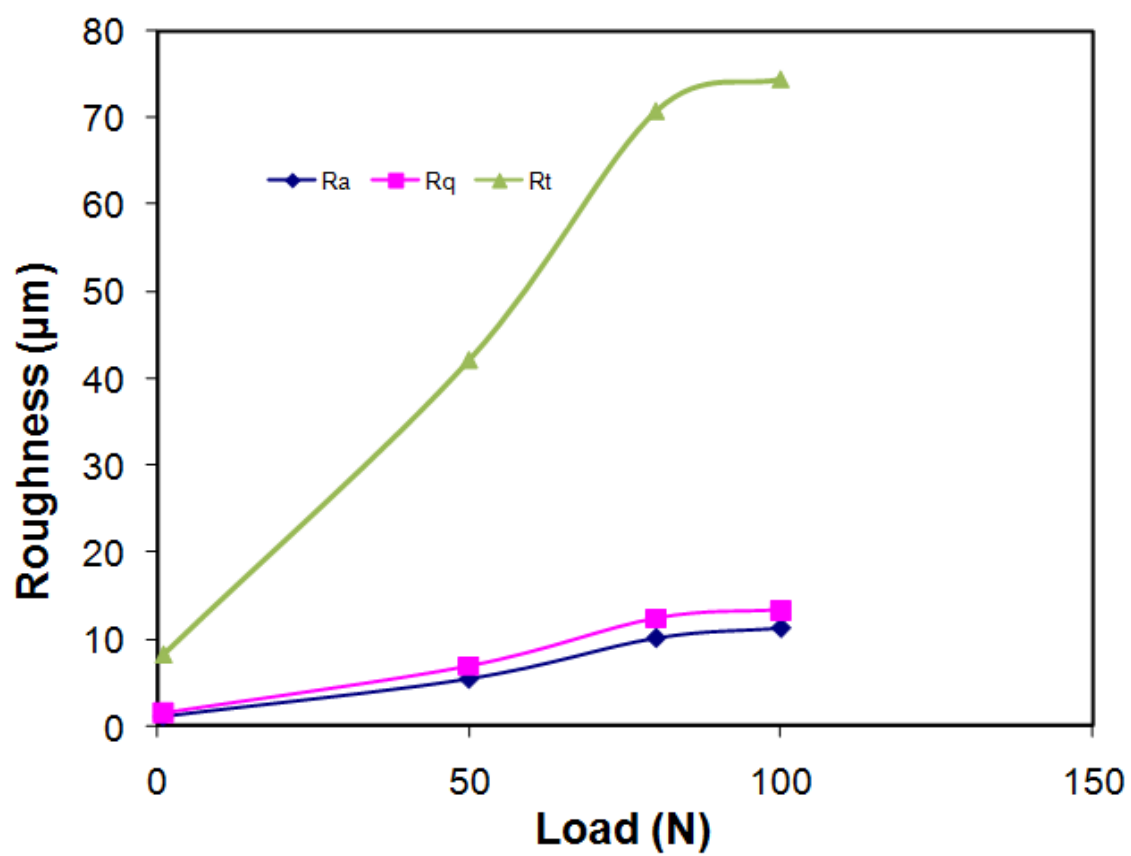


**Fig.5.32.** Variation of worn surface roughness parameters with load in argon.

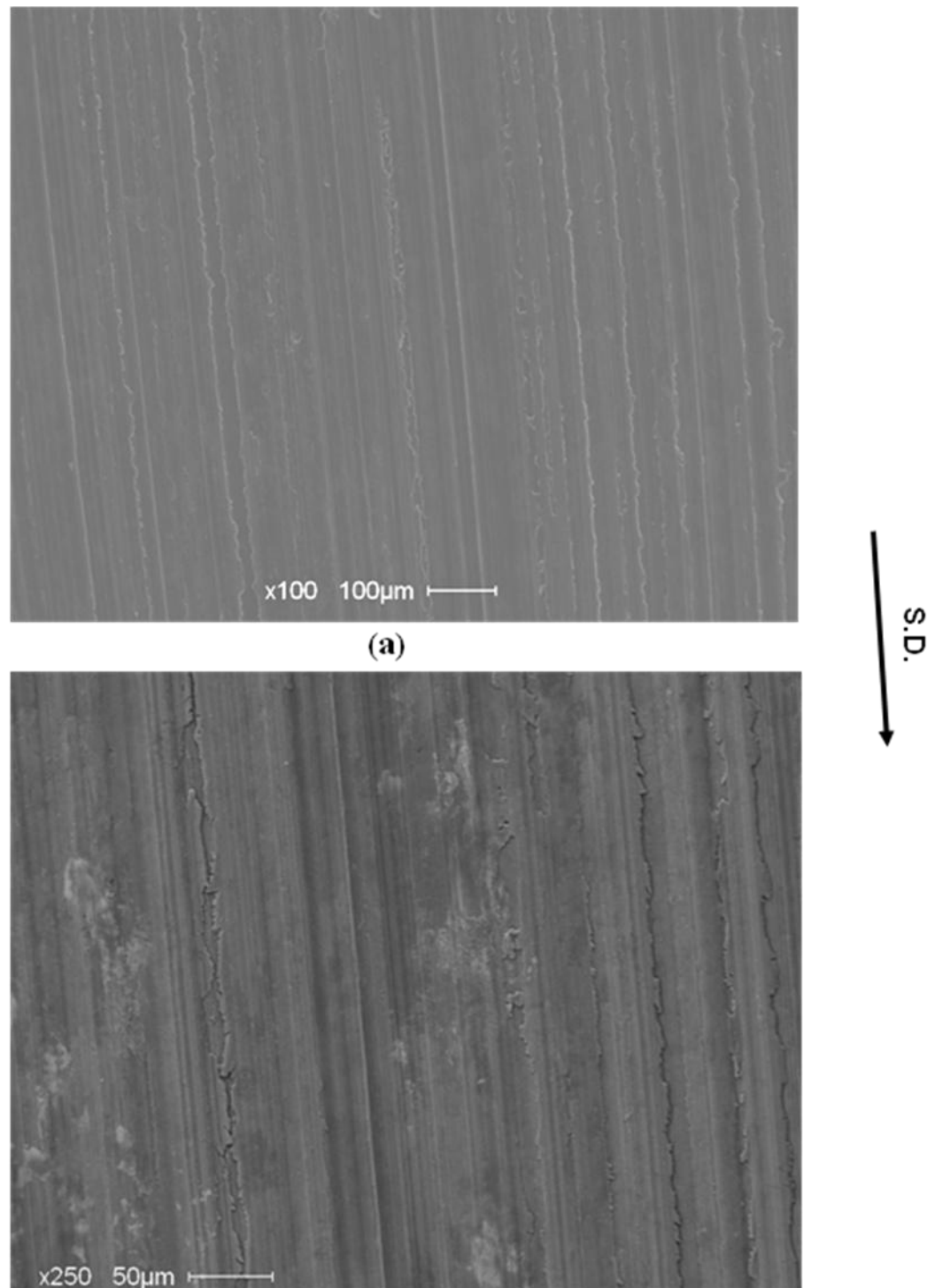


**Fig.5.33** SEM micrographs of the worn surface of Al-11% Si alloy sample tested at 1N in argon atmosphere: (a) secondary SEM, (b) back scattered SEM.



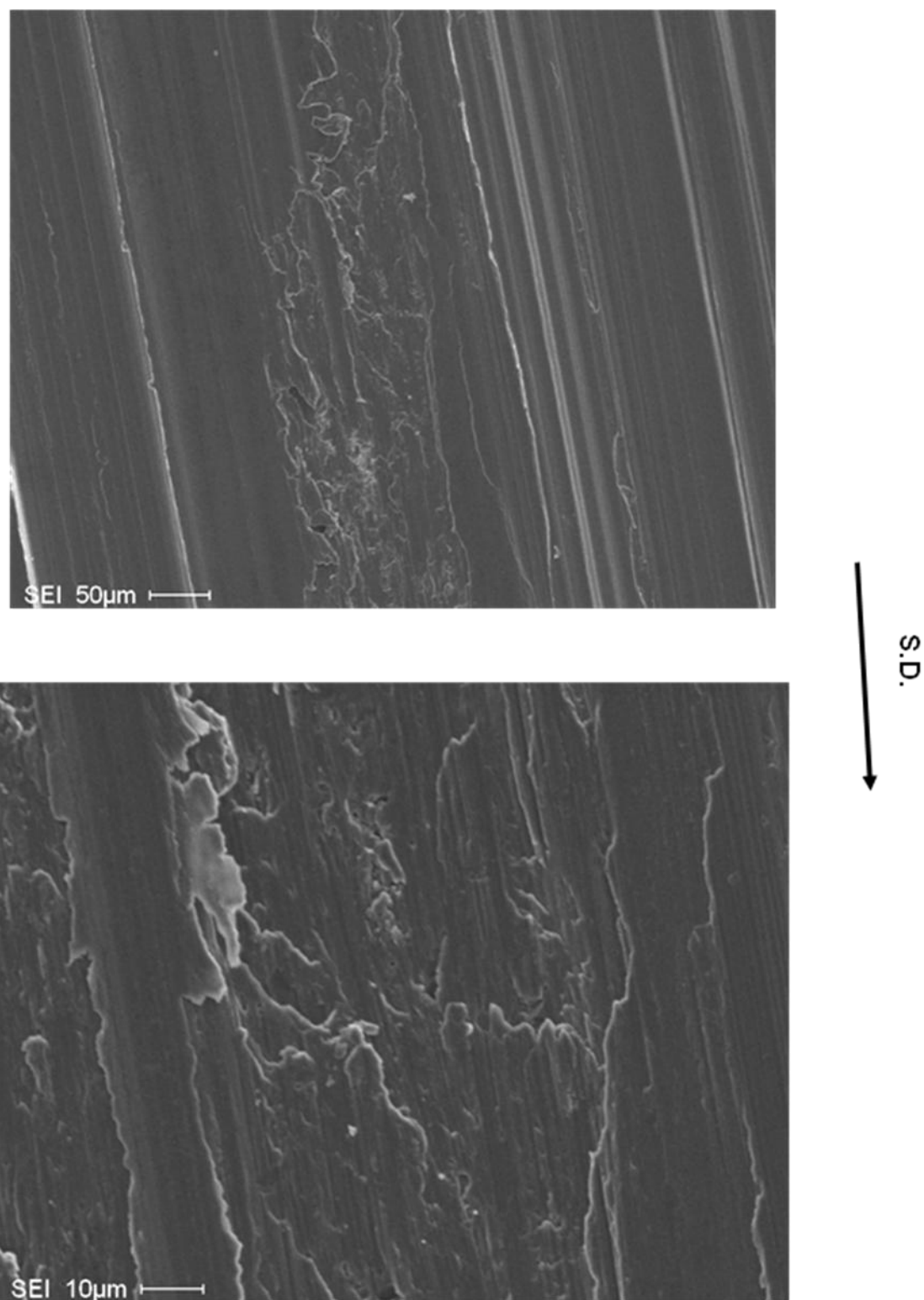
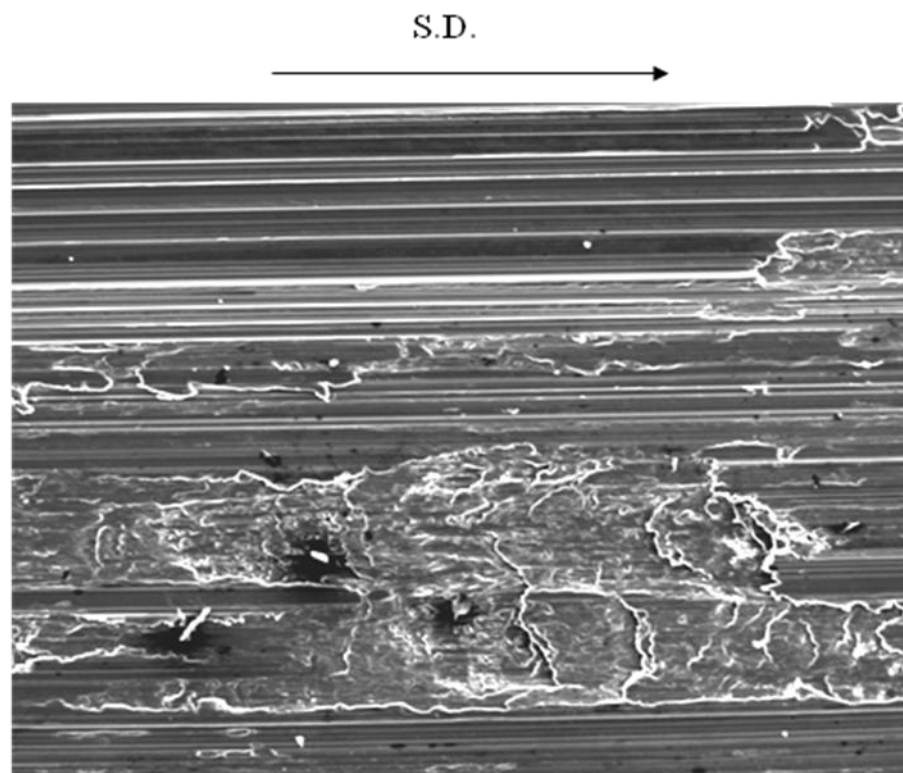
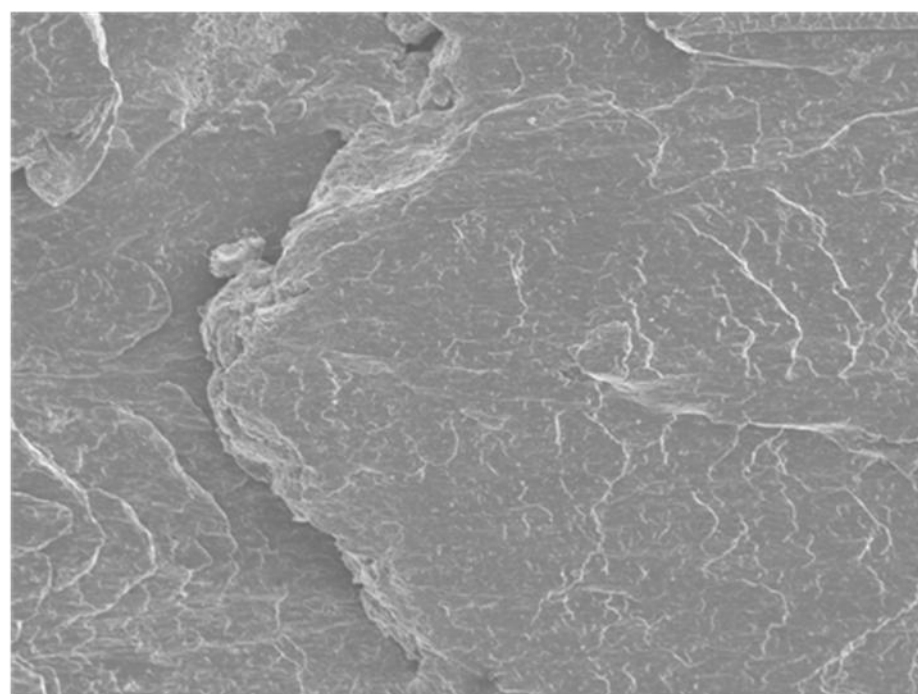


**Fig.5.34** SEM micrographs of the worn surface of Al-11% Ai alloy sample tested at 50N in argon atmosphere with two magnifications.

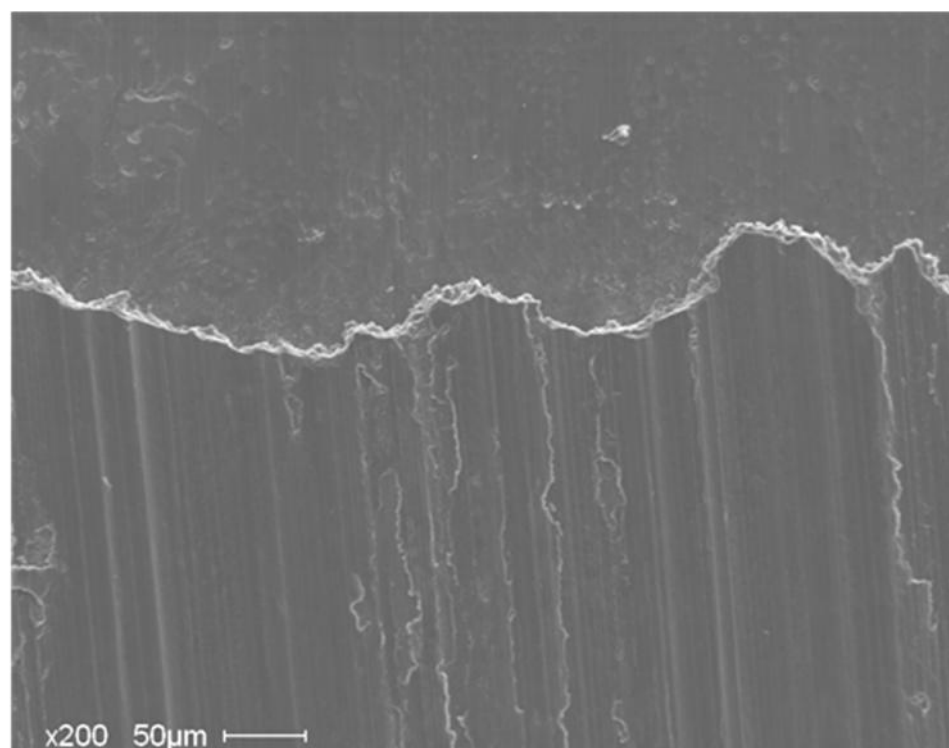


(a)



(b)

**Fig.5.35** SEM micrographs of the worn surface of Al-11% Si alloy sample tested at 80N (a) and 100N(b) in argon atmosphere.



S.D

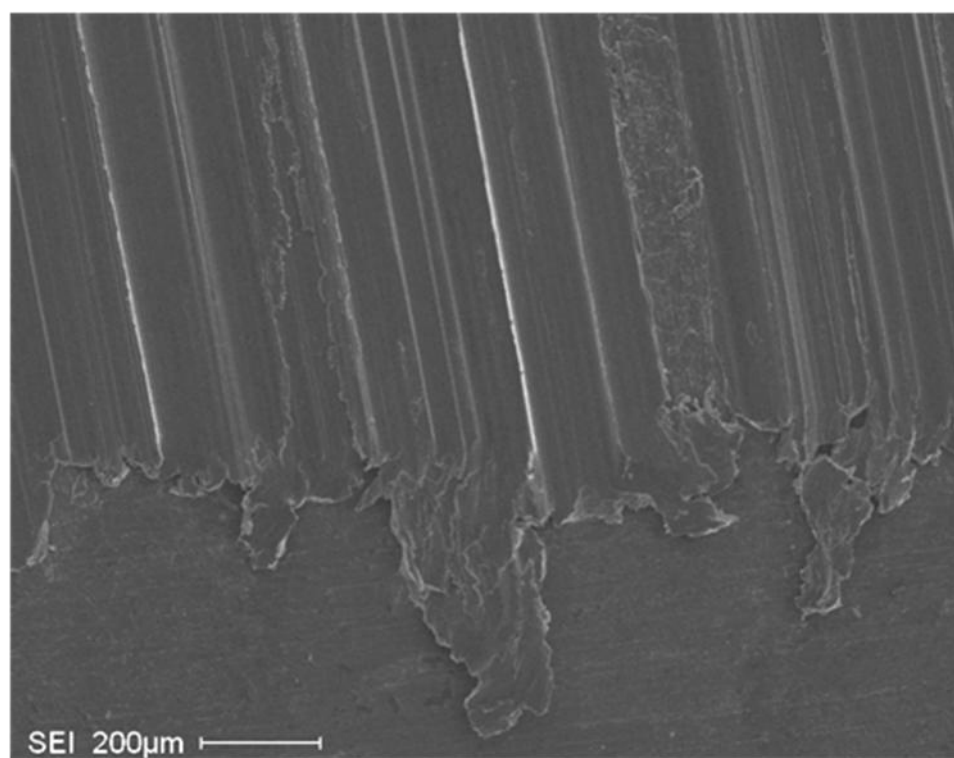
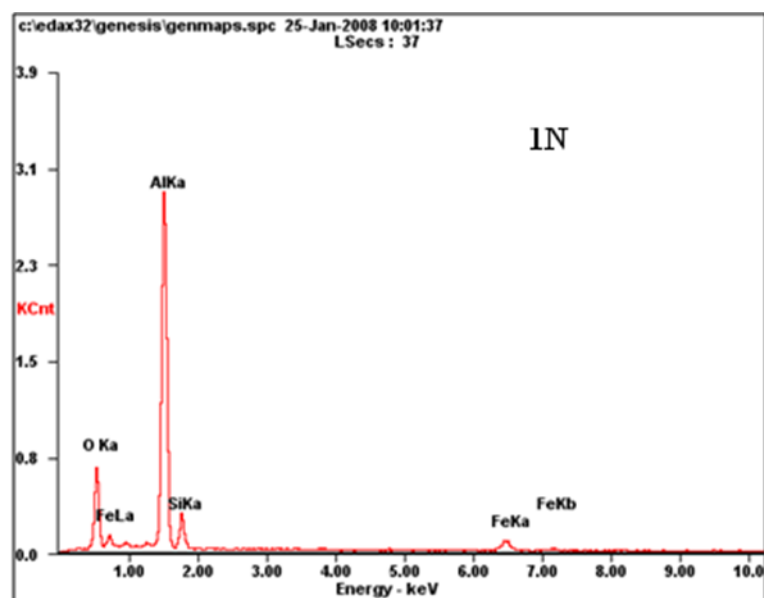
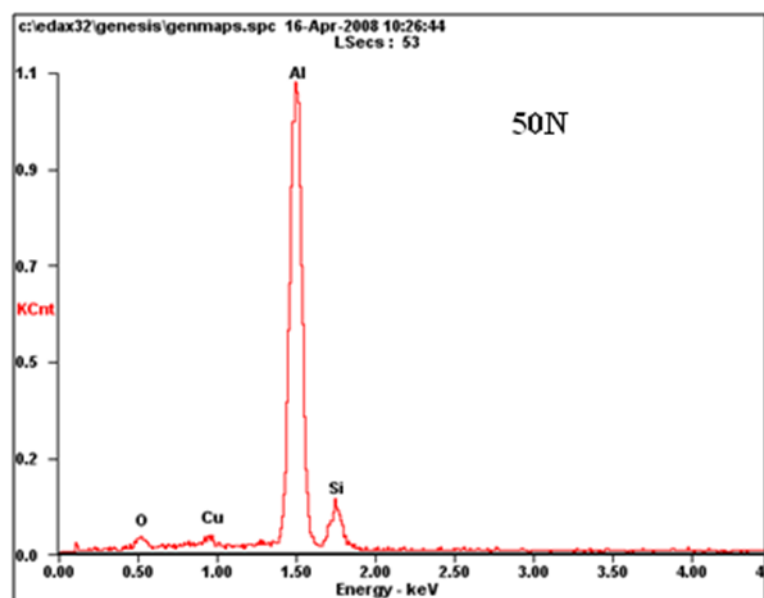


**Fig.5.36** SEM micrographs of the edge of wear track at 1N (a) and 50N (b) in argon. At 50N, layers in the form of flake were observed.

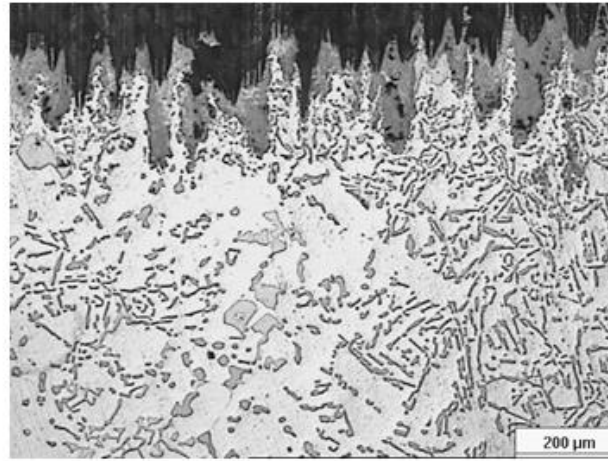


(a)

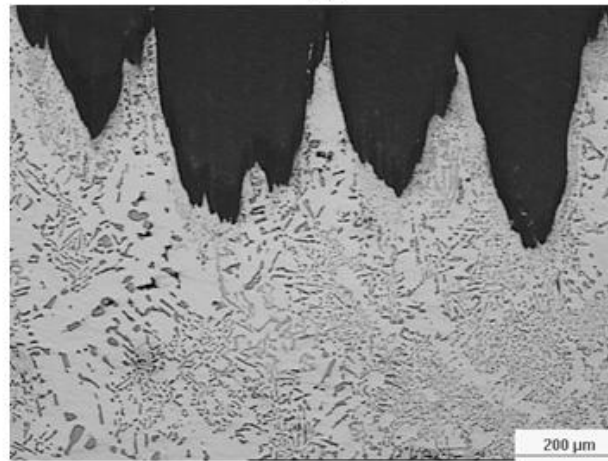


(b)

**Fig.5.37** EDS spectra of the worn surfaces at 1N and 50N after a sliding distance of 4000m tested in argon atmosphere.



(a)



(b)



**Fig. 5.38** Subsurface optical micrographs of Al-11% Si alloy taken from the tapered sections cut at angle of  $5.7^\circ$  to the contact surfaces at loads of (a) 10 N, (b) 50 N and (c) in argon (5% RH).

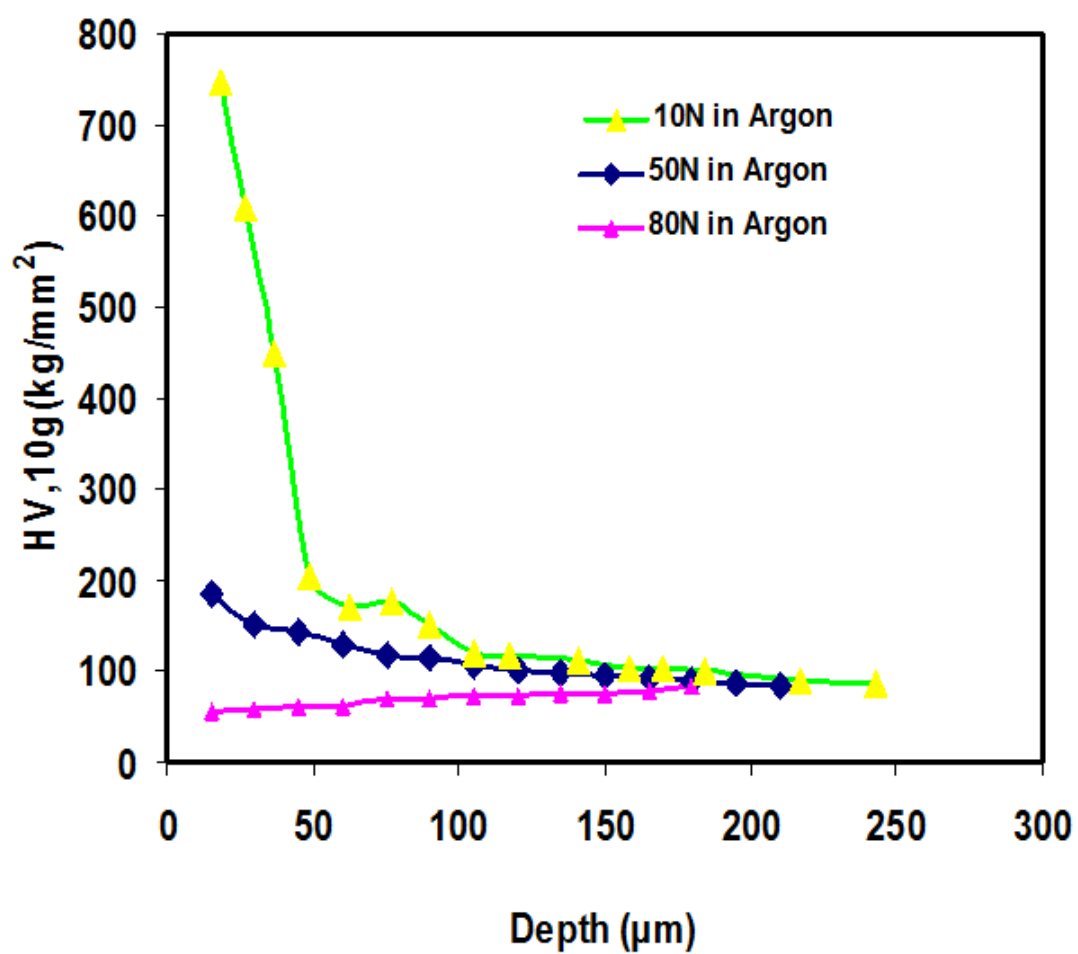
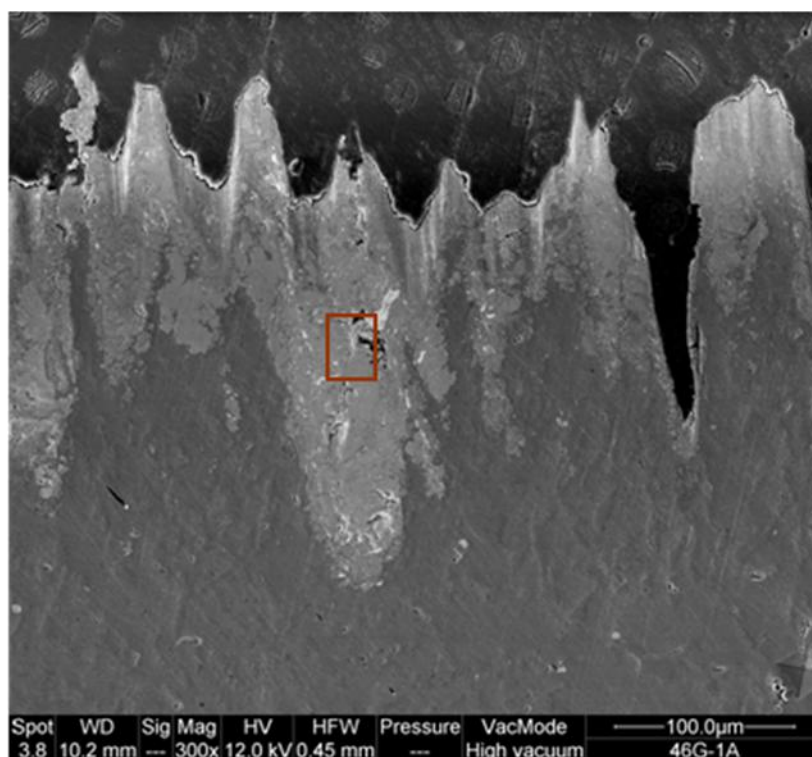
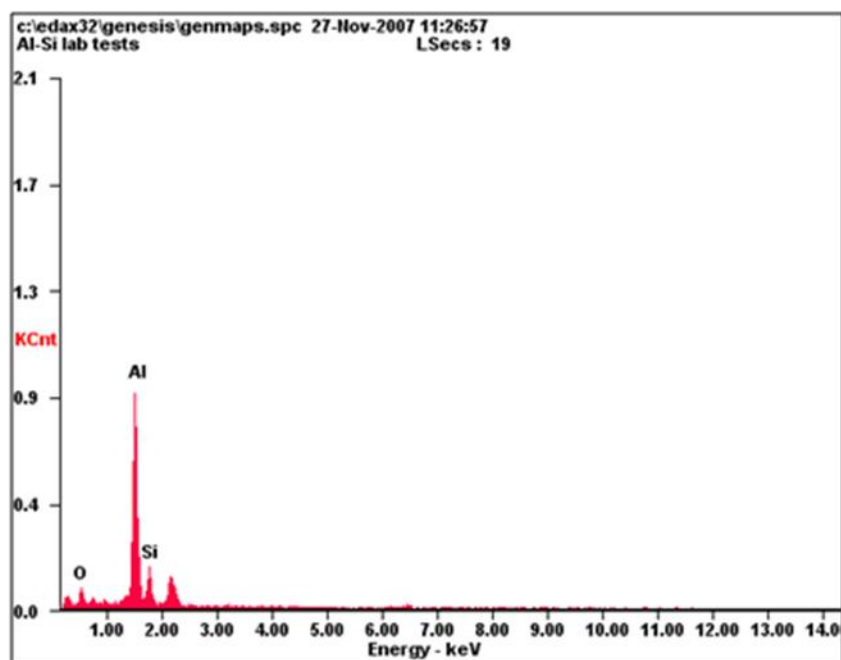


**Fig.5.39** Subsurface microhardness (HV, 10g) profile at load of 10N, 50N and 80N in argon after a sliding distance of 4000m. Microhardness measurements were performed on transverse tapered sections (cut at an angle of  $5.7^\circ$  to worn surface)



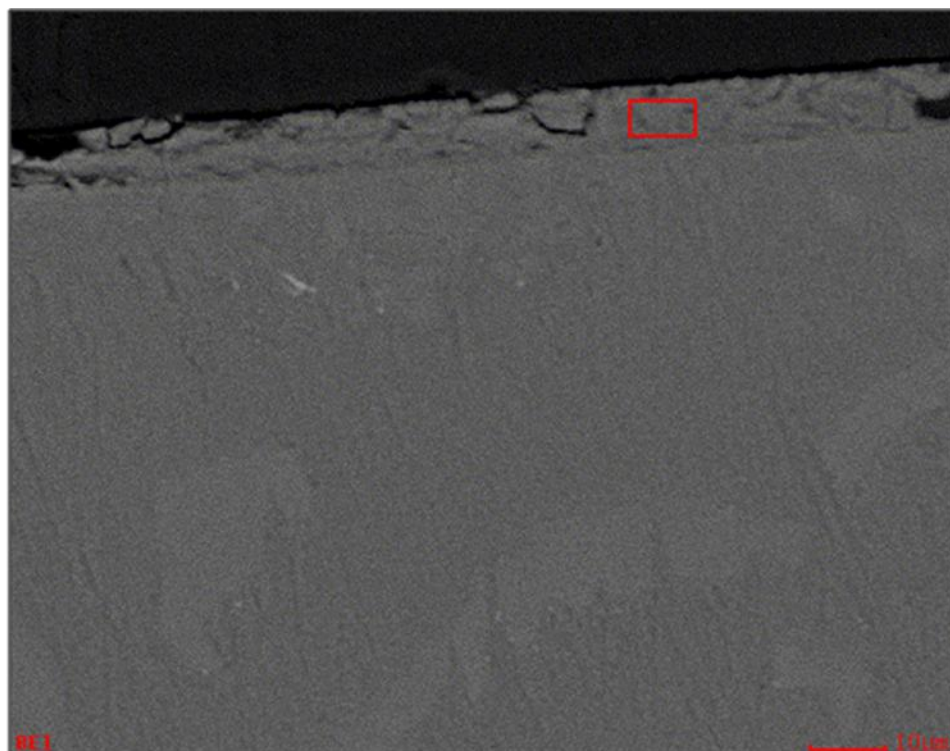
(a)



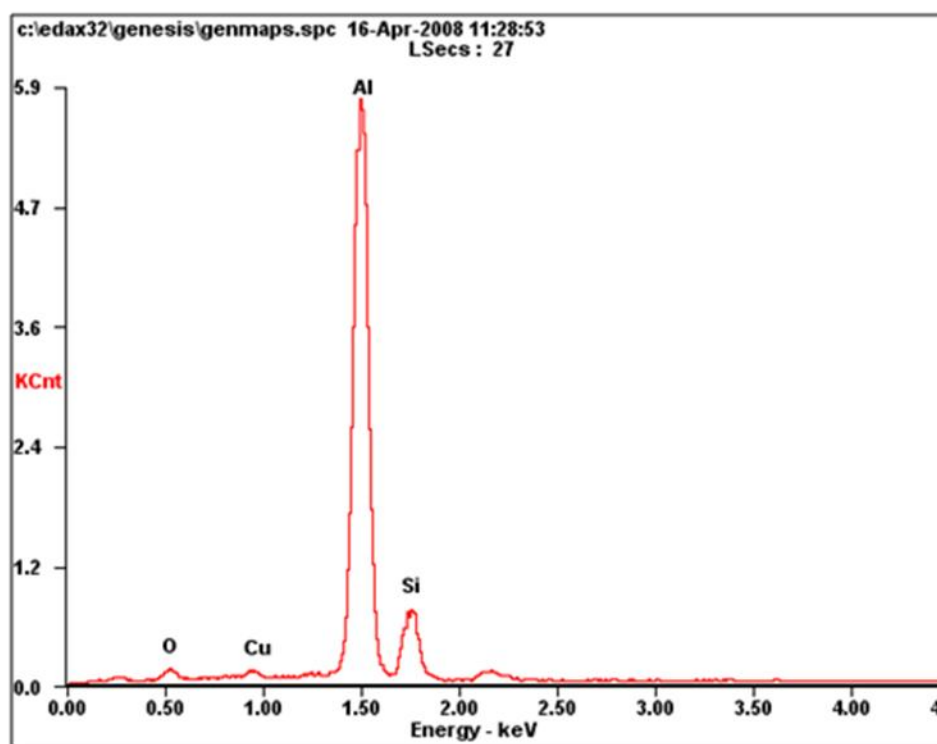
(b)

**Fig.5.40** Back scattered SEM (a) and EDS (b) spectra of the worn subsurface at 10N after a sliding distance of 4000m tested in argon atmosphere.





(a)



(b)

**Fig.5.41** Back scattered SEM (a) and EDS (b) spectra of the worn subsurface at 50N and 50N after a sliding distance of 4000m tested in argon atmosphere.



## **CHAPTER 6**

### **SUMMARY AND CONCLUSIONS**

The purpose of this research was to study the tribological performance of the eutectic Al-Si alloys with the potential for use in the manufacturing of linerless automotive engine blocks. The microstructures and wear performances of engine blocks made of two eutectic Al-Si alloys with different Si morphologies and dendrite arm spacing were characterized after engine tests. In addition, dry sliding wear tests on a selected eutectic Al-11% Si alloy were conducted using a block-on-ring (SAE 52100 type steel) configuration under controlled air and argon atmospheres to gain a deeper understanding of the wear behaviour of near eutectic alloys.

#### **6.1 Microstructures and Wear Performances**

- 1) The brass-chilled Al-Si alloy had a finer microstructure with more spheroidized Si particles at a lower aspect ratio than the sand-cast Al-Si alloy. The brass-chilled Al-Si alloy also had shorter dendrite arm spacing.
- 2) Overall, both Al-Si alloys provided similar wear performance, as determined by metallographic examinations of the samples after they had been subjected to engine tests.

#### **6.2 Dry Sliding Wear Behaviour of Al-11% Si Alloy under Dry Air and Argon Atmospheres and Their Wear Mechanisms**

- 1) Two different wear regimes were identified in the load range between 0.2 N and 180 N in an air atmosphere: mild wear (MW) and severe wear (SW). The mild

wear regime consisted of two sub-regimes: MW-1 and MW-2. The transition from MW to SW occurred at a load of 160 N.

- 2) The wear process under dry air in the mild wear regime was controlled by the formation and destruction of tribolayers composed of Fe, Al, Si, and O on the worn surfaces. When the load increased, the tribolayers changed from Fe-riched to Al-riched oxidized tribolayers, and the debris shape changed from powder to plate-like particles with an increase in size that corresponded to the transition from MW-1 to MW-2.
- 3) The tests performed in an argon atmosphere resulted in the attainment of low mild wear (LMW) rates, which were approximately an order of magnitude lower than those observed in dry air (5% RH) at loads below 10 N. LMW in argon was found to be a result of deformed, smooth, and continuous Al-(Si) tribolayers.
- 4) The MW observed in a dry air atmosphere produced lower wear rates for the Al-11% Si compared to those of the Al-18.5% Si alloy [16]. The load at which the transition from MW-1 to MW-2 occurred was however lower than for the A390, and the transition loads to the severe regime in A390 was 150N lower than that in the Al-11% Si alloy. Under the argon atmosphere, there was little difference between these two alloys.
- 5) At a low load (in MW-1) in an air atmosphere, the wear mechanism is oxidative. In MW-2, the wear mechanisms included delamination and Al transfer. Compared to the air atmosphere, the tribolayers were uniform and stable in the argon atmosphere, resulting in low wear rates. The mechanism of material removal under the argon atmosphere was delamination. Wear was also more

sensitive to applied load in the argon atmosphere because the thermal softening dominates the wear process in the competition between strain hardening and thermal softening that occurs at the contact surface.

### **6.3 Suggestions for Future Work**

Lubricated sliding wear tests on eutectic Al-Si alloys are necessarily conducted using a block-on-ring configuration to obtain a deeper understanding of the wear behaviour in real-engine work condition. Using the sample with curvature can be well simulating real-engine work condition in lab (already had some progress during my research). It is economical and practical for providing valuable information to develop automotive engine alloys.

## Appendix

### Wear test results in air and in argon

Load(N)	11%Si wear rate in air (mm <sup>3</sup> /m)	11% Si wear rate in argon (mm <sup>3</sup> /m)
0.2	1.84E-05	
0.5	6.43E-05	
1	1.26E-04	1.84E-05
2	1.38E-04	
3	1.84E-04	
4	2.51E-04	
5	2.88E-04	2.76E-05
6	3.03E-04	
7	3.12E-04	
8	3.37E-04	
9	3.52E-04	
10	3.77E-04	3.06E-05
20	9.28E-04	1.41E-04
30	1.61E-03	1.84E-04
40	2.17E-03	
50	2.17E-03	1.59E-03
60	2.43E-03	4.01E-03
70	2.66E-03	
80	2.75E-03	2.80E-03
90	4.00E-03	
100	4.66E-03	7.39E-02
110	5.05E-03	8.20E-02
120	5.39E-03	
130	6.38E-03	
140	6.72E-03	
150	6.76E-03	
160	6.81E-03	
170	9.45E-01	
180	9.40E-01	

## REFERENCES

1. J. L. Murray and A.J. McAllister, Bulletin of Alloy Phase Diagrams, 5(1984) 74-84.
2. Yamagata, The Science and Technology of Materials in Automotive Engines, Woodhead Publishing limited, Cambridge, (2005) 10-39.
3. W. S. Miller, L. Zhuang, J. Bottema, A. J. Wittebrood, P. De Smet, A. Haszler, and A. Vieregge, Materials Science and Engineering. A280 (2000), 37-49.
4. A. T. Alpas, and J. Zhang, Metallurgical and Materials Transactions 25A, 1994, 969- 983.
5. A. Edrissy, T. Perry, Y. T. and, A. T. Alpas, Wear, 251(2001) 1023-1033.
6. X. Nie, L. Wang, E. Konca and, A. T. Alpas, Surface and Coatings Technology, 188-189( 2004)207-213.
7. Edward P. Becker, Tribology International 37 (2004) 569–575.
8. R.E.Green, Die Cast Engineer, 14, 5,(1970)12-26.
9. C. M. Taylor, Engine Tribology, Elsevier, New York, 1993, 104-216. ( Chapter2)
10. Richard Stone, Introduction to Internal Combustion Engines (3rd Edition), SAE, 1999, 1-21.
11. D. Assanis, C. Borgnakke, D. E. Cole, D. J. Patterson, Internal Combustion Engines, Analysis of Engine Process, U. S. Automobile Engines, 1993, 620-641.
12. L.L. Ting, Wear Control Handbook, Peterson, M. B. and Winer, W. O., Eds., ASME, New York, 1980, 609-665.
13. J. B. Heywood, Internal Combustion Engine Fundamentals, McGraw-Hill Series in Mechanical Engineering, 1989, 341-357.
14. C. S. Tung, M. L. Mcmillan, Tribology International, 37(2004)517-536.
15. C. M. Taylor, Engine Tribology, Elsevier, New York, 1993, 75-89.
16. M. Elmadagli, “Microstructural Studies of Wear Mechanisms in Cast Aluminum Alloys”, Ph.D., Dissertation, University of Windsor, Windsor Ontario, Canada,2005.
17. Z. Ye, C. Zhang, Y. Wang, H. S. Cheng, S. Tung, Wear, 257(2004) 8-31.
18. S. D. Henry, “Friction, Lubrication and Wear Technology”, ASM Handbook, the Materials Information Society, 18 (1992) 162-171.
19. W. R. Smith and R. Knight, JOM, August 1995, 32-39.

20. Standard Terminology Relating to Erosion and Wear, G40. Annual Book of ASTM Standards, ASTM, 1995, 30-50.
21. J. Zhang and A.T. Alpas, *Acta Mater.* 45(1997) 513-528.
22. A. Dyson, *Journal of Tribology International*, 8 (1975) 77-87.
23. A. R. Riahi, A. T. Alpas, *Wear*, 251(2001) 1369-1407.
24. P. K. Rohatgi, B. C. Pai, *Wear*, 28, (1974) 353-367.
25. S. C. Lee, H. S. Cheng, *J. Tribol.*, 113(1991) 327-334.
26. P. C. Nautiyal, J. A. Schey, *Trbol.* 112, 282-287.
27. A. S. Reddy, B. N. P. Bai, K. S. S. Murthy, S. K. Biswas, *Wear*, 171(1994) 115-127.
28. Haizhi Ye, *Journal of Materials Engineering and Performance*, 12(3) (2003) 288-297.
29. E. L. Roy, *ASM Handbook*, v 15, "Castings" 9th ed., ASM International, Materials Park, OH, 1992, p. 743-769.
30. R. E. Green, *Die Cast Engineer*, 14, 5(1970) 12-26
31. J. Clarke, A. D. Sarkar, *Wear*, 54(1979) 7-16.
32. Doty, Herbert William, <http://www.freepatentsonline.com/6921512.html>, 2005.
33. Hiroshi Yamagata, *The Science and Technology of Materials in Automotive Engines*, Woodhead Publishing limited, 40-46.
34. H.M. Skelly and C.F. Dixon; 'Hypereutectic Aluminum-Silicon Alloys Produced by Hot Compaction of Atomized Powder' Canada Dept. of Mines and Technical Surveys, Mines Branch Research Report, R184, May 1966.
35. Y. Huang, X. Jiang, S. Li, *Bull, Mater. Sci.*, Indian Academy of Science, 23(2000)539-542.
36. C. S. Tung, M. L. Mcmillan, *Tribology International*, 37(2004) 517-536.
37. S. Sailer, *Wear Control Handbook*, Peterson, M. B. and Winer, W. O., Eds., ASME, New York, 1980, 1305-1308.
38. R. Shivanath, P.K. Sengupta, T.S. Eyre, *British Foundrymen*, 79(1977)349-56.
39. T.S. Eyre; "Wear of Aluminum Alloys", *Microstructural Science*, Stevens, Vander Voort, McCall, eds., Elsevier North Holland, Inc., 1980, New York, NY and Amsterdam, 8 (1980) 141-151.
40. M. Elmadagli, T. Perry, A.T. Alpas, *Wear*, 262(2007), 79-92.

41. I.M. Hutchings, Sliding wear, in *Friction and Wear of Engineering Materials*, 1992, 82-92.
42. W. Hirst and J.K. Lancaster, *The Influence of Speed on Metallic Wear* 229-241.
43. A. Dyson, *Journal of Tribology International*, 8(1975)77-87.
44. G.Dietter, *Mechanical Metallurgy*, Third edition, 1998, 301-304.
45. M. F. Ashby, J. Abulawi, and H. S. Kong, *Tribology Transactions*, 34(1991) 577-587.
46. M. Elmadagli, A.T. Alpas *Wear* 261 (2006) 823–834.
47. R.A. Saravanan, J.-M. Lee, S.-B. Kang, *Metall. Mater. Trans. A* 30 (1999) 2523–2538.
48. H. Goto, M. Ashida, K. Eno, *Wear* 116 (1987) 141–155.
49. B. K. Yen, and T. Ishihara, *Wear*, 198 (1996) 169-175.
50. W.A. Brainard, D.H. Buckley, *Dynamic-scanning-electron-microscopy study of friction and wear*, NASA Technical Note TN D-7700, 1974 (National Aeronautics and Space Administration).
51. A. Glaser, *Wear* 73 (1981) 373–386.
52. N. Gravier, E.C. Cutiongo, Y.P. Chung, *Tribol. Trans.* 38 (1995) 168–172.
53. B.K. Yen, *J. Mater. Sci.* 32 (1997) 821–828.
54. B.K. Yen, T. Ishihara, *Wear* 198 (1996) 169–175.
55. H. Goto, K. Uchijo, *Wear* 259 (2005) 613–619.
56. K.C. Ludema, in *ASM Handbook*, vol. 18, *Friction and Wear Applications*, ASM (1992) 257-271.
57. A.R. Riahi, A.T. Alpas, *Wear* 251 (2001) 1396-1407.
58. P. Heilmana, W. A. T. Clark, D. A. Rigney, *Acta metal.* 33(1983) 1293-1305.
59. K. Razavizadeh and T. S. Eyre, *Wear*, 79 (1982) 325-333.
60. R.Antoniou and D. W. Borland, *Materials Science and Engineering*, 93 (1987) 57-72.
61. J. Clarke, and A. D. Sarkar, *Wear*, 69 (1981) 1-23.
62. K.M. Jasim, E.S. Dwarakadasa, *Wear*, 119(1987) 119-130.
63. K. Mohammed Jasim, and E. S. Dwaradasa, *Wear*, 119 (1987) 119-130.

64. A. S. Reddy, B. N. Pramila Bai, K. S. S. Murthy and S. K. Biswas, *Wear*, 171 (1994) 115-127.
65. Cleg A. J., Das A. A., *Wear*, 43, 3(1977)367-373.
66. G. C. Barber, S. Jafry, *Lubrication Engineering*, 47, 5(1991) 423-430.
67. V.C. Srivastava, R.K. Mandal, B. Chatterjee, S.N. Ojha, *Trans. Indian Inst. Met.*, 52, 1, Feb 1999, 29-40.
68. J. Zhang and A.T. Alpas, *Wear*, 155(1992) 83-104.
69. A. R. Riahi, T. Perry, A. T, Alpas, *Materials Science and Engineering A343* (2003) 76-81.
70. S. Wilson, A.T. Alpas, *Wear*, 212(1997) 41-49.
71. M. Chen and A.T. Alpas, Proceedings of STLE/ASME International Joint Tribology Conference, IJTC 2006, 2.
72. S. Sailer, *Wear Control Handbook*, Peterson, M. B. and Winer, W. O., Eds., ASME, New York, 1980, 1305-1308.
73. Aluminum Alloys, *ASM Handbook, Metallograph and Microstructures*, ASM International, Materials Park, 9(1985) 351-388.



## **VITA AUCTORIS**

The author obtained his Bachelor of Science in Materials Science from Lanzhou University in 1992. After that he was accepted as a Metallurgical & Materials Engineer in Technology Centre, Anshan Iron & Steel Group, China. From 2005, he worked at R&D of Stelco Steel Company, Hamilton, Canada as a Metallurgical Engineer. He joined the Materials Engineering Program at the University of Windsor in September, 2006 as a Researcher and got his master degree in 2009.